Characterizing Infrared Molecular Radiation in a Flat-Flame Burner and an Optical Spark-Ignition Engine

by

Lucca Henrion

A dissertation submitted in partial fulfillment
of the requirements for the degree of
Doctor of Philosophy
(Mechanical Engineering)
in the University of Michigan
2020

Doctoral Committee:

Professor Volker Sick, Chair
Michael Gross, Southwest Research Institute
Professor Eric Johnsen
Professor Annalisa Manera

Lucca Henrion

lhenrion@umich.edu

ORCID iD: 0000-0002-6116-6771

Dedication

To my mother and father, Alexa and Blaise

and my sister and her children, Alba, Annabelle, Amelia, and Autumn

and my many wonderful friends

and most of all my dearest partner, Alyssa

Without all of you, this work would not have been possible.

Acknowledgments

I would like to thank my advisor Professor Volker Sick and committee member Dr. Michael Gross for their guidance and support through the development of this work. I would like to extend my many thanks to my committee members Professor Eric Johnsen and Professor Annalisa Manera, for their participation in my doctoral work. Thanks to my committee, I have developed a deep understanding of radiative phenomena in combustion systems.

This project has allowed collaboration with Professor Daniel Haworth and his research group at Pennsylvania State University. I would like to acknowledge the collaborative research we have done with Professor Haworth as his expertise and simulations have been invaluable to the development, execution, and success of these experiments.

Finally, I want to thank all the members of the Quantitative Laser Diagnostics Laboratory for providing an excellent, enriching, and global work environment. Dr. Mohammed Alzuabi for his patience and collaboration in operating the engine during experiments, Dr. Ahmet Mazacioglu for cooperation and advice in infrared work, Dr. Ivan Tibavinsky for ongoing research discussions and support, Angela Wu for her collaboration and words of encouragement, Allison Gibson for providing an outstanding sounding board for ideas, Owen Sayer for his help in collecting data, and James Elkins for his friendly technical support. Additionally, I would like to thank Dr. David Reuss and Dr. Hao Chen for helping situate me in the broad research domain of internal combustion engines.

The information, data, or work presented herein was funded in part by the Office of Energy Efficiency and Renewable Energy, U.S. Department of Energy, and the Department of Defense, Tank and Automotive Research, Development and Engineering Center (TARDEC) under Award Number DE-EE0007307.

The Rackham Graduate School of the University of Michigan has supported me through the Rackham Merit Fellowship and conference travel.

Table of Contents

List of Tables

List of Figures

Abstract

There is a common assumption that radiative heat loss is negligible in spark-ignition (SI) engines. Total radiation consists of soot particle and molecular gas radiation. Soot radiation is often seen in rich flames, where small clumps of carbon particles emit in a broadband fashion primarily in visible wavelengths. Molecular radiation, consisting in large part of H_2O and CO_2, occurs due to reactant and product gases of combustion at high temperatures, and these molecules radiate in specific infrared wavelength bands corresponding to discrete energy levels. Recent interest has led researchers to re-evaluate the influence of molecular radiation as a source of engine heat loss. Researchers created a simulation technique that demonstrated the relative importance of molecular radiation as an emitter of energy, but also molecular influence in absorbing energy throughout the engine cylinder. However, these simulations lacked experimental measurements for validation.

To address the lack of experimental data, a methodology was developed to measure the wall reaching radiation in a spectrally and temporally resolved way. This work demonstrates broadband emission spectroscopy in an atmospheric flat-flame burner and the first crank-angle-resolved broadband emission spectroscopy performed in the near- and mid-wavelength infrared (IR) in a well-characterized, spark-ignited, optical, research engine. Flat-flame measurements were performed at a variety of equivalence ratios and nitrogen dilutions. Engine measurements were made at twelve conditions to characterize the impacts of equivalence ratio, nitrogen dilution, and carbon dioxide dilution on radiative heat transfer. The presented studies provide information to

understand the magnitude, lifetime, and variation of molecular radiation at a series of combustion conditions at atmospheric and engine-relevant pressures and temperatures.

These experimental measurements were used to validate and improve predictive models of intra- and trans-cylinder radiation in combustion systems. Strong agreement between the measured and simulated spectra exists for the atmospheric-pressure flat-flame burner, and strong agreement from 2.4-3.5 μm was seen for stoichiometric engine combustion at 1300 rev/min. Cycle-to-cycle variability of radiation in the measurements is evaluated as it corresponds to the measured pressure and combustion landmarks. Engine measurements showed that CO_2 is strongly self-absorbed, and the impacts of radiative absorption on local condition changes are discussed. The experimental trends are evaluated and discussed in the context of their implications on engine behavior. Finally, these results show the potential for the development of a diagnostic through experimental measurements.

Chapter 1 Introduction

1.1 Background

1.1.1 Global context of advanced engine research

Climate change due to human-made greenhouse gas (GHG) emissions has drawn worldwide attention as the defining issue of the century. Projections by the Intergovernmental Panel on Climate Change (IPCC) suggest that catastrophic impacts will take place if global warming exceeds 1.5 °C above the pre-industrial average temperature [1]. The emission gap is a useful tool to understand the scale of reduction needed, it quantifies the difference between World projected GHG emissions in the year 2030, and the IPCC recommended World GHG emissions to stay below a 1.5 °C of warming [2]. The 2019 emission gap report reported a 32 $GtCO_2e$ gap between the emission projected with current policy and technology and the recommended 1.5 °C range [2]. In 2018, the transportation sector made up ~28% of primary energy usage in the United States and accounted for ~36% of the total CO_2 emissions [3]. A strong focus must remain on improving the efficiency of the transportation sector to reduce overall GHG emissions.

Efficiency improvements to the transportation sector are a promising avenue for GHG reduction, but this sector is facing challenges due to its current distributed form. In 2018, there were ~270 million registered vehicles on the road in the United States and 92% of transportation energy was provided by petroleum in 2018 [4]. Despite the recent increases in electric vehicles (EV), most vehicles still emit GHG and pollutants directly out of their tailpipe. Solutions to

capture, store, or use GHGs are not currently feasible at vehicle scales [5]. Therefore, the most direct way to transportation emissions is to improve fuel efficiency while maintaining or reducing other pollutant emissions.

Federal policy has been effectively leveraged to reduce the GHG-intensity of the transportation sector. The Corporate Average Fuel Economy (CAFE) standards enacted in 1975 set moving standards that increased efficiency and reduced pollutant emissions in the next generations of vehicles. From 1975 to 2017, the fuel economy of US vehicles increased from 13 to 24.8 miles per US gallon, and the average vehicle emits 357 grams of CO_2 per mile – a 48% reduction in CO_2 emission [6]. These regulations have been invaluable in motivating research and the development of more energy-efficient vehicles.

Advanced engine research has been a valuable tool to investigate solutions demanded by Federal and State regulations. Regulations change over time, and researchers continue to identify ways of reducing engine losses and improving fuel efficiency. Engines are imperfect and inefficient sources of work that often have thermal efficiencies (TE) in the 20-30% range [7]. However, researchers have created solutions that continue to improve the efficiency of vehicles. Figure 1-0-1 demonstrates the typical energy split of a spark-ignited internal combustion engine. From the figure, it is clear that heat loss to coolant and exhaust gas enthalpy losses are the largest sources of efficiency penalties. Small reductions to these losses could result in a ~1-4% increase in TE, and efficiency improvements can result in massive fuel savings over the lifetime of a vehicle fleet [8].

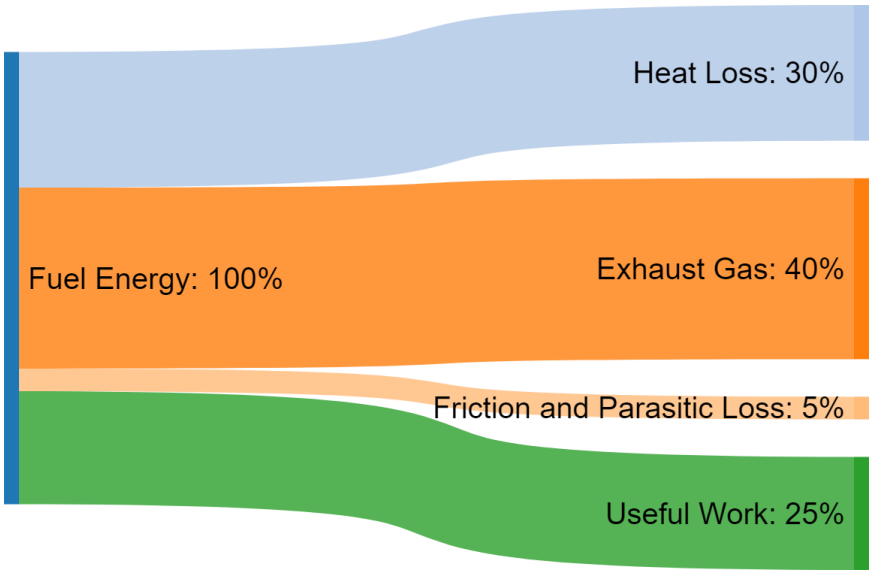

Figure 1-0-1: Diagram of typical energy split in spark-ignited internal combustion engine [7]

One pathway to improve gasoline-fueled engine efficiency is to operate at higher pressures. An example of this is the gasoline compression-ignition (GCI) engine, which operates at a higher compression ratio (CR) than a traditional SI engine [9]. High CR with a stoichiometric charge increases the temperature of combustion, which can increase thermal-NO_x formation [7]. To address this, the charge is diluted with exhaust gas recirculation (EGR) and/or the charge is made leaner with reduced fuel to reduce the peak in-cylinder temperatures and mitigate thermal-NO_x formation [7]. The resulting high-CR can reach similar operating pressures with less fuel [10]. Therefore, lean and/or diluted combustion of GCI can result in a large increase in fuel efficiency [11]. One of the disadvantages of GCI is that the temperature and chemical composition within the engine cylinder must be tightly controlled to maintain stable operation. This introduces a new problem, how do researchers accurately monitor, predict, and control engines operating in tighter regimes.

Today, engineers evaluate and design engines by using predictive computational fluid dynamics (CFD) simulations; however, the development of accurate simulations must be iteratively

validated with data from collaborative and comprehensive experiments. Accurate simulations of the in-cylinder conditions result when simulators consider all the relevant, complex, and inter-dependent physics, but consideration of these physics can drastically increase computational expense. However, the next generation of high-efficiency engines, such as GCI, will result from the most accurate simulations of the in-cylinder dynamics.

1.1.2 Motivation for the presented study

Historically, the molecular radiation of H_2O and CO_2 has been considered unimportant to engine heat transfer. Soot was considered the dominant source of radiative heat transfer in compression ignition (CI) engines [12], [13]; however, recent simulations that solve the radiative-transfer equation for many individual photons in a CI engine have shown that molecular emissions can outweigh soot emissions [14], [15].

Radiative heat losses in spark-ignition (SI) engines were considered negligible due to the absence of soot, but these new revelations from CI simulations have put this assumption into question. The widespread use of EGR to mitigate the downsides of higher peak pressure suggests that understanding radiative heat transfer may be vital to the design of new SI engines. EGR consists principally of inert gases (H_2O and CO_2) that are strong emitters and absorbers in the infrared (IR) band. Simulations of high-pressure turbulent flames have shown that >80% of emitted radiation can be reabsorbed before reaching the flame boundary [16]. The resulting energy redistribution can lead to changes in local temperatures of 50-100 K [14]. Meanwhile, increasing engine efficiency requires operating closer to the limits of stable combustion, where slight changes in local conditions are important.

Engine simulations must incorporate models of molecular radiation and reabsorption. Models describe the influence of specific physical phenomena, in this case molecular radiation. Engine

simulations use a variety of models to account for the influence of all relevant physics. These models are often interdependent, so inaccurate models can dramatically alter the results of a simulation. Still, these models must not be too computationally expensive to limit their usage to purely academic research. The implementation and validation of such models require detailed experimental data, which is sparse in the IR bands where H_2O and CO_2 emit strongly. This work presents the development and results of an experimental study of the spectral emissions of combustion products from a flat-flame burner and within an optical SI engine. The engine work also provides detailed information about intra- and trans-cylinder radiative heat transfer, which will aid the validation of accurate simulations of these phenomena.

This technique used a coupled high-speed IR camera and a dispersive grating spectrometer to capture crank-angle resolved spectra at ~4.5 kHz framerates. Different gratings provided varying spectral resolutions allowing for broadband spectra covering 1.0 μm or 0.46 μm. This setup is aligned through a series of optics and stages to both a turbulent methane-fueled flat-flame burner and the propane-fueled, spark-ignited, third-generation Transparent Combustion Chamber (TCC-III) engine, which has a cylinder liner and piston window made of fused silica and sapphire respectively [17]. The repeatability of the flat-flame in the burner makes it useful for model validation of flame radiation at atmospheric pressures. The simple geometry of the TCC-III engine—flat piston top and head, one intake valve, one exhaust valve—making it simpler for modeling validation of a high-pressure combustion system. This document describes the experimental setup used to measure these radiative emissions, shows results from the burner and engine operating at a variety of conditions, and provides information pertinent to the consideration of molecular radiation in combustion environments.

1.2 Engine Heat Transfer Research

Heat transfer in internal-combustion (IC) engines is an innately complicated problem. The combination of a turbulent, compressible, chemically reacting flow with moving boundaries makes it challenging to solve fully from first principles. Engineers have long sought to improve engine efficiency by reducing engine heat loss, but solving all the relevant physics is still intractable. Meanwhile, empirical correlations have guided engineering decisions in engine design. Simulations must accurately model relevant physics, but many of the current models are not of satisfactory accuracy. This is evidenced by continuous research into improving wall modeling [18], turbulence-chemistry interactions [19], and other physical phenomena. Models must be revisited, improved, and validated to assure that simulations are accurate. The presented body of work aims to review the historical assumption that molecular emissions are negligible in engines and to provide new experimental insight into infrared molecular emission in SI engine operation. The following sections explain the development of the "negligible molecular radiation" assumption, followed by a section describing recent studies leading to the re-evaluation of this assumption.

1.2.1 Historical development of radiative heat transfer assumptions (1920-2000)

Since the 1920s, efforts to increase engine efficiency have led to the study of heat transfer in internal-combustion engines (ICEs). The amount of energy lost to the cylinder walls, piston surface, and the head of the engine is significant, and production engines are designed to reduce this energy loss [13]. Heat transfer to the engine cylinder can vary dramatically throughout the cycle, reaching peak fluxes in the 5 MW/m^2 range, and the heat flux changes significantly based on the location within the cylinder [20]. This led initial engineers to develop global models of the overall heat transfer rather than attempt to calculate it at all locations.

A series of empirical models were used as preliminary correlations of engine heat transfer based on Newton's law of cooling:

$$q" = h(T - T_w)$$

Where $q"$ is the heat flux, h is the heat-transfer coefficient, and T_w is the temperature at the wall. An initial model was created using experimental data of a spherical bomb in collaboration with real engine data [20]. This approach split the heat transfer coefficient into its convective and radiative components. Woschni created one of the most commonly used correlations for heat transfer in engines [20]. This study used thermocouples measuring the piston wall temperature to calculate the heat transfer coefficient. This method showed significant differences attributed to the local difference in temperature throughout the spherical chamber [20]. These measurements showed local heat transfer coefficient differences of over 100%. This explained why single point measurements could not provide accurate global heat transfer measurements, and at the time of the studies the computational tools to calculate heat transfer throughout the engine were not available. To circumvent this lack of information a semi-empirical correlation was created, the Woschni heat transfer coefficient.

$$h = 110[d^{-0.2}p^{-0.8}(C_1 c_m)^{0.8}T^{-0.53}]$$

where d is the characteristic length and C_1 is a constant that is usually experimentally determined from the engine. This correlation corroborates experimental data performed with a modified test engine operated with steady-state conditions. The correlation grouped all heat transfer effects. The influence of radiation and its T^4 dependence cannot be isolated from this correlation. However, other researchers explained the need to examine engine heat transfer through its constitutive parts: convection and radiation [13]. At the time, convective heat transfer was measured to make up 90%

of the total heat loss in SI engines making it the most relevant form of heat transfer to study in-depth [13].

With the focus on convective heat loss, fewer studies examined radiation. Engine radiation originates from two sources: soot luminosity and molecular combustion-product radiation. Ebersole *et al.* performed one of the seminal soot radiation studies [21]. This work aimed to separate the different components of engine heat transfer by using a thermocouple to measure the in-cylinder heat flux in a covered and uncovered setting, which would isolate the influence of radiant heat flux. The study concluded that radiation accounted for 5-10% of the total heat transfer for low engine load and 35-45% of total heat transfer at maximum engine load. However, this setup lacked the spectral information to distinguish heat flux due to soot and molecules and attributed most of the radiative heat flux to soot. This focused radiative studies on CI engines which have higher amounts of soot particle radiation, and removed emphasis from molecular gas radiation [12].

Other studies of CI engine soot radiation showed the soot radiant heat flux accounted for up to 50% of the total heat flux reaching the engine walls [22]. These experiments showed that radiative heat transfer increased with higher speeds, higher loads, increased manifold pressures. The change in the equivalence ratio caused a significant change in the apparent heat flux, a trend further explored in this work [23]. The common assumption remained that "radiation is also emitted by carbon dioxide and water vapor molecules but it is concentrated in narrow spectral bands and its magnitude is assumed to be much smaller than that of soot particles" [24].

Early computational studies of radiation in homogenous charge SI engine, where soot luminosity is minimal, showed it accounted for a total radiant fraction, $\frac{Q_r}{Q_{tot}}$, of ~10% [13]. This small contribution was deemed less relevant as convective heat transfer modeling was still

imperfect. However, there was interest in understanding the crank-angle development of the radiant fraction. One of the limitations of experimentally studying molecular gas radiation is that most molecular radiation occurs in the infrared (IR) where accurate, high-speed detection hardware was limited and expensive. Experimental and computational hardware has dramatically improved. Convective heat transfer is measured and modeled in complex ways including particle image velocimetry [25], large eddy simulations [26], and laser absorption spectroscopy [27]. IR hardware has also recently proliferated, research breakthroughs have lowered cost [28], and the high-speed study of molecular radiation in combustion is now possible [29].

1.2.2 Recent developments in radiative heat transfer in engines (2000- 2020)

In a comprehensive review of engine heat transfer, Borman *et al.* suggested several pathways for future work in understanding radiative heat transfer in engines [13]. One suggestion is experiments and simulations that further explore the directional and spectral components of radiation in engines. Data from a spectral experiment would provide sensitive tests from which to validate and develop models, and models could shed light onto the radiant fraction as a function of time and species. Computational tools have improved and allowed researchers to simulate radiation spectrally and directionally. This was complicated due to the complex geometry, changing boundaries, and complicated flows involved in engine simulations, but additionally challenging because radiation must be considered at all locations and its impact must be coupled into the resulting fields. To completely account for radiation is computationally expensive and has been avoided by many engine modeling studies. The study of radiation requires the solution of many radiative transfer equations (RTE) wherever radiation is expected to travel, e.g., throughout the entire combustion chamber.

Struwe *et al.* performed an experimental study of radiation with a self-cleaning radiation probe embedded into an exhaust valve of a Cummins N14 series diesel engine [30]. This study provided measurements of the full hemispherical in-cylinder radiation at crank-angle resolutions for different operating conditions and speeds. The peak radiation was around 2 MW/m^2 and the radiative behavior was seen to be primarily dependent on the engine load.

Wiedenhoefer *et al.* studied a computational approach to radiation utilizing a discrete ordinates method (DOM) to simplify the directional component of radiation [31]. The solid angle circumscribed by the radiation was discretized into solid angle components or "ordinates" which vastly reduced the number of solid angles radiation that must be considered. This DOM method was validated against the results of the previously described radiative experiments [30]. The model did not capture the crank-angle development of radiation well, often having a lower peak heat flux and a later peak radiation location. This study used the developed computational method to evaluate the impacts of radiation on pollutant formation and wall temperatures. NO_x and soot formation in the simulated diesel engine was seen to drop when radiation was considered; however, the overall heat loss was seen to increase significantly. This model was revisited and improved, but the DOM still was unable to predict the radiative heat flux satisfactorily [32].

One accurate method of calculating radiation is the photon Monte Carlo line-by-line method (PMC-LBL) [33]. This approach statistically determines the radiative behavior by solving the RTE for a statistically significant number of individual photons. PMC-LBL is well suited for radiative problems where the radiative properties differ throughout the region of interest, and where analytical solutions to the radiative heat transfer become too computationally expensive. This method traces the history of random photons from where they are emitted to where they are absorbed and, with enough simulated photons, creates an overall understanding of the radiative

field. The PMC-LBL method has been used as the benchmark for the development of other radiative models in the study of turbulent flames [34], [35]. Simplified models are often impeded by the challenges between optically thick and thin regimes. For optically thin media the simplest radiative model, a single elliptical PDE with a gray absorption, was seen to be satisfactorily accurate, but the optically thick regime changes the model's accuracy significantly [34]. Therefore, the PMC-LBL model has been used as the benchmark for in-engine radiative simulations as described below.

Research using the PMC-LBL method has shown the importance of molecular radiation in combustion systems [14]. Initial modeling studies of high-pressure turbulent flames have shown that radiation from a flame under engine-like conditions can have 75-90% of its emitted radiation come from CO_2. This same study showed that the broadband soot radiation component only accounted for 0.3-6% of the total emitted radiation. Also, the simulations demonstrated that the majority of the CO_2 radiation is reabsorbed before reaching the edges of the domain. These results highlighted that a significant amount of radiative energy is transferred throughout the domain during combustion and that molecular radiation is an essential component of the radiative heat transfer. However, a calculation of radiant fraction, $\frac{Q_{rad}}{Q_{fuel}}$, highlighted that the total radiation reaching the walls only amounted to ~4% of the initial fuel energy for a case with an initial gas temperature of 1200K; while molecular radiation is a significant component of the total radiation and energy redistribution it does not always constitute a large component of the overall heat loss.

The PMC-LBL method was applied in several CI engine studies to evaluate the impact of radiation on other operating conditions. One such study summarized that the soot radiation was significant early in combustion, but that gas radiation was the most significant source of radiation overall [36]. A detailed study of radiation in a heavy-duty CI engine used the PMC-LBL method

to investigate the spectra within the engine and used synthetic EGR to see the impact of radiative trapping [37]. The results showed that total radiative emissions equal one-third to one-half of the wall-boundary convective heat loss, but 80-90% of this radiation is reabsorbed before reaching the boundary. So radiative heat loss was only 10% of the overall heat loss. Radiative reabsorption was seen to cause local temperature changes of up to ±60 K near the piston wall. These temperature changes can change the local fluid density and thus impact the local velocity, turbulent viscosity, convective heat loss, and pollutant formations. The engine-out soot and NO_x changes changed around 10% in this study, but the author describes a need for additional research into the impact of radiation on soot formation. This computational study also acknowledges the complex spectral interactions in two specific spectral bands: the CO_2 band (4-5 μm) and the CO_2-H_2O overlap band (2.5-3.2 μm). The radiative energy spectrum is currently accessible in simulations only from using the PMC-LBL method.

Simulations have provided needed insight into the impacts of radiation using the PMC-LBL model, but currently it is not feasible to perform full PMC-LBL simulations coupled with CFD simulations. Therefore, simplified models of the radiative heat transfer have been an ongoing focus. Recently, a method took the lessons of the PMC-LBL method to create a "stepwise gray" model which saw superior performance [35]. This model was formulated by separating the entire wavelength spectrum into five discrete wavelength bands and calculating an average absorption coefficient, κ_λ, for each band. The bands with high κ_λ correspond to the CO_2-H_2O overlap band (2.5-3.2 μm) and the CO_2 band (4-5 μm). The resulting model required ~3% of the computational time as the PMC-LBL model but provided results within 10% of the PMC-LBL model [35]. However, this model's wavelength bands are calibrated for the test case, and the performance of this stepwise gray model is inadequate for other test cases [38].

This renewed interest in simulating radiative heat transfer (RHT) in engines has led to many insights. Still, the lack of high-speed experiments of RHT limits the general benefit of these studies. The PMC-LBL method must be validated for these types of combustion systems with experiments. The influence of molecular gas radiation has been seen to outweigh soot radiation in CI engines and significantly change in-cylinder conditions; however, the molecular gas radiation hasn't been measured. The complex spectral inter-dependences in the CO_2 band (4-5 μm) and the CO_2-H_2O overlap band (2.5-3.2 μm) must be explained, and the directional nature of this radiation must be evaluated. The understanding of these interactions can only occur through coupled simulations and experiments. These questions are explored in this dissertation, and through the presented work, it becomes clear that radiative heat transfer is a complex and essential component of the total engine heat transfer.

1.3 Guide to this Thesis

This thesis describes the creation of an experimental technique meant to examine the importance of molecular radiation in combustion systems. This document – using guidance from recent computational work – presents the development of an experimental methodology to measure infrared molecular emissions from combustion systems. Subsequently, the experimental technique is utilized to measure radiation from two unique combustion systems to characterize the molecular radiative emissions. Insights from measured molecular radiation spectra allow the re-evaluation of previous heat transfer assumptions, provide accurate measurements for the validation of radiative models, and inform a conceptual model of molecular radiation in combustion systems.

This thesis is presented in seven chapters. Chapter 1 provided the necessary context and background to motivate the body of work. Chapter 2 provides the theoretical information needed to understand the production and evaluation of the data. Chapter 3 provides information about the

experimental devices used throughout the different studies and discusses the ways that the data is processed and corrected. Chapter 4 shows the experimental data from the flat flame burner, which contains the exploration of the important molecular features and their relative influence at atmospheric pressures across a variety of operating conditions. Chapter 5 provides results from a comprehensive validation study of molecular radiation simulations with experimental data and provides a concrete quantitative understanding of the influence of radiative trapping. Chapter 6 presents the dataset of different engine operating conditions. This chapter evaluates the experimental data to explore correlations pressure and heat flux, analyze spectral characteristics, and discuss their implications on engine behavior. Finally, Chapter 7 provides the conclusions of this dissertation and provides avenues for continued/ongoing research into the molecular radiation in combustion systems.

Chapter 2 Theory

The presented work relies on the theory of spectroscopy and radiative transfer. This chapter introduces the needed theory and expressions to describe the methods and results of this dissertation. Firstly, an introduction of rotational and vibrational spectroscopy which explain the emitted and absorbed radiation. Secondly, the theory of radiative heat transfer, which describes how the emitted radiation travels through the combustion environment and how it is absorbed. Additionally, the radiative transfer theory provides a macroscopic understanding of this behavior. This chapter will provide the needed background for the remainder of this dissertation.

2.1 Spectroscopy Theory

2.1.1 Wavelength Ranges of Interest

IR radiation seen in combustion is often connected to the rotational-vibrational transitions due to the high-temperature combustion reactants and products. The majority of the thermal emission takes place within the IR. For example, a blackbody-like emitter at 2000 K will have peak emission at around 1.45 μm and more than 90% of its emission in the IR [39]. There are five subcategories of the IR: the near-IR (0.75-1.4 μm), the short-wavelength IR (1.4-3 μm), the mid-wavelength IR (3-8 μm), the long-wavelength IR (8-15 μm), and the far IR (15-1000 μm). The near-, short-wave, and mid-wave IR are the wavelength regions most important to combustion research. IR wavelengths from 0.75-8 μm capture the large majority of relevant IR radiation due to combustion. The majority of past IR combustion research focused on near- and short-

wavelength IR [40]. New measurement technology provides access to the mid-wavelength, long-wavelength, and far IR for more accurate measurements [41]. HITRAN 2012 calculations [42] show combustion relevant species (H_2O, NH_3, CO_2, CO, CH_4, NO) in the near- to long-wavelength IR, and the strongest emissions can be seen from 1-8 μm [40].

2.1.2 Rotational and Vibrational Spectroscopy Theory

Spectroscopy is based on the quantum mechanical concept that energy is quantized, and that by monitoring the discrete energy levels of a molecular species we can discover information about the properties of that molecule [43]. Energy leaves or enters the molecule in the form of a photon at a specific wavelength. The energy of a photon is described as follows:

$$E = h\nu = \frac{hc}{\lambda}$$

where h is the Planck constant, c is the speed of light, ν is the frequency, and λ is the wavelength. As illustrated in Figure 2-1, when a molecule is excited by absorbing a photon, it transitions to a higher energy level corresponding to that photon's energy. Likewise, when a molecule changes from its elevated energy level to a lower energy level it emits a photon of corresponding energy. Transitions between different vibrational and rotational states of a molecule result in IR absorption or emission [43].

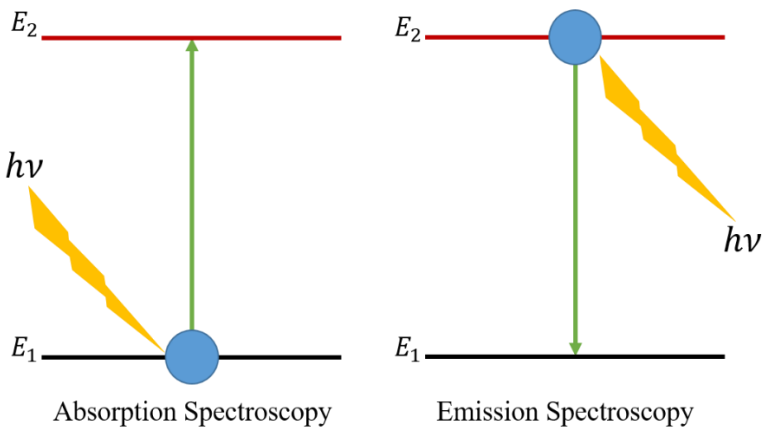

Figure 2-1: Diagram of the difference between the two types of spectroscopy

In a simple model, molecules are treated as atomic masses (nuclei) connected by a spring (chemical bond). A molecule vibrates when the masses move towards and away from each other at a certain frequency. The energy of the system is defined by how stretched or compressed the spring is during vibration. Figure 2-2 demonstrates the potential internal energy curves of a diatomic molecule. As seen in Figure 2-2 there are three different transition types: electronic, vibrational, and rotational.

Electronic transitions represent the highest energy transitions where the internal energy of the molecule rises or drops an entire electronic potential level [44]. Figure 2-2 illustrates an electronic transition with the red arrow. The high-energy nature of these electronic transitions leads to high-frequency radiation which is usually in UV-visible wavelengths [45]. Vibrational transitions are due to the discrete vibrational modes of certain molecules, and the radiation associated with these transitions is often in the IR. Vibrational transitions are the second highest energy transitions possible as seen by the blue arrow in Figure 2-2. Finally, there are specific and limited ways that a molecule can rotate; the rotational transitions are dictated by that rotation. The rotational transitions are the lowest energy transitions of the three types considered here and are shown with the black arrow in Figure 2-2. Usually, rotational and vibrational transitions occur

simultaneously, which necessitates the usage of rotational-vibrational spectroscopy theory to understand the spectrum [45].

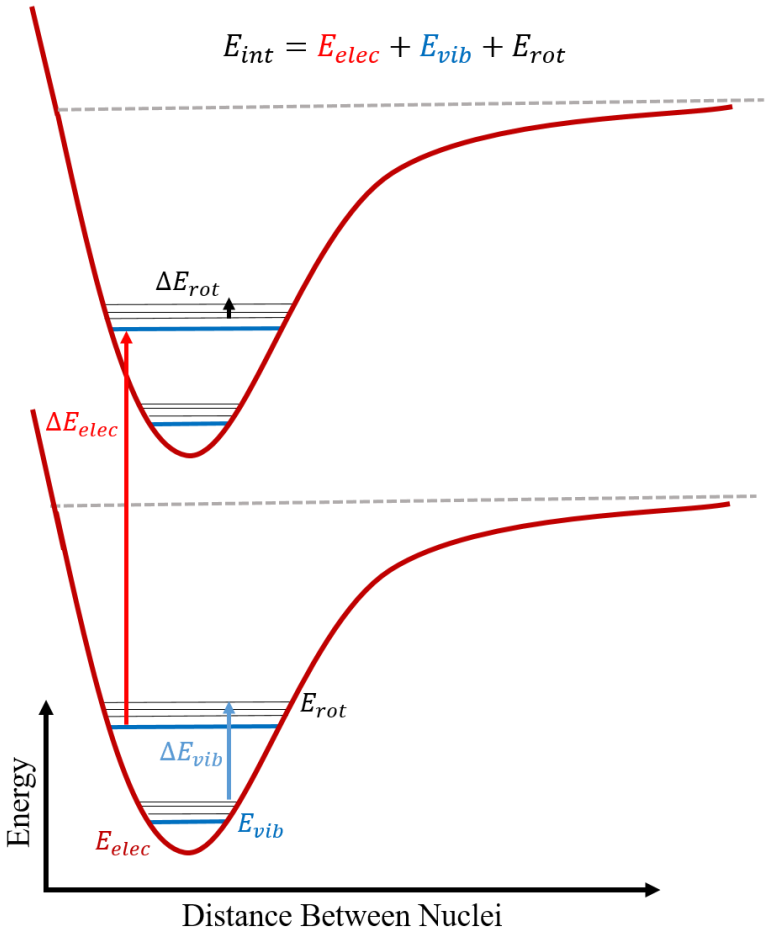

Figure 2-2 Energy against the distance between nuclei for a diatomic molecule. Three different types of energy levels, electronic, vibrational, and rotational are labeled in different colors.

The viable vibrational transitions of any molecule can be determined by examining its degrees of freedom. A single atom can be located with three coordinates such as X, Y, and Z in the Cartesian system. For a molecule, each atom has three available coordinates. Therefore, a polyatomic molecule of N atoms will have 3N degrees of freedom. However, the entire molecule's translation and rotation are described by six degrees of freedom. The remaining degrees of freedom are associated with the internal vibrations of the molecule. Non-linear molecules have M fundamental vibrations described by the equation [46]:

$$M = 3N - 6\ (non - linear\ molecules)$$

For linear molecules, there is no rotation about the bond axis; hence, only five degrees of freedom are needed to describe the translation and rotation. Therefore, the following equation describes the M fundamental vibrations of a linear molecule:

$$M = 3N - 5\ (linear\ molecules)$$

In engine-relevant conditions, the primary participating species are CO_2 and H_2O. H_2O is a nonlinear molecule, so it has three vibrational modes, and CO_2 is a linear molecule, so it has four vibrational modes. A diagram of these fundamental vibrations is shown in Figure 2-3. As seen in Figure 2-3, CO_2 vibrations υ_2 and υ_4 are degenerate vibrations that are identical except that they occur on axes perpendicular to each other (one occurs up and down the other in and out of the page). Multiple vibrational modes can occur simultaneously so the molecule may exhibit a combination or difference of several vibrational modes, and multiples of the fundamental vibrations, known as overtones, can occur [43]. Symmetric bonds, such as in O_2 and N_2, are IR-inactive so they do not impact the radiative behavior in combustion [47].

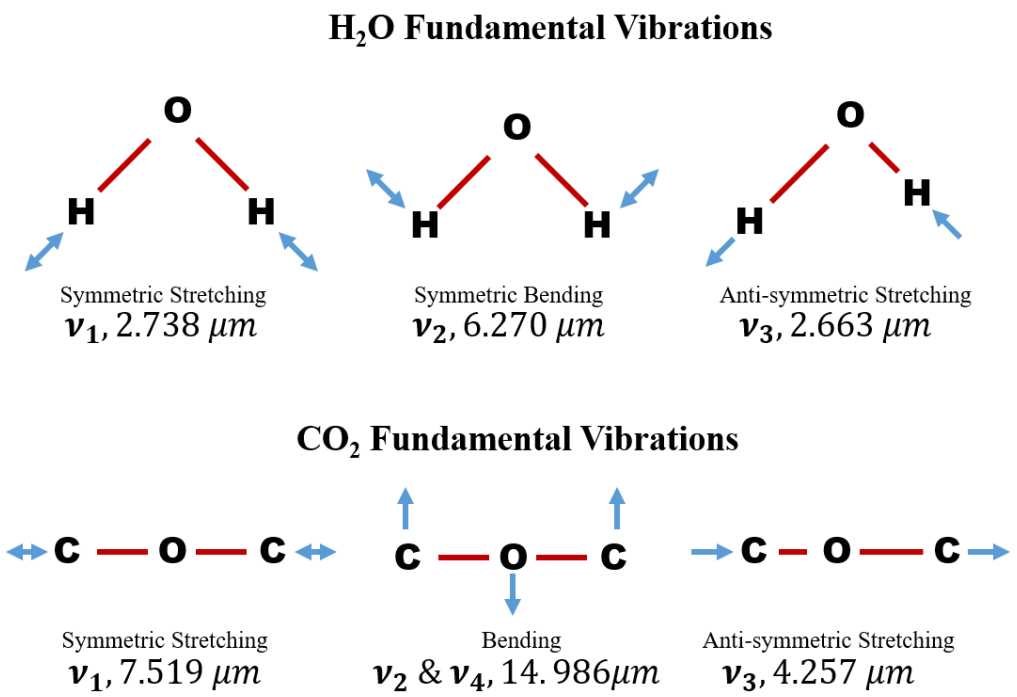

Figure 2-3: fundamental vibrations of H_2O and CO_2

The discrete nature of molecular energy levels builds the foundation of spectroscopy. However, there are several rules used to describe the available transitions. For ro-vibrational spectroscopy the discrete energy levels are described by quantum numbers. For a simple harmonic oscillator model the vibrational energy is described by the following equation [48].

$$E_\nu = \frac{hc}{\lambda}(\nu + \frac{1}{2})$$

where ν represents the quantum number for vibrational energy levels and λ corresponds to the wavelength of the vibration. Similarly, for a simple rigid rotor the rotational energy is described in the following equation [48].

$$E_r = \frac{h^2}{8\pi^2 I} J\,(J+1)$$

Where J represents the quantum number for rotational energy levels and I is the molecules moment of inertia. The selection rule constrains the different transitions between energy levels that can occur [43]. For vibrational transitions, the rule states $\Delta\nu = 0, \pm 1, \pm 2, \ldots$ are allowed, which means that the vibrational energy level can go up or down more than a single vibrational energy level at a time. However, the strongest transitions are $\Delta\nu = 0, \pm 1$. This rule is superposed with the rotational selection rule, which similarly states $\Delta J = 0, \pm 1, \pm 2, \ldots$, meaning that rotation is constrained in the same way. These vibrational and rotational transitions often occur together forming the basis of ro-vibrational spectroscopy. Ignoring electronic transitions, the change in internal energy of a molecule can be seen as the sum of the energy of the rotational transition and the vibrational transition.

$$\Delta E_{int} = \Delta E_r(J) + \Delta E_\nu(\nu)$$

Rotational transitions are of much lower energies than vibrational transitions, but there are many rotational transitions available between viable vibrational transitions, as illustrated in Figure 2-2. Due to this, ro-vibrational diatomic spectra exhibit bands. Bands are the group of lines with a common vibrational transition but different rotational transitions. Since these bands share a vibrational energy level, the emitted or absorbed radiation from these transitions are of similar wavelengths. An illustration of the band structure resulting from a diatomic molecule is shown in Figure 2-4. This figure shows the fundamental band of carbon monoxide, with the fundamental vibrational transition occurring at υ_0, and the additional rotational transitions occurring surrounding this transition. The R branch represents the vibrational transition occurring with a simultaneous increase in rotational energy level, $\Delta J = +1$. The P branch represents the vibrational transition occurring with a simultaneous decrease in rotational energy level, $\Delta J = -1$. Polyatomic vibrations also exhibit band structures, but they can have an additional Q branch where vibrational

transitions occur without a rotational transitional. To capture the detailed rotational line structure requires a device with a high spectral resolution [43]. The measurement apparatus used for the presented experiments does not have the spectral resolution required to capture the rotational fine structure, and the combustion environment influences spectral lineshape broadening. Therefore, the presented spectra show a contour of the ro-vibrational band rather than individual ro-vibrational transitions.

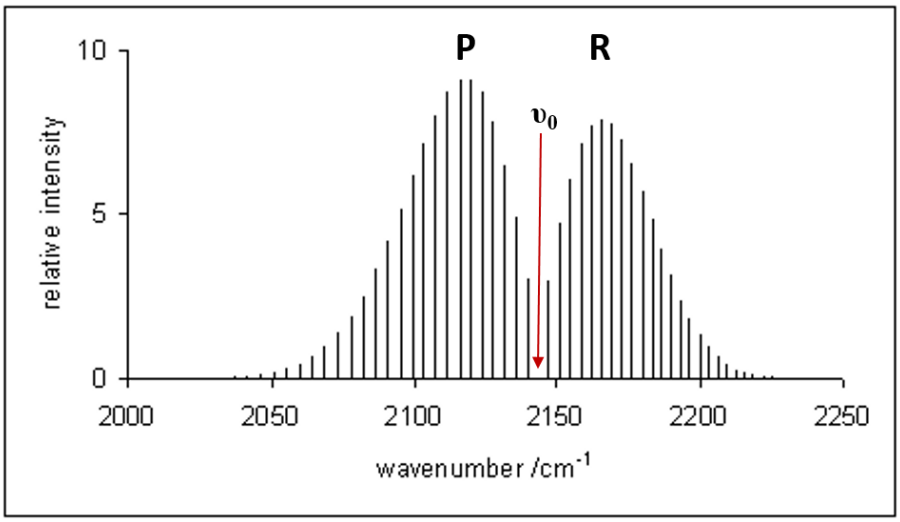

Figure 2-4: Ro-vibrational Spectrum of the fundamental band of carbon monoxide. Labeled with R and P bands [43].

The high-temperature and high-pressure combustion environment lead to spectral line broadening. The presented research is influenced by broadening mechanisms in combusting gases, and the most relevant mechanisms are the collisional broadening and thermal broadening effects which depends on the pressure and temperature of the gas respectively [49]. Pressure broadening occurs when collisions disturb the energy transitions of molecules, thus leading to movement of the transition wavelength [50]. Thermal broadening occurs due to the motion of molecules in the mixture. This molecular motion is directly connected to the temperature of the mixture, and the movement can cause the broadening of the molecular band. As a molecule travels towards the detector it causes the transition wavelength to shorten slightly (blue-shift); as a molecule travels

away from a detector it causes the transition wavelength to lengthen slightly (red-shift). Therefore, high-temperature mixtures will have fast traveling molecules and will present broader spectral lines. The impact on the spectral lineshape due to pressure and thermal broadening can be described by a Lorentzian profile [42].

2.1.3 Relevant Ro-vibrational Transitions

Wavelengths from 1-5.5 μm are examined throughout this dissertation. H_2O and CO2 are the primary emitters in this wavelength region. The relevant H_2O vibrations and CO_2 vibrations are described in Table 6-4 [51]. It is important to note that the fundamental vibrations (boldface in Table 2-1) often have the highest population and thus have the strongest intensity bands. The strongest emissions from 2.4-3.4 μm, due to the υ_1 and υ_3 vibrations of H_2O, and from 4-5 μm, due to the υ_3 vibration of CO_2 are the focus of the dissertation work.

Table 2-1: Relevant H_2O and CO_2 vibrations across the entire measured spectrum, 1-5.5 μm. Fundamental vibrations in boldface.

λ_{H_2O} $[\mu m]$	H_2O Vibration	λ_{H_2O} $[\mu m]$	CO_2 Vibration
1.14	$\nu_1 + \nu_2 + \nu_3$	1.96	$2\nu_1 + \nu_3$
1.38	$\nu_1 + \nu_3$	2.01	$\nu_1 + 2\nu_2 + \nu_3$
1.45	$2\nu_2 + \nu_3$	2.06	$4\nu_2 + \nu_3$
1.88	$\nu_2 + \nu_3$	2.69	$\nu_1 + \nu_3$
2.66	$\boldsymbol{\nu_3}$	2.77	$2\nu_2 + \nu_3$
2.73	$\boldsymbol{\nu_1}$	4.26	$\boldsymbol{\nu_3}$
3.17	$2\nu_2$	4.82	$\nu_1 + \nu_3$
		5.17	$3\nu_2$

2.2 Radiative Transfer

2.2.1 The Radiative Transfer Equation

The equilibrium radiative transfer equation (RTE) in a medium that absorbs, emits, and scatters is expressed as [33]:

$$\frac{dI_\lambda}{ds} = \kappa_\lambda I_{b\lambda} - \beta_\lambda I_\lambda + \frac{\sigma_{s\lambda}}{4\pi}\int_{4\pi} I_\lambda(\hat{s}')\Phi_\lambda(\hat{s}', \hat{s})d\Omega'$$

here $I_{b\lambda}$ is the blackbody radiative intensity (a known function of wavelength and temperature), I_λ is the spectral radiative intensity, $\hat{s}$ describes the unit direction ($\hat{s}'$ represents incident direction for the integral which considers scattering), κ_λ is the spectral absorption coefficient, $\sigma_{s\lambda}$ is the spectral scattering coefficient, $\beta_\lambda = \kappa_\lambda + \sigma_{s\lambda}$ is the spectral extinction coefficient, and Φ_λ represents the scattering phase function. Φ_λ is used to describe the probability of in-scattering from the $\hat{s}'$ direction into the $\hat{s}$ direction. However, in this work and the accompanying computational work using the PMC-LBL model, the combustion medium is considered to be non-scattering ($\sigma_{s\lambda} = 0 \ \therefore \ \beta_\lambda = \kappa_\lambda$). This assumption is made because there is little to no scattering media (fuel and oil droplets, soot, etc.) so the overall in-scattering contribution will be low [52]. The non-scattering assumption leaves a simplified RTE:

$$\frac{dI_\lambda}{ds} = \kappa_\lambda I_{b\lambda} - \kappa_\lambda I_\lambda = \kappa_\lambda(I_{b\lambda} - I_\lambda)$$

2.2.2 Radiative Absorption

There are two methods for IR spectroscopy to gain insight into the combustion properties. One is to measure the absorption of the combustion mixture by probing the species with photons, usually with laser radiation. The probing radiation will be absorbed if the radiation is of the right frequency to interact with the molecules in the mixture. Absorption measurements evaluate the

radiative energy before and after passing through a sample to determine absorption. Absorption can be used to determine an array of different quantities such as temperature and molecular concentration [40].

Using the previously defined simplified RTE, the equations underpinning absorption experiments can be derived. If the simplified RTE is integrated over a pathlength, L, the integrated form of the radiative transfer equation gives the following equation.

$$I_\lambda = I_\lambda^0 \exp(-k_\lambda L) + I_{b\lambda}[1 - \exp(-k_\lambda L)]$$

where I_λ^0 is the incident intensity. For absorption experiments the gas is probed with high power monochromatic light, usually from a laser, which has much higher probing radiation than the natural intensity, $I_{b\lambda}$, of the gas.

$$I_\lambda^0 \gg I_{b\lambda}$$

This leads to the foundational equation of absorption spectroscopy resulting from the absorption principle described above. The resulting equation used to describe absorption experiments is known as the Beer-Lambert law [53]:

$$I_\lambda = I_\lambda^0 \exp(-k_\lambda L)$$

The Beer-Lambert Law is illustrated in Figure 2-5. This basic relationship is true for any length where k_ν is constant, or it provides a path-averaged absorption.

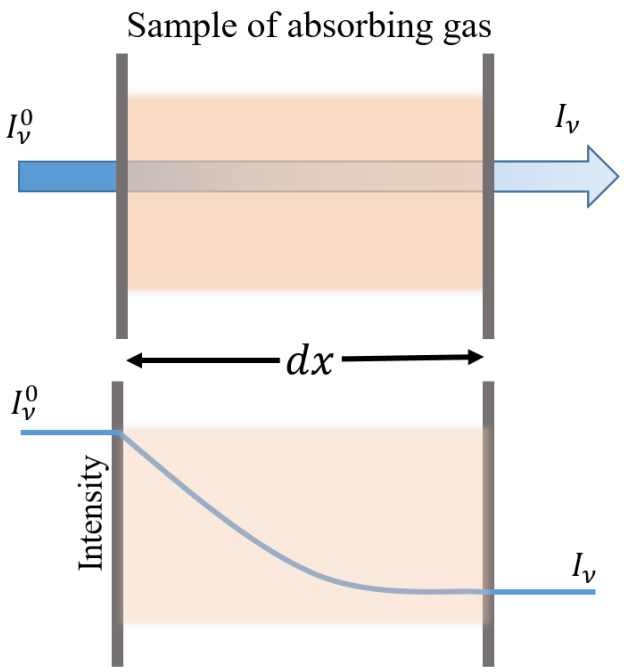

Figure 2-5: Example of absorption spectroscopy experiment

The following relationship of the absorption coefficient is related to the total absorption, $\alpha(\lambda)$. The following equation connects the spectral absorption coefficient to the thermodynamic properties of the mixture:

$$k_\lambda L = \alpha(\lambda) = \sum_j S_j(T) \mathrm{X}_{abs} \phi_j(\lambda, T, P, \mathrm{X}) L$$

$S_j(T)$ is the linestrength as a function of temperature T for a specific transition j; X_{abs} is the mole fraction of the studied gas species; ϕ_j is the lineshape function; and the lineshape is a function of wavelength (λ), temperature (T), pressure (P), and mole fraction (X) [50]. This equation sums the influence of all relevant transitions at a specific wavelength. Researchers rely on accurate databases, such as HITRAN and HITEMP, that have tabulated spectral linestrength and lineshape data to back out the thermodynamic properties of their measurements [42], [54]. These absorption methods often monitor multiple transitions for correlation with databases or measure a broadband

spectrum to compare with databases for the most accurate fit [55]. Absorption accuracy in combustion was limited by access to spectral databases with accurate models at combustion relevant conditions [56]. These absorption methods have been utilized successfully in engines where laser radiation can be brought through the combustion gases and measured [57], [58].

2.2.3 Radiative Emission

Emission spectroscopy measures spontaneously emitted photons from a combusting species rather than probing with stimulated emissions. The photons emitted by the molecule will be of certain energy which corresponds to a specific transition of a molecule found in the mixture. This method can be used to identify the molecular species in the gas. Emission is a passive technique that is used to determine how different energy levels are populated during combustion and can identify unknown species. Finally, emission spectroscopy can be used to assess how much radiation is naturally released during combustion, which provides a measure of the radiative heat loss.

For emission experiments, we assume there is no external radiation source, $I_\lambda^0 = 0$. Leaving the following relationship to describe the emission of a radiating gas over the pathlength.

$$I_\lambda = I_{b\lambda}[1 - \exp(-k_\lambda L)]$$

The product $k_\lambda L$ is called the optical depth. An optically thick gas ($k_\lambda L \gg 1$) will emit similarly to an ideal blackbody at the gas' temperature, and optically thin gas ($k_\lambda L \ll 1$) will emit much less than an ideal blackbody at the gas's temperature. Similarly, an optically thick gas is opaque and will absorb incoming radiation, and an optically thin gas will act almost transparent with incoming radiation. It is important to note that all of these relationships depend on the wavelength, i.e. CO_2 is optically thick around a wavelength region centered at 4.25 μm but is optically thin otherwise [35]. Around 4.25 μm, CO_2 will absorb incoming radiation and will emit strongly at

high temperatures. Meaning that the strong CO_2 emission seen in radiative simulations is reabsorbed primarily by other CO_2 molecules [37]. Because radiative emission spectroscopy is central to this work the following section describes engine applications of infrared emission spectroscopy.

2.2.4 Applications of Infrared Emission Spectroscopy

Infrared emissions from flames have been spectroscopically studied for many years [45]. Studies dating to 1929 studied Bunsen burner flame emission spectra from 1-7 μm using a rock salt prism spectrometer [59]. This study examined the intensity ratios between the CO_2 feature and H_2O feature and saw and examined the ratios of the CO_2 feature. However, due to the recent widespread availability of inexpensive lasers and open-source spectral databases, the use of absorption measurements has increased dramatically [50]. It is harder to define the exact radiative pathway because emission experiments receive radiation from a solid angle defined by the optics. Nevertheless, IR emission experiments can provide valuable information about radiative heat transfer.

Experimental measurements determining the influence of radiative heat transfer on engine operation must monitor the IR radiative emissions [14]. However, measuring the natural intensity at the engine boundary shows how much radiative heat was transferred to the wall, i.e. an emission spectrum provides the radiative heat loss of the measured volume to the wall. Additionally, emission spectroscopy is inherently single-ended, which simplifies the optical access needed. Discussion throughout this section will address the previous methods that have been used to measure IR engine emission.

The use of Fourier Transform Infrared Spectroscopy (FTIR) provides high spectral resolution data over a large wavelength range [60]. Time-resolved FTIR could not be used in an

engine because it relies on a steady, repeatable sample [61]. Repeatable conditions are not possible in an engine where the engine speeds, molecular concentrations, and thermodynamic properties differ from cycle to cycle [62]. However, emission measurements were achieved by operating an FTIR and an engine in an uncorrelated way for an extended period [63]. The FTIR and engine were simultaneously operated for over 27 thousand engine cycles to populate emission spectra at different piston positions. The produced spectra measured emissions from 1.2-2.2 μm for 3^{o} crank angle steps. Soon after this method was adapted to produce FTIR absorption measurements in an engine [64]. FTIR measurements provide ensemble-averaged spectra so all radiative cycle-to-cycle variation (CCV) is lost, and the long measurement times needed for the FTIR are not possible in an optical engine.

Soot thermometry using the two-color technique has been used extensively to measure temperatures of soot in compression ignition (CI) engines [65] and SI engines [66]. Soot thermometry has also been performed in the IR using InSb and AuGe photodetectors [67]. The typical setup for this experiment is single-ended access to the engine. This technique was performed with infrared emission at 2.3 μm and 3.98 μm, to see if the IR provided similar temperature results to the visible wavelengths. These two wavelengths corresponded to wavelengths where only soot radiation was expected [68]. In this experiment, visible spectrum two-color thermometry measured the high-temperature component of the flame; whereas, the infrared method accurately measured the average temperature of the flame [68]. Due to the highly dynamic emissivity of molecular features seen in combustion, e.g., H_2O, CO_2, and CO_2, this technique has limited application to determine molecular gas temperatures.

Both of these techniques guided the creation of the forthcoming experimental apparatus. The FTIR experiments demonstrated the value of having a large spectral range with good spectral

resolution. FTIR is strongly limited by its slow capturing rate, and an experimental technique that would capture CCV was desired. The soot thermometry technique highlighted the possibility to capture emissions in the mid-wavelength IR using an InSb photodetector. Advances in IR camera technology have made InSb cameras with high framerates at low costs [28]. A traditional InSb sensor measures from 1-6 μm where the relevant ro-vibrational features are emitted [69]. The usage of a high-speed IR camera and a traditional dispersion-grating IR spectrometer provided a pathway to high repetition rates, large spectral range, and acceptable spectral resolution.

Chapter 3 Experimental Approach

This chapter describes the experimental tools and measurement techniques used to measure the radiative emissions of combustion gases. This includes descriptions of the TCC-III optical engine, the Hencken flat-flame burner, the IR dispersive spectrometer, the IR cameras, and other associated optical components. This is followed by the procedure used to calculate and perform the transmission, spectral sensitivity, and background emission corrections.

3.1 Optical Engine

The engine used in these experiments is the third-generation Transparent Combustion Chamber (TCC-III) engine [70],[17]. This engine has a simple pancake chamber with geometry described in Table 3-1. During the experiments included, the engine was operated on a range of operating conditions with a pre-mixed propane/air mixture. The engine was operated at both 500 and 1300 rev/min with an intake plenum pressure of 40 kPa. Exhaust plenum pressures of 98 and 101.5 kPa were used. The ignition timing was -18 degrees after top dead center compression (°aTDC) for all experiments where the engine was fired. The in-cylinder pressure dynamics were measured with an in-cylinder pressure transducer (Kistler 7001) every 0.5 crank-angle degrees (CAD). Additionally, pressure transducers and thermocouples measured the intake and exhaust pressures and temperatures. The real-time combustion analysis system (CAS) was used for analysis and additional post-processing. The crank-angle resolved pressure and temperature measurements were used to provide in-cylinder pressures, apparent heat release (AHR), apparent

heat release rate (AHRR), and other combustion landmarks. These pressure-derived parameters' correlation to the radiative heat transfer in the engine is further explored in Chapter 6.

Table 3-1: Table of engine geometry and relevant parameters [17]

TDC-III Engine Geometry			
Bore, cm	9.20	Connecting-rod length, cm	23.1
Stroke, cm	8.60	Piston-pin offset, cm	0.0
Clearance @ TDC, cm	0.95	Connecting rod offset, cm	0.0
Combustion chamber volume, cc	631.5	Exhaust valve closing, ^{o}aTDC	12.8
Top-land crevice volume, cc	0.37	Intake peak lift, ^{o}aTDC	114.8
Spark-plug crevice volume, cc	0.02	Intake valve closing, ^{o}aTDC	240.8
TDC volume, cc	63.54	Exhaust valve opening, ^{o}aTDC	484.8
Swept volume, cc	571.7	Exhaust peak lift, ^{o}aTDC	606.8
Geometric CR	10.0	Intake valve opening, ^{o}aTDC	712.8
Effective (IVC) CR	8.0	Valve-seat angles, degree	30/45/60/75
Steady-flow swirl ratio	0.4	Spark plug	Denso 4511PT16TT

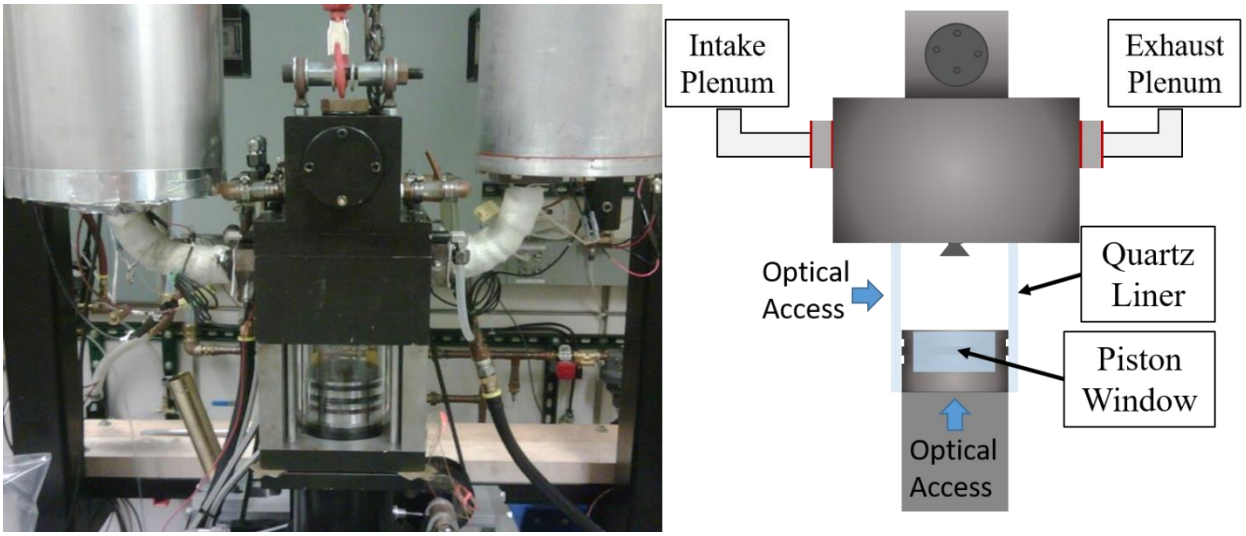

Figure 3-1: Image and diagram of TCC-III optical engine with optical components and optical access labeled. Picture provided from [17].

The engine has two pathways of optical access. A fused silica cylinder liner (Rodriguez Consulting) provides optical access through the sides of the combustion chamber, as seen in Figure 3-1. Additional optical access is available through the specially designed Bowditch extended piston with a sapphire piston window. The Bowditch piston allows optics located within the piston assembly for beam steering [71]. The piston window and cylinder liner can be replaced with different materials. Early engine measurements during this work were made through the fused silica cylinder liner. Later measurements were performed through a sapphire piston window (Guild Optical Associates) in the Bowditch piston. Compared to fused silica, sapphire improves the transmission in the mid-wavelength IR.

Sapphire was a strong alternative for fused silica. Sapphire provides very high strength and superior transmission in the relevant IR wavelengths [72]. A Sapphire piston window allowed measurements of the relevant ro-vibrational IR bands [35]. Sapphire transmits >85 % from 0.3-4.0 µm and has transmission out to ~6.0 µm, whereas fused silica transmits only up to ~3.5 µm.

Sapphire has a thermal conductivity of $30\frac{W}{mK}$, which is around twenty times higher than fused silica and is closer to the conductivity of a metal piston [73]. These properties affect the piston window temperatures and the piston-gas interface.

3.1.1 Heat Flux Measurements

Heat flux measurements were made with a heat-flux probe (Medtherm TCS-233-JU(JU-.156)-72-11340). This probe was located 35.5 mm from the measurement axis. One thermocouple was set at the probe surface and another was set at 3.96 mm into the probe material. Measurements of the heat flux were made ever 0.5 CAD. A complete description of the heat-flux probe and measurement protocol within the TCC-III engine was provided in previous work [18]. The instantaneous heat flux, q_w, was calculated from a relationship between the surface temperature probe and the recessed temperature probe [74]. The uncertainty of this measurement technique demonstrated a standard error of around 5% [18].

3.1.2 Infrared Transmission of Engine Optical Components

The transmission of the materials providing optical access in these experiments was carefully considered. Many previous studies in the TCC-III engine have focused on visible and UV radiation, but the materials used for high transmission in the UV-visible wavelengths may have poor transmission performance in the IR [72]. Moreover, the transmission of the optical materials used can vary strongly due to the manufacturing process. Transmission is a wavelength and temperature-dependent property [39]. Therefore, the transmission was evaluated and corrected for fused silica and sapphire.

The transmission of the fused silica cylinder liner was measured using the spectrometer and camera described in Section 3.4 and a blackbody source (Electro Optical Industries LES800-

04) with a known emissivity. This blackbody source provided an extended area for transmission measurements. The blackbody source exhibits a total temperature fluctuation of ±0.5 ^{o}C when allowed to reach a steady state and a spatial variation of ±1.0 ^{o}C at steady state. The blackbody source was heated to 800 ^{o}C, allowed to reach a steady state, and then the emitted spectrum from 1.5-5.5 μm was measured with and without a sample of the fused silica engine cylinder. The transmission was determined using the following relationship:

$$\tau_\lambda = \frac{I_{\lambda,S}}{I_{\lambda,N}}$$

where τ_λ is the measured transmission of the material at a specific wavelength; $I_{\lambda,S}$ and $I_{\lambda,N}$ are the measured spectral power with and without the fused silica sample respectively. Although the cylinder transmits well across much of the visible wavelengths (not shown on the plot), the near-IR and short-wavelength IR show strong attenuation from 2.75 to 2.9 μm and beyond 4.2 μm as seen in Figure 3-2. As a result, the signal recorded in these bands was weak, and correcting recorded signals for these (low) measured transmission values produced unreliable results for the emission inside the cylinder. However, several relevant ro-vibration bands of H_2O and CO_2, namely those identified as significant in simulated studies [35], were obstructed by the opacity of fused silica.

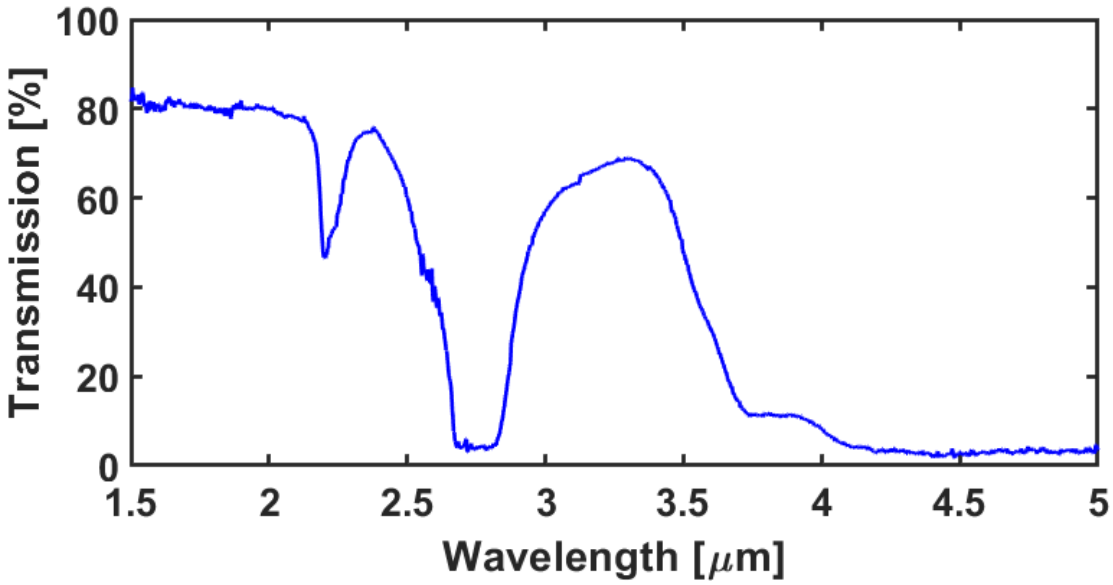

Figure 3-2. The measured transmission of the fused-silica cylinder. The low transmission near 2.8 μm and above 4.2 μm lead to the work described within this document measuring wavelengths below 2.5 μm.

As the blackbody source was no longer available upon receipt of the sapphire windows, transmission measurements were made using an instrumented heating plate (Deni 16310). The heating panel's temperature was monitored with a thermocouple (Omega Type-K Thermocouple) and a thermal controller (Digi-Sense Single Zone Temperature Controller) was used to maintain a constant temperature of 300 ± 8 ^{o}C. The spatial variation of temperature was evaluated by moving the thermocouple and was found to be ±6 ^{o}C across the panel. This device was not able to reach the same high temperature as the blackbody source, but the temperature was sufficient to provide the broadband radiation needed to measure transmittance from 1.5-5.0 μm as seen in Figure 3-3 [69]. The measurements were performed in the same fashion to those described for the fused silica transmission. The data shows strong, uniform transmission, above 90%, until 4 μm followed by a gradual decrease in transmission. Figure 3-3 confirms that sapphire is well suited for IR measurements.

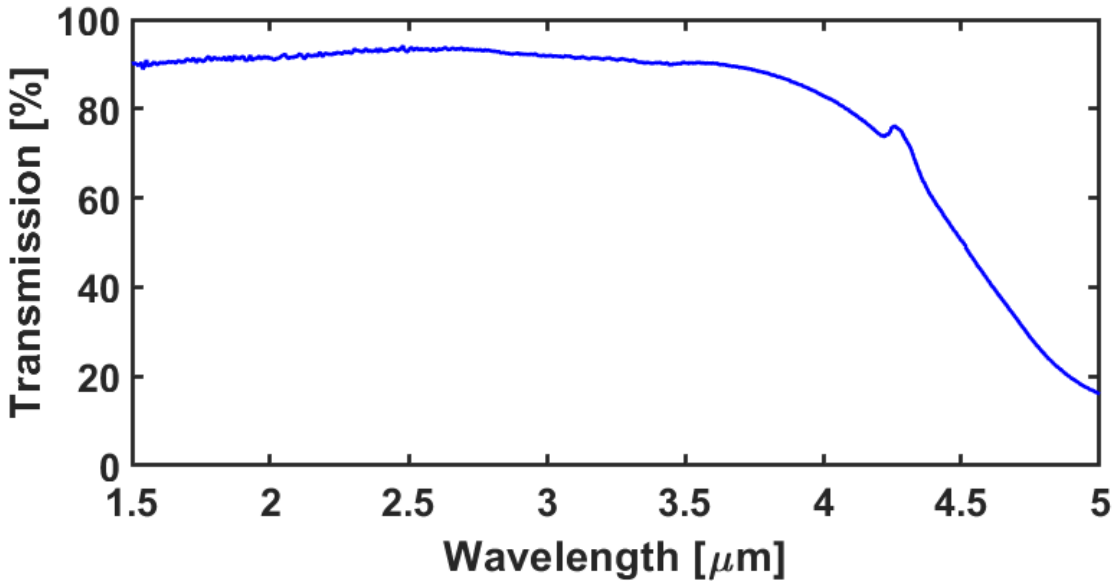

Figure 3-3: The measured transmission of the sapphire piston window. >80 % transmission occurs until ~4 um

The transmission spectrum depends on the temperature of the material, but this study was unable to fully correct for the temperature dependence of transmission. Fused silica and sapphire transmission degrade based on the temperature [75], [76]. Data adapted from Oppenheim *et al.* shows the transmission of an 8-mm thick sample of sapphire at different temperatures in Figure 3-4 [76]. The transmission can be seen to decrease as temperature increases. The following analysis was performed to determine the feasibility of a temperature-dependent transmission correction, and given the needed data a temperature-dependent transmission correction was not performed.

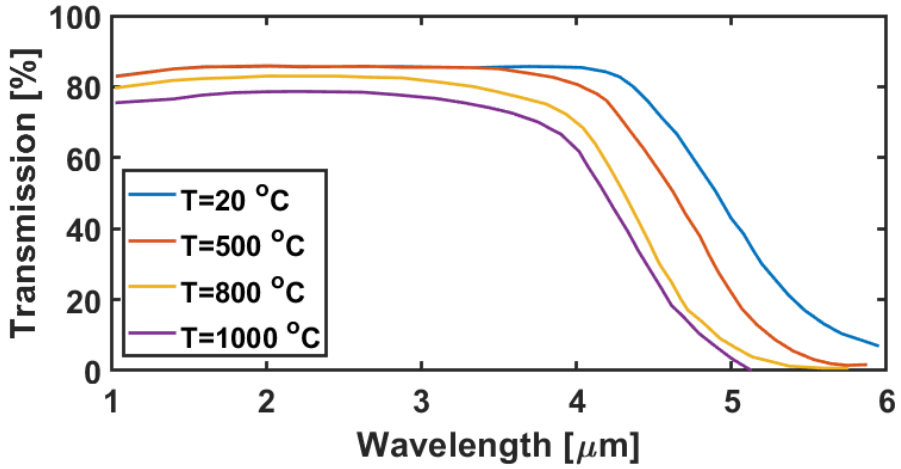

Figure 3-4: Transmittance of 8-mm sapphire sample heated to different temperatures. Data adapted from Oppenheim [76].

Large eddy simulations examining conjugate heat transfer in the TCC-III engine provided information about the material temperatures [26]. Simulation data, provided by Dr. Angela Wu, seen in Figure 3-5, shows the temperature profile across the center point of the fused silica piston window during stoichiometric combustion in the TCC-III engine [personal communication with Dr. Angela Wu]. The engine was simulated operating at 1300 rev/min with a 40 kPa intake pressure. The simulation data, presented at four crank angles, illustrates the temperature profile throughout the cycle. The piston window has a nearly constant temperature profile throughout the cycle. The highest temperature occurs at the piston top (0 cm into piston window) and decreases deeper into the piston window. A difference of ~35 K in piston top temperature occurs -360 °aTDC (lowest plotted temperature) and 0 °aTDC (highest plotted temperature). However, the simulated piston window shows a ΔT of ~500 K across the piston at all simulated CAD. The small changes in piston temperature throughout the cycle would not significantly affect the transmission, but the high-temperature gradient across the piston could impact transmission [77]. Given the higher thermal conductivity of sapphire, $30\,\frac{W}{mK}$, it is likely that the ΔT across the piston would be much smaller. Analysis using Fourier's law suggests a ΔT across the piston window of ~25 K for a sapphire piston window at TDC. However, this simple analysis does not consider the influence of the sapphire piston window on the flow and gas temperature. A transmission measurement of the piston window, heated to match the average piston temperature gradient, could be used to correct the measurements. Regrettably, the simulated piston temperatures do not align with previous literature measuring the piston temperature of similar engines.

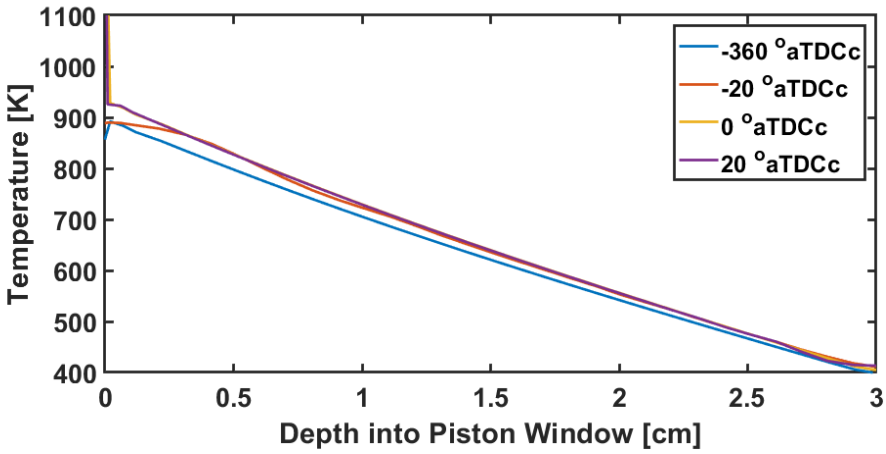

Figure 3-5: Temperature profile across the fused silica piston window at -360, -20, 0, and 20 °aTDC during a simulated firing cycle considering conjugate heat transfer. Provided by Angela Wu.

Previous experiments have measured the piston temperature in engines, and the piston top temperatures were seen to be much lower than those presented in Figure 3-5. A study of a direct-injection SI engine with a quartz piston, similar to the TCC-III engine, instrumented with piston top and bottom thermocouples showed piston top surface temperatures of around 480 K and piston bottom surface temperatures of 390 K [78]. This engine was operating at similar conditions, 1300 rev/min with an intake pressure of 54 kPa. However, the ΔT across the piston was much smaller.

Another study in an optically-accessible diesel engine using thermographic phosphors deposited on the piston surface to measure temperature [79]. This experiment demonstrated a maximum top surface temperature of around 550 K at -90 °aTDC. Both of these experiments were not able to reach steady state piston surface temperatures due to the limitations of the optical engines. This data suggests that measured piston temperature may not align with the previously noted TCC-III simulations and that measurements of the piston top and bottom surface of the TCC-III engine with the sapphire window are needed to correctly account for the temperature-dependent transmission.

The simulations suggest that a single transmission measurement of the sapphire piston window may be sufficient for one operating condition; however, piston temperature measurements would be needed for all the operating conditions described in Table 6-1 to account for different steady state piston temperatures. Additionally, obtaining measurements of the sapphire piston surface temperature during combustion would require the usage of a laser diagnostic technique, such as thermographic phosphorescent coatings, or the modification of the piston assembly to provide thermocouple access to the piston top [80]. This additional measurement was not performed and therefore the temperature dependence of transmission remains uncorrected.

The data shown herein were corrected for transmission collected at room temperature. The transmission spectra shown in Figure 3-2 and Figure 3-3 were both measured with the optical material at room temperature. Certain results may be impacted by this lack of temperature-dependent transmission data; these impacts will be described, when applicable, in the following chapters. However, all the presented spectral data could be corrected for the temperature-dependent transmission, should the transmission measurements at in-cylinder temperatures be made.

3.2 Hencken Burner

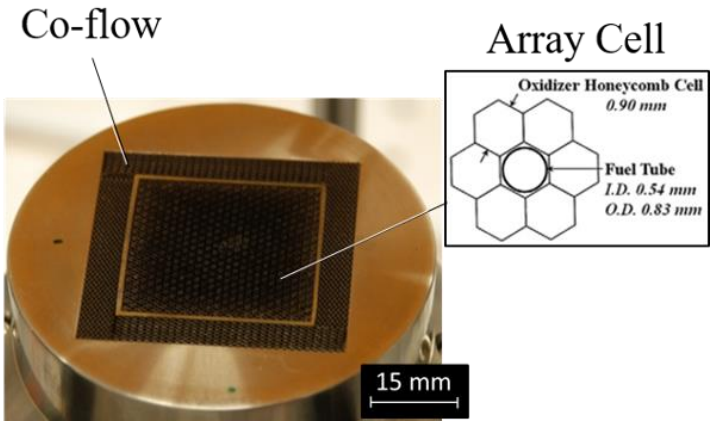

Figure 3-6: Image of Hencken burner flame matrix with a diagram of oxidizer and fuel-tube honeycomb cell adapted from [43]

Flat-flame experiments were performed using a Hencken burner (Technologies for Research, Model RT 1.5 x 1.5) with a square flame area of 25.4 X 25.4 mm. Hencken burners are flat-flame burners that are widely used in the field of combustion diagnostics [81], [82]. The burner consists of a honeycomb array of injection tubes. Separate tubes supplying fuel and air are evenly dispersed across the flame array, and mixing occurs at the exhaust of these injection tubes. Figure 3-6 shows a diagram of the Hencken burner and its honeycomb array.

The benefits of the Hencken burner is that it provides a premixed laminar flame and results in a highly repeatable flame. The flame is anchored adiabatically to the top of the burner surface at a specific lift-off length. The mixture of fuel, oxidizer, and diluent determines the laminar flame speeds [83]. The Hencken burner provides an excellent test case for the spectral emission measurements as the flame radiation was very consistent and the flame conditions were accurately controlled. Through experiments with the burner, it was possible to examine the influence of equivalence ratio and dilution on the measured emission spectra.

In these experiments, the Hencken burner was supplied with methane and air. Nitrogen gas was used as a diluent and as the gas in the co-flow. The nitrogen co-flow surrounds the flame area, as seen in Figure 3-6, protecting from external cross-flows [84]. The mass flow rates of all three gases were computer-controlled by mass flow controllers (Alicat Scientific). The burner had an exhaust system with a slight vacuum to remove the burnt gases from the test room, which was located ~35 cm above the flame area. The burner was operated at standard atmospheric conditions, 98 kPa and 20 °C, and the spectroscopic setup was located ~50 cm from the center of the Hencken burner.

3.2 Spectrometer and Optics

The spectrometer (McPherson Model 2035) had a 350-mm focal length input mirror, and an output mirror with a 400-mm focal length. This combination placed the output spectrum on the camera sensor, which was mounted to the spectrometer's output port. The camera was mounted to the spectrometer via a custom bracket that allowed fine adjustments of the camera alignment and location. All the spectrometer's mirrors were gold-coated to provide the best reflection across the wide range of wavelengths investigated. The spectrometer was equipped with two turret-mounted gratings (Richardson) allowing rapid changes between gratings. The first grating had a peak efficiency at 2.1 μm with a density of 30 grooves/mm allowing for a ~2.4 nm/pixel resolution and a ~4-nm spectral resolution (FWHM at 1959.94 nm). The second grating had a peak efficiency at 4.0 μm with a density of 11.5 grooves/mm allowing for a ~6.3 nm/pixel resolution and a ~10 nm spectral resolution (FWHM at 1958.84 nm). The coarse grating allowed for broadband single-shot measurements spanning ~1000 nm with less spectral detail. The finer ~2.4 nm/pixel grating gave access to finer spectral features with a range of ~460nm. The wavelength location and grating choice were set using the provided McPher software.

A xenon lamp (Newport 6033) was used to determine the spectral resolution of the system. This was done by comparing a xenon transition of known width with the measured width of that transition through the experimental apparatus [85]. This procedure quantified the smallest details distinguishable by the experimental apparatus. In addition, wavelength calibration was performed using the xenon lamp. The known IR transitions of xenon were used to establish a wavelength-to-pixel mapping for each recorded spectrum, and to determine the measurement span [85].

Two CaF_2 plano-convex lenses (focal length = 250 or 500 mm, 50 mm diameter) were used to determine the solid angle that was measured from the combustion device. For experiments on

the flat-flame burner, two 250 mm focal length lenses were used and the focal point was ~10 mm above the center of the burner. For experiments in the optical engine through the fused silica cylinder liner, two 250 mm focal length lenses were used and the focal point was ~10 mm below the center of the cylinder head. For experiments in the optical engine through the sapphire piston window, one 250 mm and one 500 mm focal length lens was used and the focal point was ~15 mm below the centrally located spark plug. The solid angle subtended by the optical setup in the sapphire piston experiments is the subject of further exploration in Chapter 5.

3.3 Infrared Cameras and Triggering

A broadband high-speed IR camera (Xenics Onca MWIR InSb 320, broadband option), hereafter "Onca camera" was used for spectral measurements. The Onca camera has an InSb sensor with 320 x 256 pixels sensitive from 1.0 to 5.5 μm and has monochrome pixels with 14 bits of depth. Each pixel is sensitive to 16384 monochromatic shades or "counts". The InSb sensor is cooled with a Stirling cooler to cryogenic temperatures so that radiation from 1.0 to 5.5 μm can be measured. The camera records at 460 Hz full frame. However, the camera sensor was windowed for spectroscopic measurements. This allowed the experimental setup to only record desired pixels, allowing for significantly higher framerates due to shorter readout time. For spectroscopic experiments, only horizontal information was needed to resolve wavelength; therefore, spectral measurements had the camera windowed to 320 x 8 pixels, allowing frame rates up to 4.5 kHz.

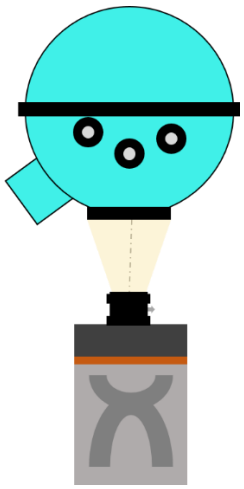

Figure 3-7: Schematic of IR camera and integrating sphere setup used for non-uniformity correction

A two-brightness non-uniformity correction (NUC) was performed using an integrating sphere (Electro Optical Industries ISV-400S). Figure 3-7 shows the experimental setup for the NUC correction. These calibrations removed circular artifacts that appeared on the Onca camera, likely due to the Stirling cooler. The integrating sphere had uniform radiation directly at its exit aperture. The Onca camera manufacturer-supplied software (Xenics Xeneth) allowed NUC through the interpolation of two images, one dark image and one bright image. The dark image was captured with a room temperature integrating sphere with the internal light sources off such that the median pixel value was at < 25% of the maximum pixel count value. The bright image was captured by lighting the integrating sphere thus illuminating the Onca camera sensor such that the median pixel value was at > 50% of the maximum count value. A series of calibrations for different integration times were performed, and the software allowed non-uniformity correction using the provided TrueNUC model. The TrueNUC correction determines an offset correction for a series of integration times with the dark and bright images, identifies and replaces bad pixels, and corrects the gain [86].

The Onca camera contains a cold shield used to protect the InSb sensor and Stirling cooler, but this shield obstructs the edges of the camera sensor when operating without a camera lens. This

is due to a mismatch in f-number between the spectrometer exit port and the Onca camera. This feature partially blocks the signal from 132 columns of pixels. Therefore, signals from those columns were discarded for spectroscopic measurements. This left 188 pixels in the center of the sensor to measure spectroscopic data. However, when capturing IR images the lens attached to the camera matched the f-number allowing images with the full camera sensor.

The Onca camera contains an internal filter wheel allowing for five different filters. Filters were used when imaging with the Onca camera. Filtering allowed for images of specific emission bands. The filter wheel had the following filters: A bandpass filter from 4-5 μm (Spectrogon BBP 4000-5000 nm), a shortpass filter from 2.1 μm (Spectrogon SP 2010 nm), and a bandpass filter from 2-2.5 μm (ThorLabs FB 2250-500-UM). These filters were chosen because they allow the measurement of isolated molecular emissions bands, and the resulting images show the spatial movement of these isolated emissions [69].

High-speed triggering was performed by a LaVision high-speed controller (HSC). This device received triggers from the TCC-III engine CAS system every 0.5 CAD and uses this information to time the camera triggers. This aligned the measurement devices to the timing of the engine. LaVision's DaVis software allowed control of the frame rates and duration of the recording. This device was able to trigger spectral measurements at a two CAD resolution, measuring from -180 to +270 °aTDC.

A second IR camera was used for combined spectroscopy/ imaging studies [29]. The short-wavelength IR camera (Xenics Cheetah-640-CL with the VisNIR option) was used for high frame rate imaging [87]. The Cheetah camera had 640 x 512 monochrome pixels with 12 bits of depth and was sensitive to wavelengths between 0.4 and 1.7 μm (though maximum sensitivity occurs between 1.0 and 1.6 μm). This Cheetah camera was used to provide simultaneous IR images for

experiments on the optical engine. To better match, the spectral range of the Onca camera, a 1000-nm long-pass filter (ThorLabs FELH1000) was inserted between the lens (Navitar SWIR-35) and the camera. The camera can operate at up to 865 Hz in full-frame mode. Unlike the Onca camera, this camera was not windowed. Custom electronics allowed every fourth trigger from the high-speed controller to be sent the imaging camera, producing one IR image for every fourth IR spectrum recorded.

3.4 Experimental Post-Processing

In addition to the transmission correction, two other wavelength-dependent parameters needed correction for the final data. First, the correction for the spectral sensitivity of the experimental setup, which was corrected using a blackbody source. Second, the background emissions due to the heat of the subject being studied. The procedures used to calculate and correct the raw spectral data are described below.

3.4.1 Spectral Sensitivity Measurement

The spectral sensitivity of the spectrometer - Onca camera system was characterized using a blackbody source (Electro Optical Industries LES800-04), and the resulting data was used to correct the measured spectra. Similar to the transmission measurement described in Section 3.2.2, the blackbody source was heated to 800 ºC and an emission spectrum was measured from 1-5.5 μm. The measured emission spectrum was corrected for emissivity.

$$I_{bc,\lambda} = \frac{I_{bu,\lambda}}{\epsilon(T)_\lambda}$$

where $I_{bc,\lambda}$ is the corrected spectral power measurement, $I_{bu,\lambda}$ is the uncorrected spectral power measurement, and ϵ_λ is the manufacturer provided emissivity of the blackbody source at the chosen temperature, T. All of these values are evaluated at a wavelength, λ. This corrected spectral power

was compared to an ideal spectral power for a blackbody at 800°C, $I_{bb,\lambda}$, described by Planck's law [39]. The resulting ratio was used to determine the spectral sensitivity, S_λ, of the Onca camera, IR spectrometer, and optics.

$$S_\lambda = \frac{I_{bc,\lambda}}{I_{bb,\lambda}}$$

S_λ was measured for both the coarse and fine grating. These correction factors were used to correct for all wavelength-dependent effects of grating efficiency, optical transmission, camera-sensor sensitivity, and atmospheric absorption.

3.4.2 Background Emission Correction

Background emission is present in all measurements due to the length of exposure and because the camera is sensitive to mid-wavelength IR where thermal emissions can be measured. The raw data was corrected for the influence of background emission during post-processing.

The data was corrected for background emission through the subtraction of measured background spectra. For the Hencken burner study, background spectra were measured before burner operation. For the TCC-III engine studies, the average of the ten measured spectra, from -150 to -130 °aTDC, for the first measured cycle of the run was used as the background spectrum. This average spectrum captures the heated engine components due to firing but where the in-cylinder pressure is close to the intake pressure. This engine background spectrum accounts for the heated components of the firing TCC-III engine, but is not influenced by the gas radiation because the in-cylinder pressure is close to the intake pressure and the gas temperature is low. Motored TCC-III experiments showed appreciable emission late in the compression stroke due to the heating of fuel and residual product gases. In both cases, the resulting background spectrum, B_λ, was subtracted from the raw measured spectrum, I_λ^{RAW}.

3.4.3 Correction Procedure

Correction of the raw measured data used the transmission, spectral sensitivity, and background emission spectra. These three correction spectra are assumed constant throughout each experiment. The correction occurs at each measured wavelength, and B_λ must be corrected for spectral sensitivity and transmission. For the Hencken burner the raw data is not strongly time-dependent due to the highly repeatable flame. The final Hencken burner emission spectra I_λ, are determined using the following equation.

$$I_\lambda = \frac{I_\lambda^{RAW} - B_\lambda}{S_\lambda * \tau_\lambda}$$

For the TCC-III experiments, the correction procedure must be performed at all measured crank-angle in addition to all measured wavelengths. The raw spectral data, $I_{CA,\lambda}^{RAW}$, is corrected using the following equation [38].

$$I_{CA,\lambda} = \frac{I_{CA,\lambda}^{RAW} - B_\lambda}{S_\lambda * \tau_\lambda}$$

Chapter 4 Radiation of Atmospheric Steady Flame

This chapter presents measurements of the Hencken flat-flame burner from sixteen different flame conditions at atmospheric pressure. The Hencken burner was utilized to develop the experimental apparatus, and the initial measurements of the atmospheric Hencken burner flame were used to validate the accuracy of the measurement. The presented data characterize the product-gas radiation from 1.5-5.5 μm of a methane-air flame for seven equivalence ratios and four levels of nitrogen (N_2) dilution. The measured data is compared to the predicted number densities and temperatures from chemical equilibrium calculations. Finally, the measured stoichiometric spectrum is compared with a simulated spectrum created with the PMC-LBL model, and the initial comparison of measured and simulated IR spectra is discussed.

4.1 Experimental Set-up

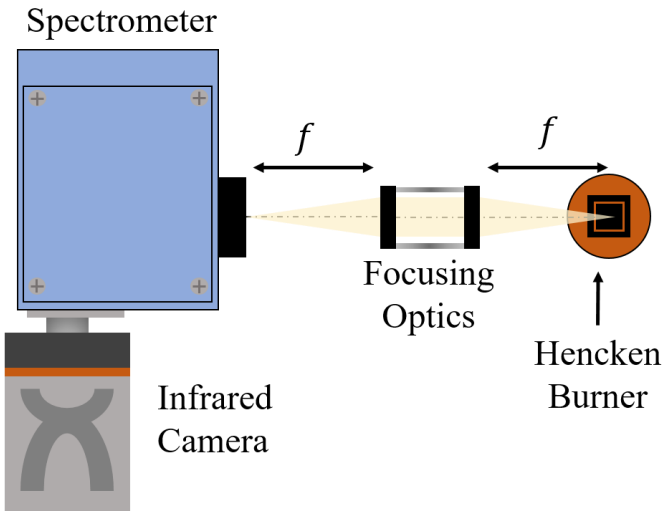

Figure 4-1: Schematic of setup for IR spectral measurement of Hencken burner flame. f1 = f2 =250 mm.

The experiments performed on the flat-flame Hencken burner allowed the effective development of an experimental technique for measuring infrared radiation in combustion. The repeatability of the flat-flame was advantageous in developing the experimental setup used for the optical engine experiments. Additionally, the precise control of the flame's conditions such as equivalence ratio and dilution allowed probing of the influence of different conditions on the emission spectrum. The atmospheric pressure of the flame also provided an excellent benchmark to measure. In engine flows, the high-pressure environment has a significant influence on flame emission and absorption. Figure 4-1 shows the schematic of the complete experimental setup used to capture the IR emission spectrum of the flat-flame burner from 1-5.5 μm. All of the components of this setup are described in Chapter 3.

The fine grating was used to capture 18 spectra, each spanning 270 nm with a 2.4 nm/pixel resolution. Each 270 nm spectrum is the average of one hundred 113-pixel measured spectra. The 18 individual spectra are assembled end to end into one complete spectrum spanning 1.0-5.5 μm

for each condition shown in Table 4-1. The complete measured spectrum is corrected using the equation described in Chapter 3.4.3.

4.2 Hencken Burner Conditions and Flame Conditions

Table 4-1: Conditions measured during Hencken burner experiments. Each X represents a measurement of the full spectrum from 1.5-5.5 μm.

Hencken Burner Conditions								
Equivalence Ratio, (φ)		**0.85**	**0.90**	**0.95**	**1.00**	**1.05**	**1.10**	**1.15**
N_2 Dilution (% of mass)	**0**	**X**	**X**	**X**	**X**	**X**	**X**	**X**
	5	**X**			**X**			**X**
	10	**X**			**X**			**X**
	15	**X**			**X**			**X**

Table 4-1 contains the complete table of the measured operating conditions for the Hencken burner. The burner was operated at a range of lean, stoichiometric and rich equivalence ratios with the addition of dilutions. Thermo-chemical calculations for CH_4-air flames with N_2 dilutions at the tabulated conditions were performed using NASA's chemical equilibrium data with applications software [88]. The resulting temperature and chemical number density values are plotted in Figure 4-2. Dilution was calculated as a percentage of the mass flow rate and was performed using non-reacting nitrogen (N_2) gas. The nitrogen dilution added thermal mass to the combustion reaction, resulting in lower flame temperatures as seen in Figure 4-2. Additionally, nitrogen was chosen as the diluent because it is IR-inactive. The peak temperature occurs in the φ =1.05 case with no dilution. The plots of CO, CO_2, and H_2O number density for the different measured conditions provide useful insight into the trends seen later in the measured spectra.

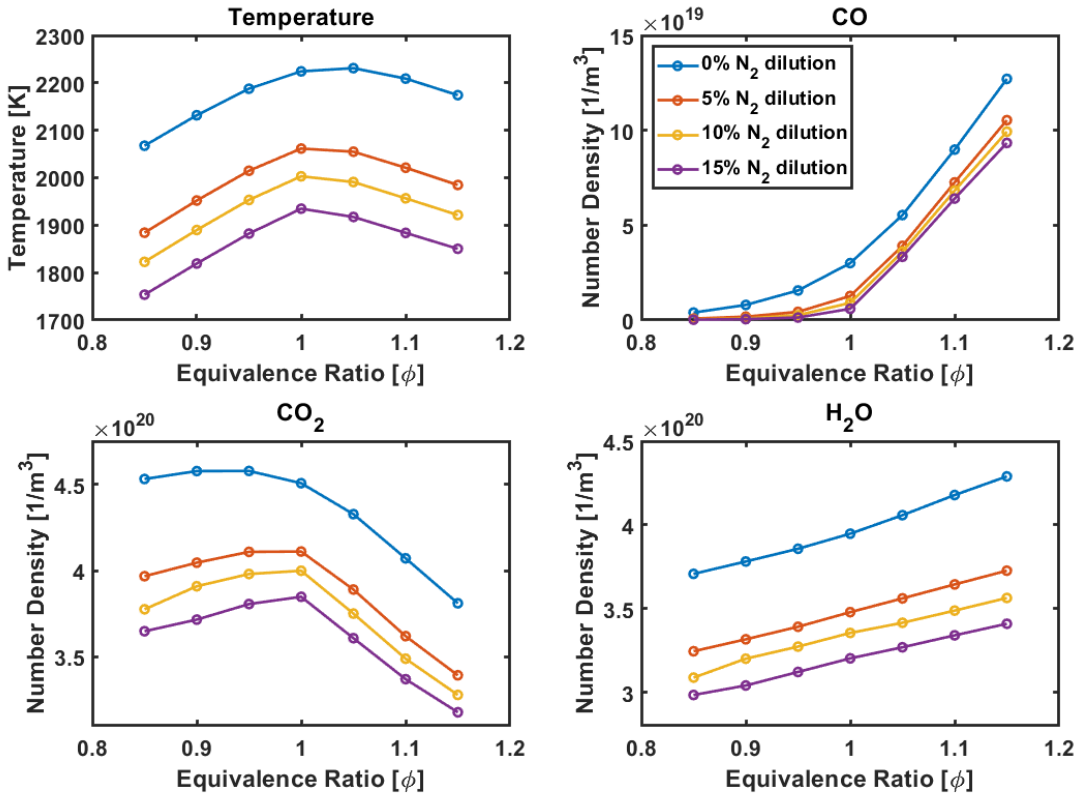

Figure 4-2: Chemical equilibrium calculations of CH_4-air flame for ϕ=0.85-1.15 and N_2 dilution=0-15 %wt

Concurrent simulations of a similar flat-flame burner operating at stoichiometric conditions were performed by Dr. Sebastian Ferreyro Fernandez at Pennsylvania State University allowing comparison of the stoichiometric spectrum [89]. The rectangular computational domain has sides that are 36.5 mm and a height of 50 mm. The results were post-processed using the photon Monte Carlo line-by-line method (PMC-LBL) [14] to determine the IR emission spectrum of H_2O, CO_2, and CO reaching the sides of the domain. Dr. Fernandez describes a similar laminar flame simulation and radiative post-processing method in his dissertation [89]. Additional personal communication provided the species-specific radiative emissions and the major species and temperature in the flame data shown in. The experimental focal point was located 10 mm above the center of the burner, which is above the reaction zone seen in Figure 4-3. Therefore, it is clear that the experiments capture the product gas radiation due primarily to H_2O and CO_2.

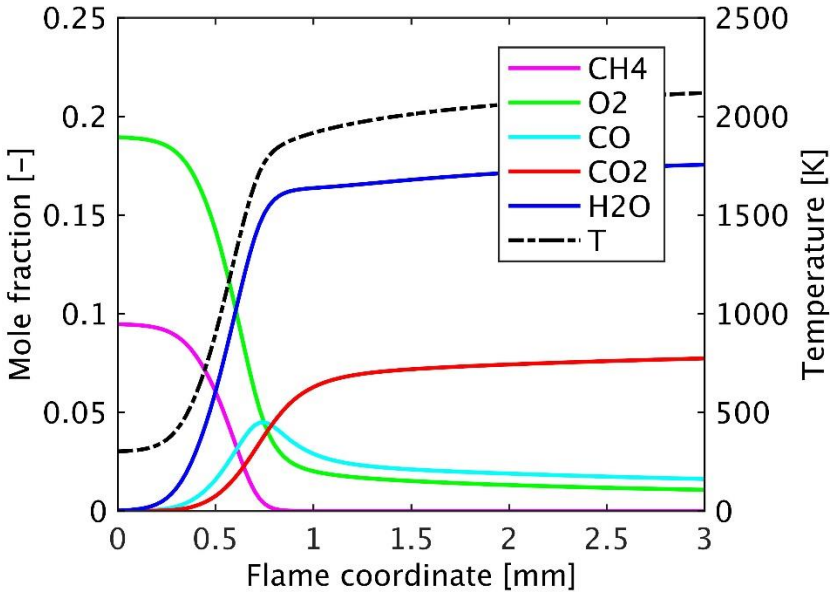

Figure 4-3: Major species and temperature profiles along the flame coordinate for a CH4-air laminar flame [Provided by Dr. Daniel Haworth and Dr. Sebastian Ferreyro Fernandez at Pennsylvania State University].

Species-specific spectral data is shown in Figure 4-4. This shows the major bands of importance in this wavelength range. Namely, the H_2O and CO_2 combination band from ~2.5-3.5 µm and the CO_2 band from ~4-5 µm. The CO contributions are seen to be nearly negligible in simulations, but measured CO emissions are noticeable.

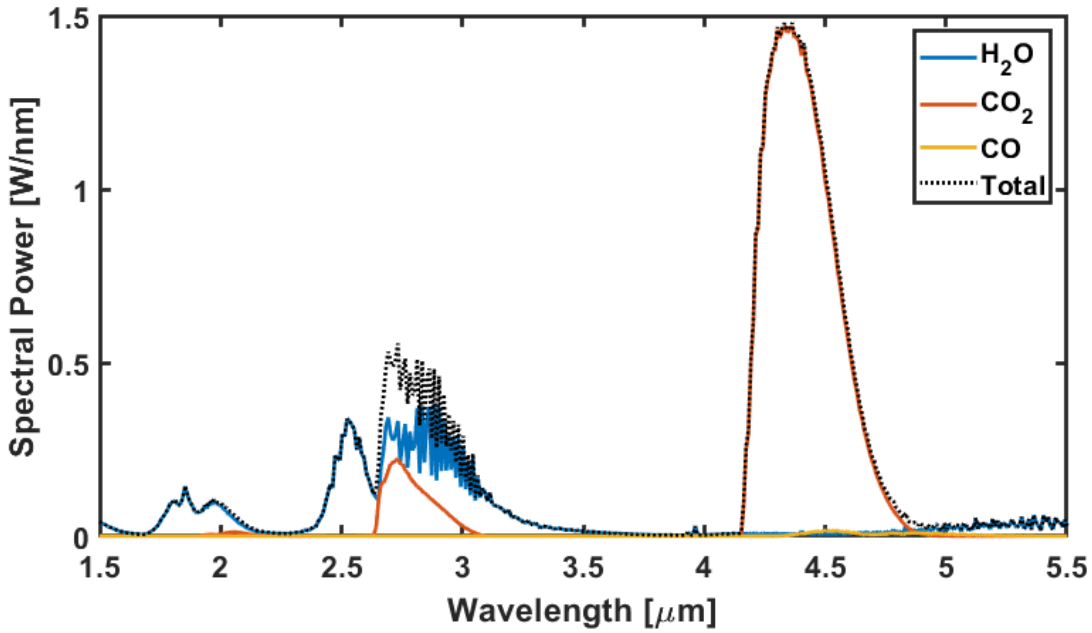

Figure 4-4: Simulated stoichiometric Hencken burner flat flame with species-specific contributions labeled [Provided by Dr. Daniel Haworth at Pennsylvania State University].

4.2 Hencken Burner Results

4.2.1 Hencken Burner Flat-flame Infrared Images

IR images were taken with the Onca camera of the flat-flame at different equivalence ratios and are shown in Figure 4-5. These images are the 100-image average of the flame using different bandpass filters described in Chapter 3.4 and show the average spatial characteristics of the Hencken burner flame for different equivalence ratios. The images are shown from lean (φ=0.85) on the top row to rich (φ=1.15) on the bottom row. The measured wavelength range of the filters is labeled at the top of each column, and the corresponding wavelength regions are highlighted in the stoichiometric spectrum shown in Figure 4-6. The leftmost column of Figure 4-5 shows images of the emission of the $\nu_2 + \nu_3$ ro-vibrational band of H_2O in the flames. The second column from the left contains the weak emission from 2-2.5 μm. This region contains the edge of two H_2O vibrational bands, $\nu_2 + \nu_3$ and ν_3. However, this spectral region is mostly free of molecular

radiative signal. The signal in this column was multiplied by 35 to identify distinct features. The main signal comes from the heated burner surface, and in the lean image the elevated central injection tube can be seen. The next column, covering 4-5 μm, shows images of the ν_3 ro-vibrational band of CO_2. It is clear from the images in Figure 4-5 and the spectra in Figure 4-6 that the majority of the IR emission measured during these experiments. The rightmost column shows images without a filter, capturing all the emission from 1-5.5 μm.

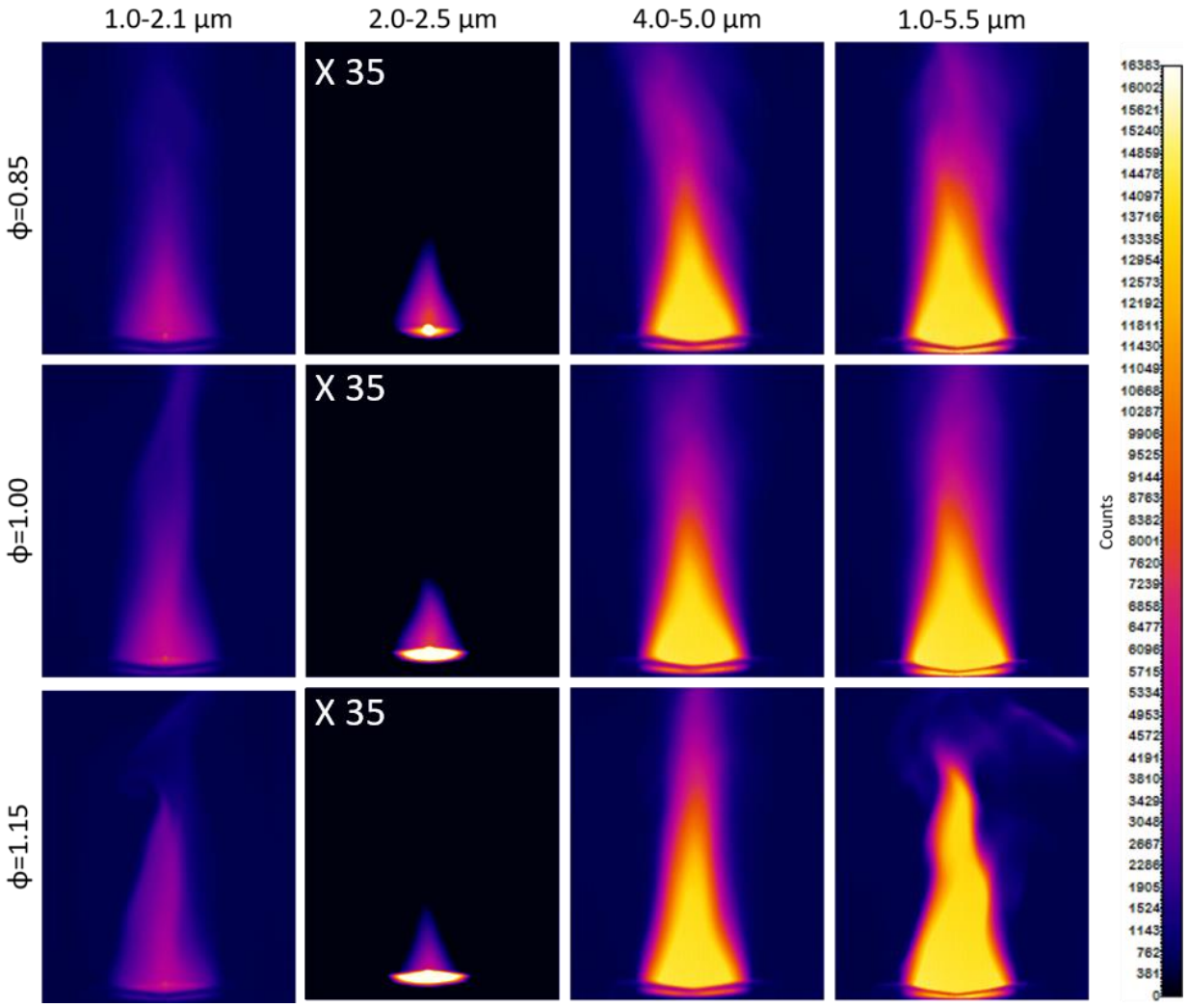

Figure 4-5: Filtered images of flat flame for various stoichiometric ratios.

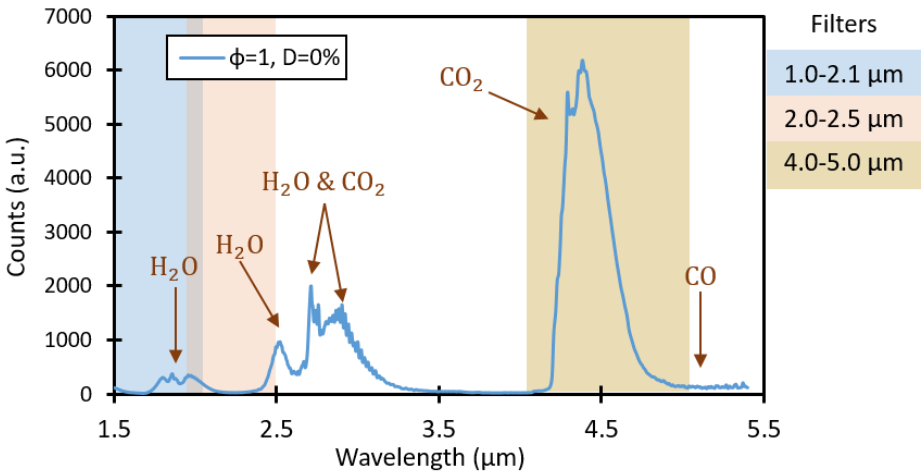

Figure 4-6: IR spectrum of stoichiometric methane-air flame. Molecular ro-vibrational bands are labeled and imaging filters are highlighted.

From these images, it is clear that different burner conditions lead to different flame shapes. The rich flame case has a longer flame due to the additional time needed to burn all the fuel and the later formation of CO_2. There is unburned fuel that is not burned at flat-flame and that burns upstream above the flat-flame after additional air has been entrained. This explains the longer region of CO_2 emission on the rich case seen in images and similarly explains why the lean case has a shorter region of CO_2 emission.

4.2.2 Hencken Burner Spectroscopic Measurements

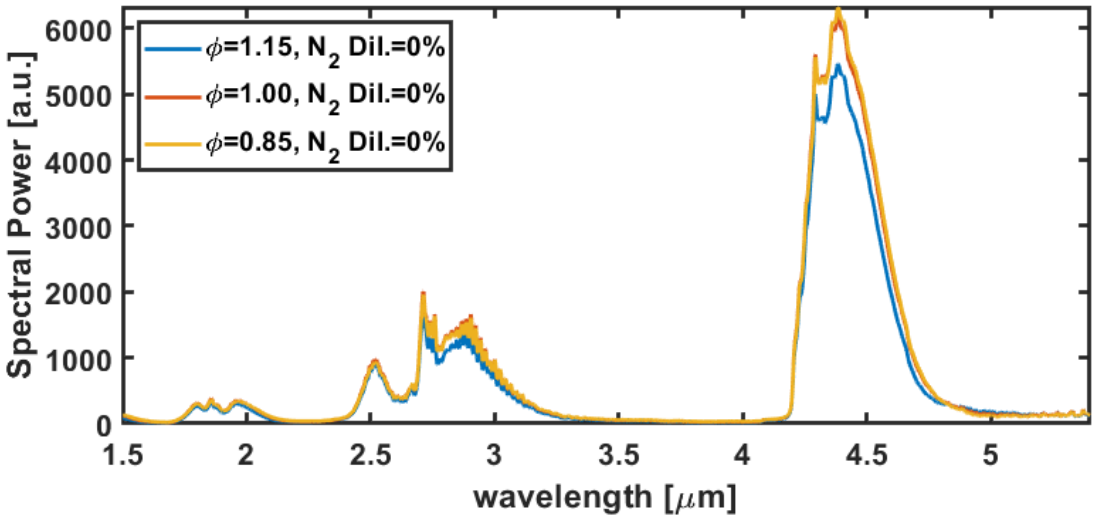

Figure 4-7: IR Spectra from 1.5-5.5 µm of flat-flame for various stoichiometric ratios and no dilution (D=0%).

Figure 4-7 shows the spectra associated with the flat-flame burner conditions shown in Figure 4-5. These spectra are labeled by their equivalence ratio (φ) and their nitrogen dilution as a percent of mass (N_2 Dil.). The difference between the rich (φ =1.15) case and the other equivalence ratios without dilution is clear. There is significantly less radiation from CO_2, 4-5 µm, in the rich case. Rich flames are a lower temperature cooler and have a lower concentration of CO_2, but a higher concentration of CO and H_2O. The effect of increased CO concentration is further explored in Figure 4-10. Interestingly, the IR emission spectrum of the lean, φ =0.85, and stoichiometric flames have similar net radiation. This could be due to the height of the measurement from the flame location, causing the measured temperature to be similar for the lean and stoichiometric flame.

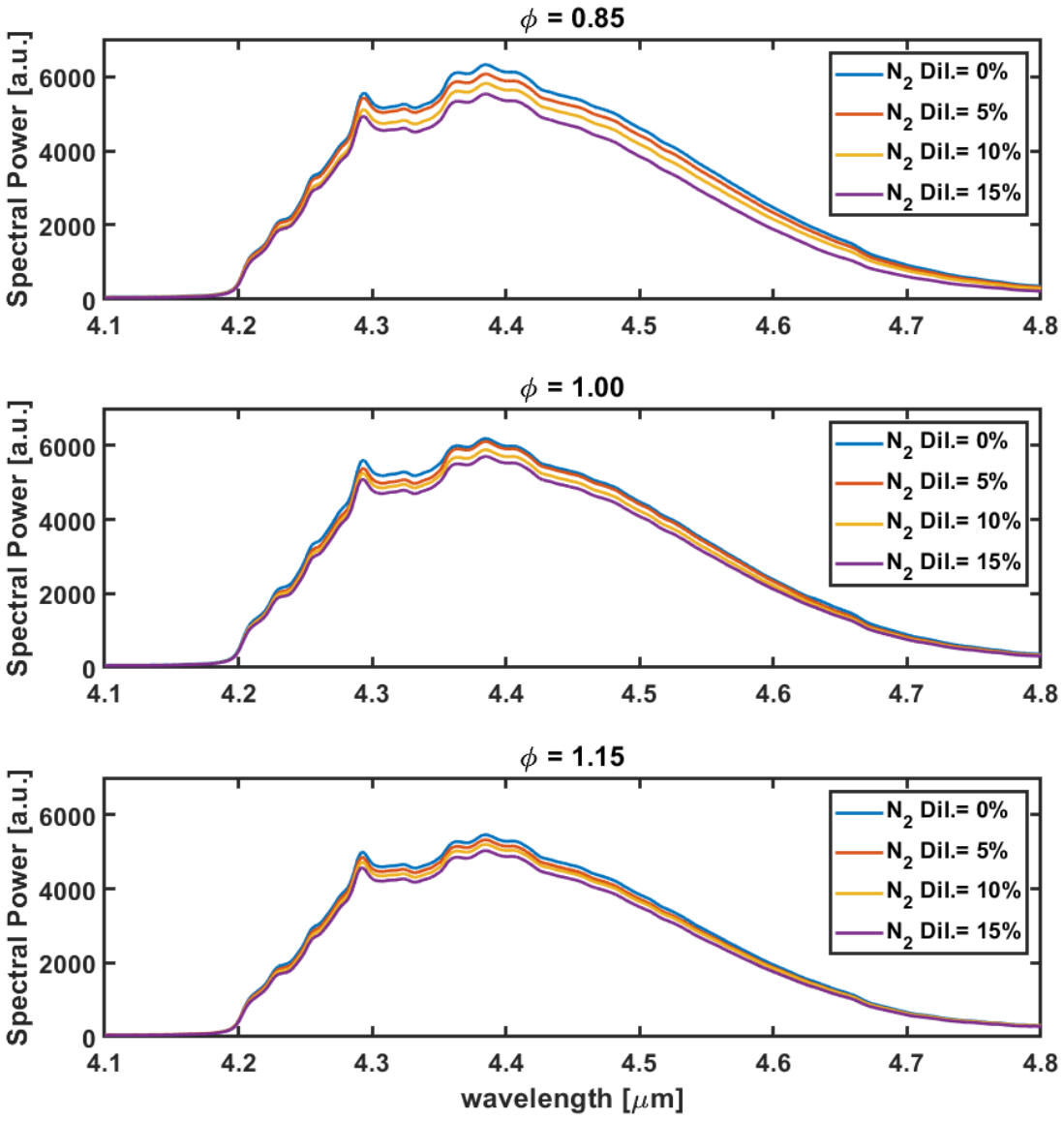

Figure 4-8: Effect of dilution on spectral emission is related to change in temperature.

The effect of N_2 dilution is explored in Figure 4-8 for the CO_2 feature seen from 4.2-4.8 µm. Chemical equilibrium calculations were used to determine the change in temperature due to N_2 dilutions. For the lean case shown in Figure 4-8, the flame temperature drops from 2067 K to 1753 K from a 15% increase in N2 dilutions. This ~300 K change in temperature causes a monotonic decrease in emission across the entire measured IR spectrum. The same trend is seen

for the φ =1.00 and φ =1.15 cases. The noted impact of nitrogen dilution guides the understanding of the results for diluted engine charges in further chapters.

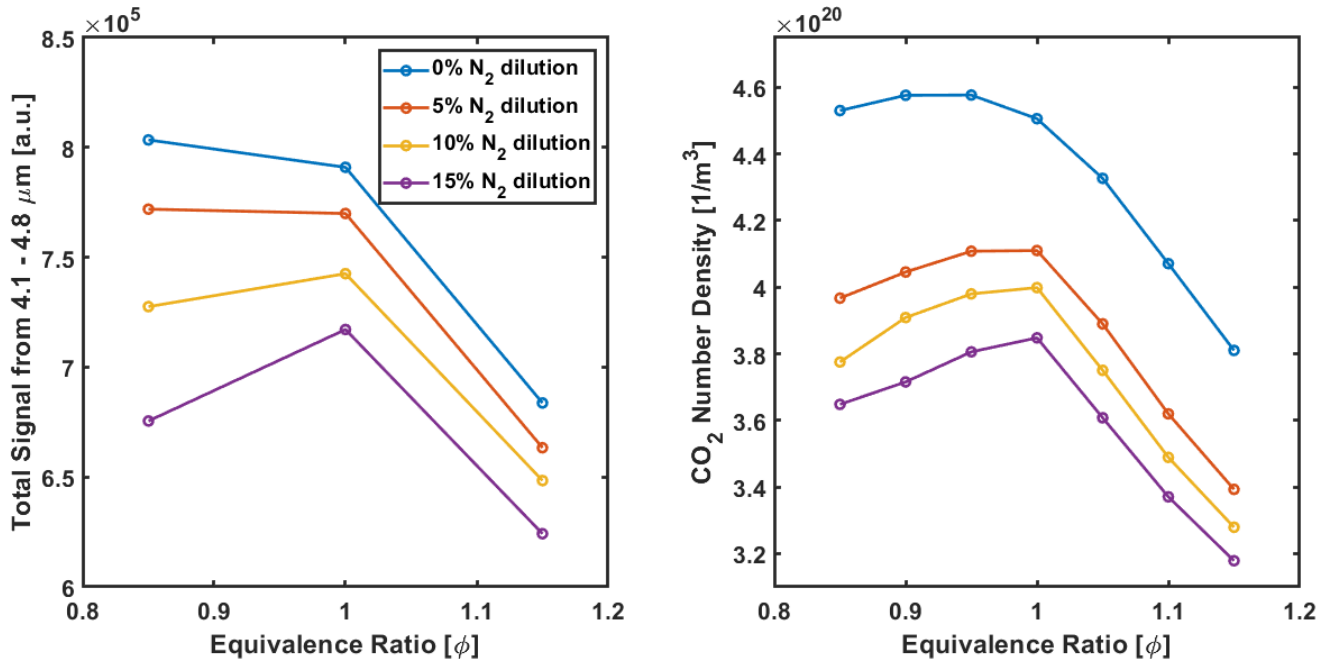

Figure 4-9: Left: Total signal from 4.1-4.8 μm at different levels of dilution and equivalence ratios. Right: CO_2 number density against equivalence ratio. Measured IR intensities resemble the trends in CO_2 number density for various equivalence ratios.

Figure 4-9 shows the total measured signal from 4.1-4.8 μm and the CO_2 number density side-by-side to further explore the effect of dilution. There is strong agreement in trends between the 12 measured conditions and the expected number density at that condition. This shows the strong agreement between the measurements and theoretical calculations. The influence of temperature, pressure, and self-absorption cause changes in the total measured signal. These influences are not captured in the molecular number densities, and cause the differences between the plots. The agreement of the CO number density and the measured signal is explored in the following section.

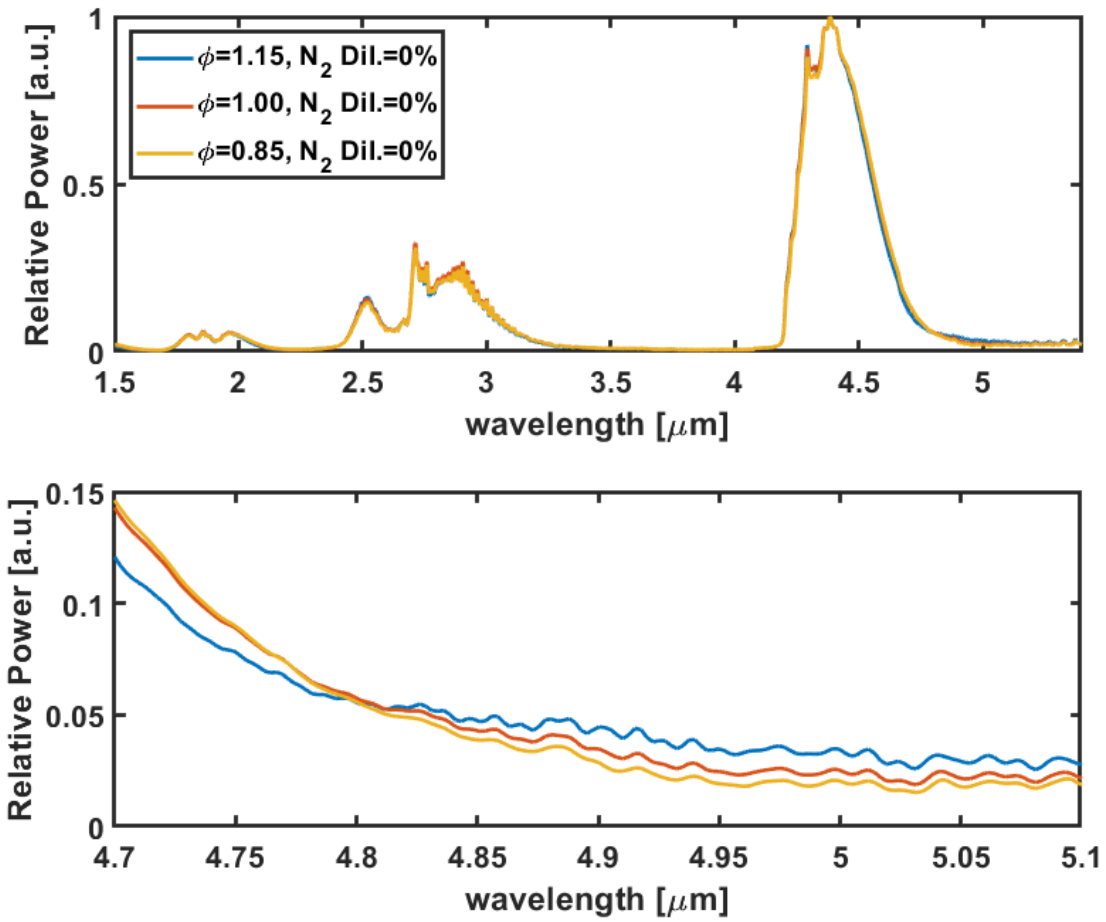

Figure 4-10: Top, normalized IR spectra for 3 equivalence ratios. Bottom, CO emission is higher for rich cases.

To monitor changes in the species contributions, the measured spectrum is normalized by the peak emission value. This allows the different ro-vibrational bands' relative radiative power contributions to be seen. Figure 4-10 is a plot of the three IR spectra seen in Figure 4-7 normalized by the peak emission that occurs at ~4.4 μm in the large CO_2 feature. The top plot shows that the spectra agree much closer qualitatively when normalized, but examining the spectra around 4.9 μm in the bottom plot shows an interesting trend. CO is a diatomic molecule and has its fundamental ro-vibrational band centered at 4.66 μm and its longer-wavelength P-band from 4.66-5.1 μm, as previously seen in Figure 2-4. The rich operation of the flat-flame results in a higher number density of CO explaining the increasing emission around 4.9 μm from increasing φ. A

similar trend is expected in the CO R-band, between 4.3-4.66 µm, but this band is eclipsed by the large CO_2 υ_3 feature.

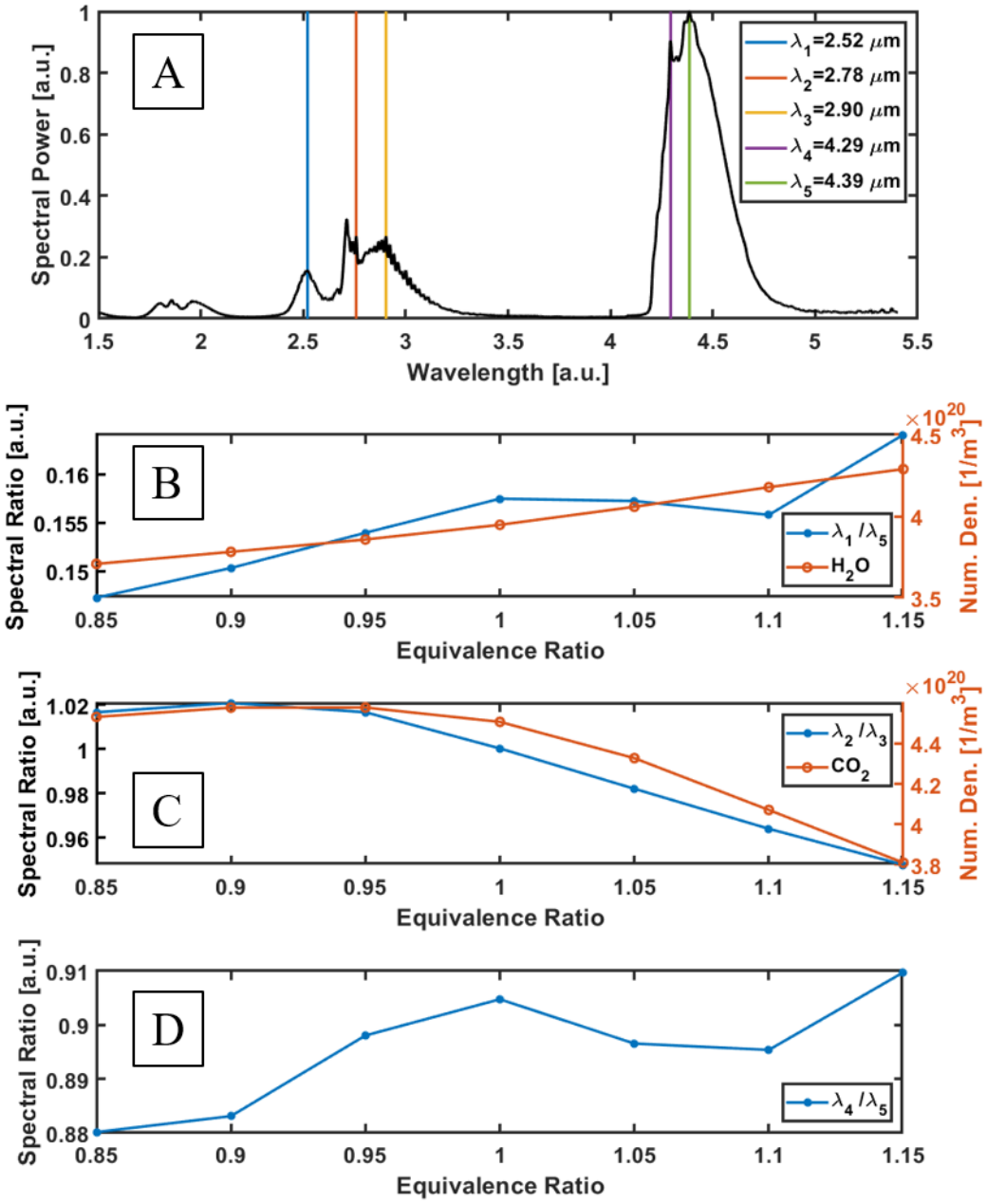

Figure 4-11: A, annotated stoichiometric spectrum with wavelengths of interest shown. B-C-D, plots of different ratios of spectral features. Plots B and C show the number density of a species that follows the spectral ratio trends.

Figure 4-11 shows the spectral feature ratios and their relevance to the flame conditions. Plot A of Figure 4-11 shows the IR spectrum of a stoichiometric Hencken burner flame with five

wavelengths chosen. These wavelengths, λ_1- λ_5, isolate different spectral features. The chosen wavelengths and corresponding molecular vibrations are described in Table 4-2. These wavelengths were chosen based on the previous exploration of signal ratios in combustion gases [59], and because they allow the exploration of ratios of species-specific emissions. λ_5 was chosen because it is the wavelength that had the maximum spectral power for all measured conditions.

Table 4-2: Chosen wavelength, corresponding molecules, and molecular vibration for the chosen wavelengths explored in Figure 4-10

Name	Wavelength [μm]	Molecules	H_2O Vibration	CO_2 Vibration
λ_1	2.52	H_2O	υ_3	-
λ_2	2.78	H_2O and CO_2	υ_1, υ_3	$2\upsilon_2+\upsilon_3, \upsilon_1+\upsilon_3$
λ_3	2.90	H_2O and CO_2	υ_1, υ_3	$2\upsilon_2+\upsilon_3, \upsilon_1+\upsilon_3$
λ_4	4.29	CO_2	-	υ_3
λ_5	4.39	CO_2	-	υ_3

Figure 4-11 B shows the λ_1 / λ_5 ratio, which corresponds to a pure H_2O emission and a pure CO_2 emission, trending upwards as φ increases. This suggests higher H_2O emission and lower CO_2 emission for richer cases, and follows the chemical concentrations seen in Figure 4-2. As noted in Figure 4-8, temperature increases strongly affect the 4-5 μm region, and therefore the non-monotonic λ_1 / λ_5 ratio is due to a convolution of the molecular number densities and temperature effects.

Figure 4-11 C shows the λ_2 / λ_3 ratio, which demonstrates the decreasing magnitude of CO_2 emission in the 2.5-3.5 um region with increasing φ. Both λ_2 and λ_3 have emissions from H_2O and CO_2, but the CO_2 emission is weaker at λ_3, as seen in Figure 4-4. The influence of the changing

equivalence ratios can be seen on the combined H_2O/CO_2 feature. CO_2 number density and λ_2 emission decreases with increasing equivalence ratio, and H_2O number density and λ_3 emission increases with increasing equivalence ratio. Therefore, this spectral ratio is primarily influenced by the CO_2 and H_2O number densities and can be seen to agree qualitatively with the CO_2 number density.

Figure 4-11 D shows the λ_4 / λ_5 ratio looks at the self-absorption of the major υ_3 CO_2 feature. This ratio is purely comprised of CO_2. The increasing temperature enhances the radiative emissions but also the radiative absorption. However, there is an overall increasing trend with higher φ. The shape of the 4-5 um feature due to CO_2 changes according to the flame conditions. This change is due to the influence of radiative absorption. Radiative absorption, especially of the 4-5 um feature, is explored further in engine measurements as it can consequentially change the local conditions within the engine.

4.2.3 Measured and Simulated Hencken Burner Spectrum Comparison

Ongoing computational interest into modeling radiative emissions and absorption within a combustion setting includes an interest in atmospheric pressure flames such as the Hencken burner [89]. A dataset of experimental flat-flame burner spectra at a series of operations has been produced, and this experimental data can be used to validate radiative simulations. Initial validation of simulations of molecular radiation in a Hencken burner flame at stoichiometric conditions is shown below. The significance of molecular re-absorption is not measured experimentally, but the experiments provide information about the net molecular radiation reaching the experimental apparatus. Dr. Daniel Haworth and Dr. Sebastian Ferreyro Fernandez at Pennsylvania State University provided initial simulations of the flat-flame operated stoichiometrically on a methane/air mixture for comparison [89]. The computational domain was

kept at ambient pressures and an initial temperature of 300 K. The major species and temperature of the simulated flame are shown in Figure 4-3. The spectral post-processing used an instantaneous snapshot of the computed three-dimensional fields of pressure, temperature, and radiative participating media from the flat-flame burner at steady-state conditions to simulate the CO_2 and H_2O radiation using the PMC-LBL method.

These simulations were compared to the measured data, and the simulated spectra were refined by adjusting the concentrations of active IR species. The emission measurements performed herein have no known radiative unit and are a measure of the relative intensity of light in arbitrary units (a.u.). As seen in the previous sections of Chapter 4, this relative information is used to gain an understanding of the relative spectral characteristics. However, the measurements must be scaled when used to validate the PMC-LBL simulations. Theoretically, the measured and simulated spectra are correlated by a wavelength-independent constant, C, such that:

$$I_{\lambda,Sim} = C * I_{\lambda_{,Exp}} \quad [\frac{W}{nm}]$$

If the simulated and measured spectra agree then C can be determined at any wavelength. However, in practice there are disagreements between the measurements and simulations; therefore, C must be determined numerically. In Figure 4-12, C is determined such that the peak net emission is equal between the simulated and scaled measurement. The resulting simulation data, presented alongside a scaled measured spectrum, is seen in Figure 4-12.

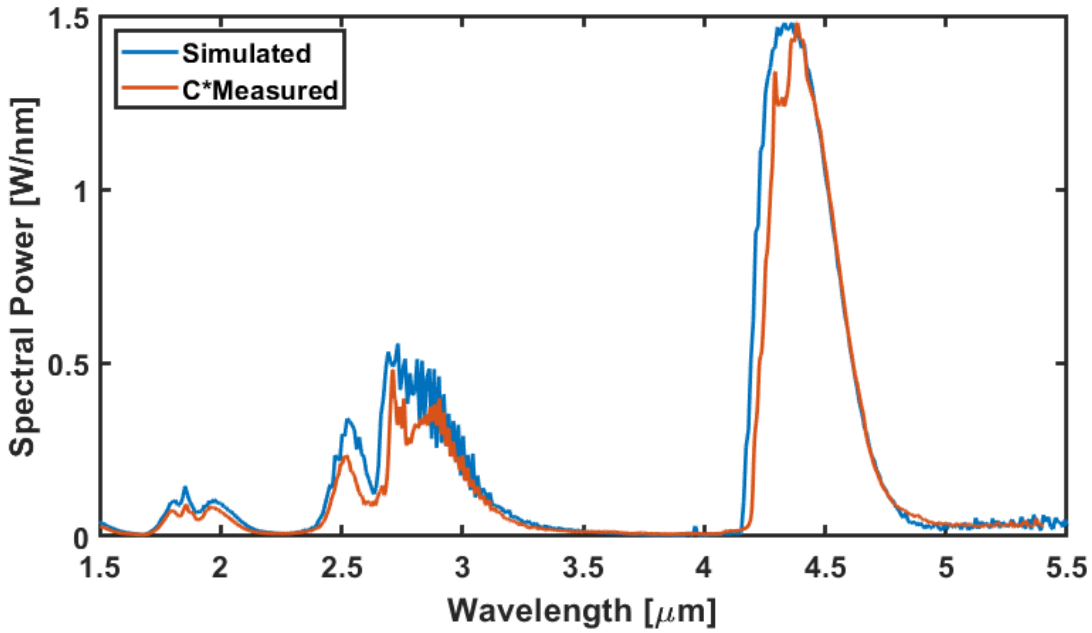

Figure 4-12: Experimentally measured and simulated IR spectrum of stoichiometric flat-flame show good agreement. Simulations provided by Dr. Daniel Haworth and Dr. Sebastion Ferreyro Fernandez from Pennsylvania State University.

From Figure 4-12 it is clear that major ro-vibrational bands are in close qualitative agreement. The disagreement exists in the CO_2 feature around 4.3 µm and may be partially due to uncorrected influences of atmospheric absorption of CO_2 radiation in measurements and CO_2 self-absorption in the simulations. The simulations provide quantitative estimates of the emission and absorption of such a flame. The measured radiation at 4.9 µm due to CO radiation is higher than in the presented simulations and suggests that the CO radiation is being under-predicted. The overall agreement is encouraging, but additional simulations of the flat-flame at the different operating conditions would provide stronger validation of the PMC-LBL method for atmospheric pressure flames. Additionally, an improved agreement is possible if the solid angle subtended by the experimental apparatus was considered in the simulations; however, given the steady and repeatable flat-flame it is likely that the measured volume radiation would be in strong agreement with the total radiative emissions from the burner.

This series of experiments provide much more repeatable and steady results than those expected in the engine, and therefore provides a good test case for comparison between the measurements and simulations. The addition of the high-pressure transient combustion environment and cycle-to-cycle variability make the experimental and simulated data in-engine much more complicated to obtain and compare. The high-pressure environment drastically increases re-absorption and leads to the 2.5-3.5 μm feature outweighing the 4-5 μm feature. Nevertheless, the simulations must be validated with accurate experimental measurements to achieve reliable and realistic results.

4.3 Summary

This Chapter discussed an initial experimental study of molecular radiation for an atmospheric flat-flame burner. The Hencken burner flame operated at atmospheric pressure was used to develop the measurement technique. The measured flat flame spectra exhibit changes due to flame conditions. The increasing equivalence ratio showed decreasing spectral power; nitrogen dilution decreased the flame temperature and lowered the overall spectral power; and the species-specific contributions of H_2O, and CO_2, CO were isolated through spectral ratios.

The atmospheric pressure, stoichiometric flat-flame emissions were used for the validation of a model of molecular radiation. Qualitative agreement exists between the measurements and simulations. There remain differences in the spectra that can be attributed to the experimental apparatus and the simulation technique. However, further comparison of the flat-flame burner measurements and simulations at different conditions will reveal the accuracy of the PMC-LBL method for atmospheric conditions. Once simulations of various Hencken flame conditions are performed, a comparison with measurements can be made.

Finally, these measurements provide insight into the expected spectra in the TCC-III engine. The various conditions measured and presented in the following chapters evaluate the changing spectral characteristics for a variety of equivalence ratios and dilutions (N_2 and CO_2). However, the trends seen in the steady flat-flame burner provide insight into spectral characteristics change due to species concentrations and temperature. The dynamic nature of engine flames adds a level of complexity, but the overall trends can be associated with similar behavior seen in this chapter.

Chapter 5 Measured and Simulated Molecular Radiation

This chapter presents a combination of measured and simulated radiative spectra aimed to validate the PMC-LBL model in the temporal and spectral dimensions. All presented spectral simulations were performed at the Pennsylvania State University in Dr. Daniel Haworth's laboratory. An initial study compared the experimental and simulated radiative spectral emissions of the TCC-III optical SI engine from 1.4-2.7 μm, but the measured and simulated net spectra reaching the walls of the TCC-III engine had significant disagreement [38]. This was largely due to a discrepancy in the signal collection volumes between the experiments and simulations. The experiments measured emissions from a long narrow volume subtended by the collection optics while the simulation results included the total in-cylinder radiation. Therefore, it was necessary to account for these sampling differences. The presented study resolves these issues by applying a measured instrument weighting function to the simulated spectra and then compares net spectral emission from 2.4-5.2 μm. This work was accepted for presentation in the 14th International AVL Symposium on Propulsion Diagnostics and will be published in the proceedings [90].

5.1 Experimental Setup and Procedure

5.1.1 Crank Angle Resolved Infrared Spectroscopy Setup

Both the measurements and simulations were performed on the TCC-III engine [70]. A central spark plug ignited a stoichiometric mixture of propane/air heated to 40 °C. The fuel and air are homogeneously mixed in the intake plenum. The engine was operated at 1300 rev/min,

matching previous experimental and computational studies [91]. The ignition timing was -18° after top dead center compression (^{o}aTDC): which results in an average crank-angle of percentage of 50% mass fuel burned (CA50) at 9.5 ^{o}aTDC. The intake pressure was 40 kPa and the exhaust pressure was 101.5 kPa. The TCC-III engine is characterized by high variability between cycles making it ideal for the study of cycle-to-cycle variations (CCV) [92]. The average peak pressure for all the recorded runs was 1837 kPa with a relative variation between runs of 1.8%. The variation of indicated mean effective pressure (IMEP) between separate measured runs was up to 2.4%. An online collection of information about the TCC-III engine and GT-Power models are available for download on the deep blue database at: https://deepblue.lib.umich.edu/handle/2027.42/108382 [17].

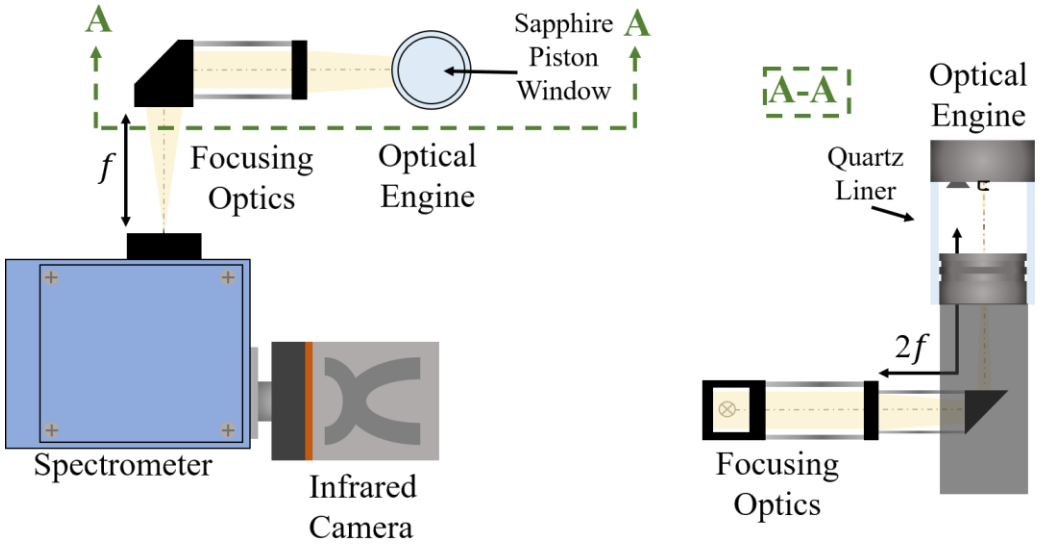

Figure 5-1: Schematic of the experimental setup for measuring radiative emission through Bowditch piston.

Optical access was provided through a sapphire piston window, which is accessed through the extended Bowditch piston. The sapphire piston window offers excellent uniform transmission in the visible through near-infrared bands, but its transmission begins to degrade after 4 μm, as

seen previously in Figure 3-3. The transmission spectrum of the sapphire piston window was measured and corrected for all presented data using the procedure described in Chapter 3.

A grating spectrometer (McPherson Model 2035) was used to disperse the IR radiation from the engine, as diagrammed in Figure 5-1. The experimental data shown in the results section was captured using a grating that was blazed at 4.0 µm with a density of 11.5 grooves/mm. Focusing optics (two CaF_2 plano-convex lenses with focal lengths of 250 and 500 mm and diameters of 50 mm) guided the radiation emitted from a volume at the center of the combustion chamber onto the entrance slit of the spectrometer. The setup produced spectra with ~11 nm spectral resolution (FWHM at 1959.94 nm) and a span of 1000 nm. Table 5-1 describes the measured wavelengths and the relevant molecules within the wavelength region. The two measured wavelengths regions, 2.45-3.45 µm and 4.0-5.0 µm were chosen as they contain the two strongest spectral features of CO_2 and H_2O [51]. Additionally, these two spectral features were the focus of a simplified radiative model [35]. Each wavelength range was measured for 100 continuous cycles to allow for adequate measurement of spectral CCV. The high-speed measurements yielded spectra at a 2-CAD resolution recording from -180 to 270 °aTDC providing 226 measured spectra per cycle. Additional information about the infrared camera, image acquisition, and processing is available in [38].

Table 5-1: Wavelength ranges and corresponding molecules of the measurements

Experiment Title	Measured Wavelengths	Relevant Molecules
$\boldsymbol{\lambda_1}$	$2.45 - 3.45\ \mu m$	H_2O, CO_2
$\boldsymbol{\lambda_2}$	$4.0 - 5.0\ \mu m$	CO_2

The spectral measurements performed in the TCC-III engine are not associated with an absolute unit. In an absorption measurement, initial known radiation is used to probe the sample of interest [40], but the emission measurements performed herein have no known radiative unit. The experiments measure the relative intensity of light in arbitrary units (a.u.). The absolute intensity values are not critical in these experiments because the focus is on assessing relative spectral intensities for comparison with simulated spectra. However, absolute units of radiation could be determined with the use of a calibrated radiation source. The experimental apparatus and conditions remain consistent throughout all experiments, so all measurements are an accurate measure of relative radiation.

In this study, the measurements are used to validate the PMC-LBL simulations. Theoretically, the measured and simulated spectra are correlated by a constant, C, such that:

$$I_{\lambda,Sim} = C * I_{\lambda_{,Exp}} \quad [\frac{W}{nm}]$$

If the simulated and measured spectra agree then C can be found at any comparison crank-angle degree. C should be a single value that is valid for all measured wavelengths and crank-angles. However, in practice there are disagreements between the measurements and simulations. Disagreement may originate from the comparison of different pressures, temperatures, and species concentrations of the mixtures, which affect the resulting spectra. Further disagreement, particularly in the λ_2 region, exists due to the temperature-dependent transmission of sapphire. Therefore, C must be determined numerically by minimizing $\left\| I_{\lambda,Sim} - C * I_{\lambda,Exp} \right\|$. A function reduced the overall differences to find the best C value, and the resulting spectra show the remaining differences between the measurements and the simulations.

5.1.2 Engine Operating Conditions

The validation study was performed with three different pressure conditions: low, average, and high in-cylinder pressure. Three representative simulated cycles were identified, and measured cycles with similar peak pressures were extracted from the λ_1 and λ_2 datasets. Figure 5-2 shows the pressure traces of the selected cycles. This figure shows that the simulated maximum pressure is reached several crank-angle degrees before the measured pressure. This is primarily due to the models for ignition and flame propagation which result in higher pressures and faster burns. However, the selected cycles demonstrate agreement early and late in the cycle, and the overall pressure trends still represent different engine behaviors. Four crank angle degree locations: -8, +8, +16, +150 ^{o}aTDC, were used for validation. The crank-angle locations capture the flame growth, peak radiation, and flame extinction. Pressure differences between the representative cycles at +16 ^{o}aTDC affect the comparison of spectra, but +16 ^{o}aTDC is close to where peak pressure and peak radiation are expected for both the experiments and simulations. Future

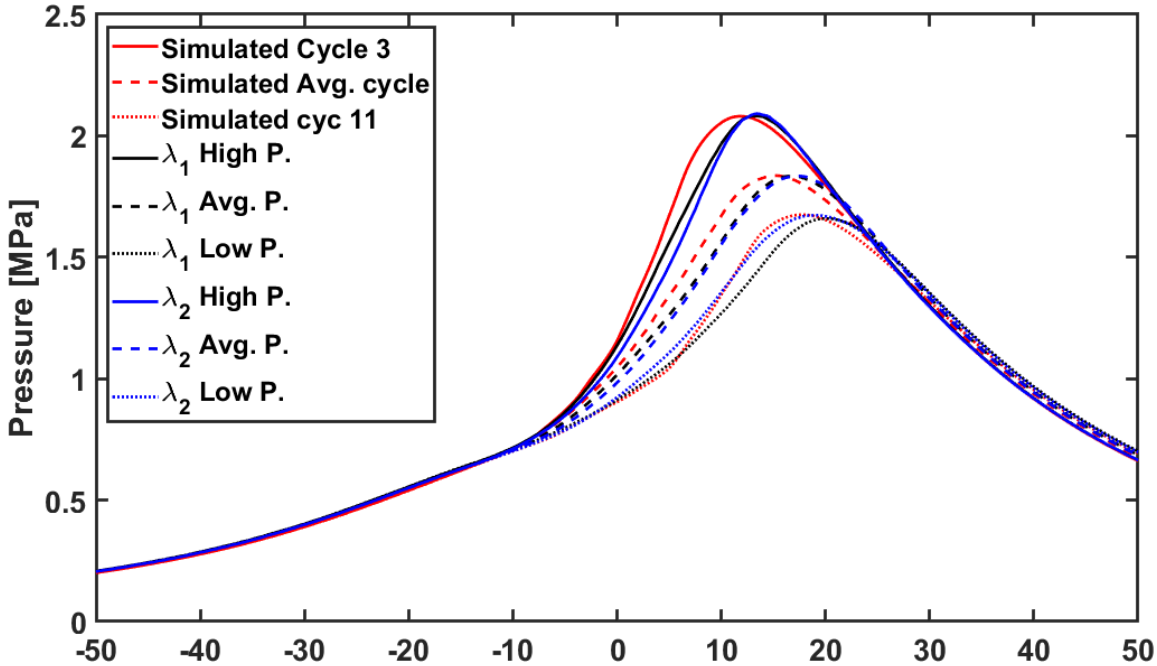

Figure 5-2: Pressure traces of measurements and simulations for the high, average, and low-pressure cases

improvements to the simulations could more accurately duplicate the measured pressure behavior by addressing the ignition model, turbulent flame propagation, and wall heat transfer.

5.1.3 Optical Weighting Function Measurements

This measurement technique is passive, all of the radiative emissions within the solid angle accessible from the collection optics were measured. Throughout this document, the optical volume where radiation was sampled is referred to as the "measurement volume". The signal strength varies as a function of location within the measurement volume. A methodology was developed to measure an optical weighting function that describes the signal throughout the measurement volume. The pathlength of the emission measurement changes throughout the cycle as the piston moves; however, distortion due to the moving piston window was negligible in measurements. Therefore, the weighting function describing the measurement volume was assumed constant throughout the cycle.

To measure this optical weighting function, an optical stage with the ability to move in the X-Y-Z directions was mounted with a xenon lamp. The xenon pin lamp (Newport 6033) was placed in an aperture shield with an aperture size of 2.35 mm. Xenon has infrared-active transitions that are captured by the camera-spectrometer setup [85]. The experiments were performed by making spectral measurements with the xenon lamp moving across a 1 x 1 cm^2 area located at the center of the piston window in $\Delta x=\Delta y=0.625$ mm steps at 16 different Z locations. The peak signal location was found at the 16 Z locations and a 1-cm sweep centered at the peak location was measured in the X and Y direction. The measurements demonstrate that the peak signal location moves in the -X and -Y direction as Z increases, as seen in Figure 5-3.

The final optical weighting function was created as an 81 x 81 x 16 matrix of values between 0 and 1, where 1 corresponds to the highest signal measurement. As seen in Figure 5-3,

the 1-dimensional sweeps of signal demonstrate Gaussian behavior. The 1-dimensional sweeps for peak signal locations and signal width were used to create a 2-dimensional Gaussian weighting function at all measured heights. A diagram of the experimental weighting function is shown in Figure 5-3 with the appropriate coordinate system. Figure 5-3 shows the outer boundary of the weighting function where only 1% of the maximum signal is detected; no signal is detected by the camera/spectrometer setup outside of this isosurface.

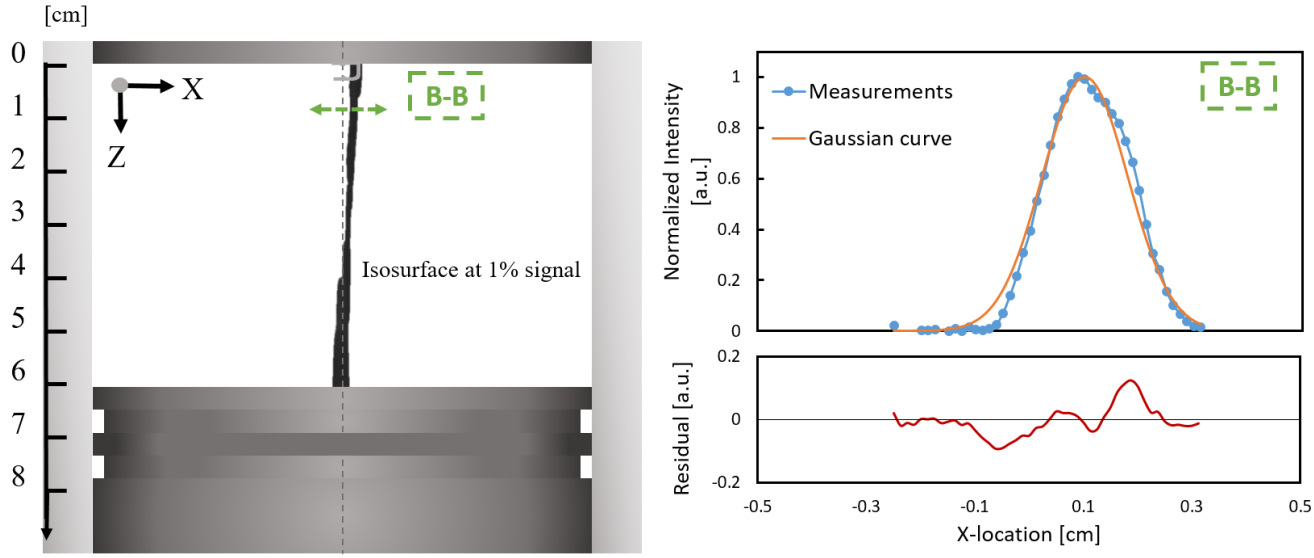

Figure 5-3: Left, diagram of optical volume coordinate system and isosurface showing measured signal at or above 1% of the maximum signal. Right, the weighting function is adequately described by a Gaussian function along with the X direction measurement at Z=1.04 cm.

5.2 Simulation Setup

5.2.1 Large-Eddy Simulations

Large-eddy simulations (LES) have been performed previously using STAR-CD. Key features of the models are a Smagorinsky subfilter-scale turbulence model, a simple energy-deposition spark-ignition model, and a modified thickened flame model for turbulent flame propagation. Details on methods and results of that study can be found in [93]. A subset of 19 cycles, referred to there as “Model 1” was selected for the work here and radiative emissions

calculations have been added as a postprocessing calculation to the already available three-dimensional fields of relevant quantities.

5.2.2 Radiative heat transfer post-processing

Here a subset of 19 consecutive Model 1 LES cycles from [93] is studied further to characterize in-cylinder radiative heat transfer, including quantitative comparisons between computed and measured spectral IR radiative intensities. The analysis is done in a post-processing mode, where instantaneous snapshots of computed three-dimensional fields of pressure, temperature, and radiatively participating species (H_2O and CO_2) are used to compute the corresponding fields of radiative emission and reabsorption. The radiation post-processing tools are implemented in OpenFOAM [94] The STAR-CD fields are interpolated to an OpenFOAM-compatible mesh, where the OpenFOAM mesh has an approximately uniform prescribed mesh spacing of 0.5 mm.

Initial results for several combinations of spectral models and radiative transfer equation (RTE) solvers were reported in [10]. There the radiative energy emitted over the full combustion chamber and reaching all bounding walls was considered, and the spectral range considered was limited to wavelengths between approximately 1.4 and 2.7 μm. Here more detailed quantitative comparisons between computed and measured spectral radiative intensities are made, which cover a wider spectral range and include explicit accounting for the optical volume that is viewed in the experiments. As discussed earlier, a stochastic photon Monto Carlo method with line-by-line spectral resolution (PMC-LBL) is used to compute radiative emission and reabsorption, using the latest available spectral database for radiative properties [54].

5.2.3 Optical volume modifications

To compute spectral radiative intensities that correspond more closely to those that are measured in the experiments, the local computed spectral radiative emission is multiplied by the local value of the optical weighting function described in Section 5.1.3. Only the radiative energy that is incident on a small wall patch (3 mm x 3 mm) centered at the base of the tilted isosurface shown in Figure 4, and with a close-to-normal incidence angle (*z*-direction cosine >0.99, approximately 9° with respect to vertical), is considered.

5.3 Results and Discussion

5.3.1 Optical Volume Effects

Table 5-2 provides the temperatures and pressures of the two simulated volumes for the ensemble-average simulated cycle at the four chosen crank-angles. The measured volume captures the early flame kernel more prominently. The simulated temperatures in the measured volume show that the cylinder core is significantly hotter. Therefore, the measured volume is biased to sample radiation that is stronger than the full volume, especially early in combustion. The measured volume temperatures at +8 ^{o}aTDC and +16 ^{o}aTDC are very similar, meaning these crank-angles will demonstrate similar magnitudes of radiative emissions. At +150 ^{o}aTDC the full volume and measured volume temperatures are similar as the fuel has been consumed in both cases; the remaining mixture is heated product gases which have reached a quasi-homogenous temperature throughout the chamber.

Table 5-2: Description of temperatures and pressures seen from both simulated volumes for the 19-cycle ensemble-averaged cycle

Crank Angle [^{o}aTDC]	Full Volume Temperature [K]	Measured Volume Temperature [K]	Pressure [kPa]
-8	857.7	2068.3	754.17
+8	1843.8	2414.5	1479.19
+16	2197.3	2410.8	1660.90
+150	1304.1	1330.4	125.11

Figure 5-4 shows the differences between the spectra resulting from the two simulation volumes. The peak magnitude of the radiative wall heat loss at +16 ^{o}aTDC from the full volume simulation is ~10^5 stronger than the measured volume simulation. The crank-angle development of the radiative spectra varies significantly. The radiative spectrum at -8 ^{o}aTDC is less than 10% of the peak-simulated radiation in the full volume simulations, but the same crank angle degree is ~50% of the peak-simulated radiation in the measured volume simulations. As seen in [38] and in Table 5-2, the measurement volume over-samples the early flame and changes the relative spectral temporal development. Unlike the full volume simulations, +8 and +16 ^{o}aTDC are of similar magnitude in the measured volume simulations. By comparing the two different volume simulations, it is clear that radiative behavior changes dramatically based on the sampling location.

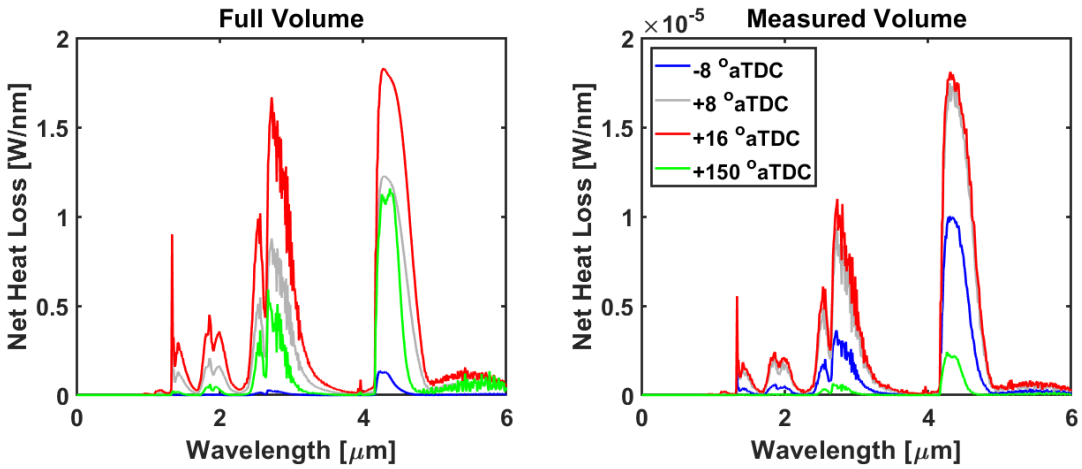

Figure 5-4: Comparison of simulations made with full cylinder volume and modified measured volume demonstrate that radiative development varies with measured volume consideration.

Table 5-3 contains the radiative emission, absorption, and heat loss for the ensemble-average simulated cycle for both simulated volumes. This table shows that the radiative emissions from the measured volume constitute a small fraction of the overall radiation, but the reabsorbed fraction is similar between both cases. Simulations showed 80-90% of emitted radiation being reabsorbed in high-pressure CI engines [37]. In this case, 35-55% of the total emitted radiation was reabsorbed before reaching the wall. The difference in reabsorption between these two simulations is due primarily to the high operating pressures in the CI engine simulations, which have peak pressures more than ten times higher than the TCC-III engine [37]. Higher pressures increase the molecular number densities and enhance radiative absorption. This radiative trapping redistributes energy within the combustion chamber and changes the temperatures and fluid properties where it is reabsorbed.

Table 5-3: Radiative emission, reaching walls, and reabsorbed for both simulated volumes of the ensemble-average cycle

Crank Angle [^{o}aTDC]	Full Volume			Measured Volume		
	Rad. Emission [W]	% Reabsorbed	% Reaching Wall	Rad. Emission [W]	% Reabsorbed	% Reaching Wall
-8	51.7	37.7	62.3	0.0173	21.9	78.1
+8	1146.2	45.6	54.4	0.0458	31.2	68.8
+16	2174	48.1	51.9	0.0483	36.5	63.5
+150	914.3	57.1	42.9	0.0062	41.0	59.0

The simulated values of species-specific radiative behavior of the ensemble-average cycle are shown in Table 5-4. This table shows the emitted radiation, radiative trapping, and radiative heat loss from 0-50 μm for H_2O and CO_2 for the four simulated crank angles. Both molecular species have stronger absorption later in the cycle due to their increasing concentration. CO_2 reabsorbs 30-50% of the emitted CO_2 radiation in the TCC-III simulations. The experiments, seen in the following suggestion, suggest that significantly more CO_2 reabsorption is occurring. The λ_2 region contains >90% of the total emitted CO_2 radiation from 0-50 μm, and so the measurements of λ_2 serve as an excellent proxy for the overall CO_2 radiation. CO_2 absorption is very sensitive to the local conditions.

Table 5-4: Simulated total radiative emission, radiative reabsorption, and radiation reaching the wall for two molecular species in the ensemble-averaged cycle. Percentage of the emission shown for absorption and radiative heat loss.

Crank Angle	Molecule	Rad Emission [W]	% Reabsorbed	% Reaching Wall
-8 ^{o}aTDC	H_2O	$4.6 * 10^{-3}$	2.4%	97.7%
	CO_2	$1.3 * 10^{-2}$	29.1%	71.0%
+8 ^{o}aTDC	H_2O	$1.4 * 10^{-2}$	5.9%	94.1%
	CO_2	$3.2 * 10^{-2}$	41.7%	58.3%
+16 ^{o}aTDC	H_2O	$1.4 * 10^{-2}$	7.9%	92.1%
	CO_2	$3.4 * 10^{-2}$	48.7%	51.3%
+150 ^{o}aTDC	H_2O	$1.6 * 10^{-3}$	14.8%	85.3%
	CO_2	$4.6 * 10^{-3}$	49.8%	50.2%

5.3.2 Spectral Comparison of Experiments and Simulations

The computed and measured radiative spectra can now be used to validate the PMC-LBL method. A function that minimizes $\|C * I_{exp} - I_{sim}\|$ across all measured wavelengths was used to identify C. The constant C was used to scale all measured spectra in the following results. The measured and simulated spectra of the three representative cycles are examined, and intra- and inter-cycle changes of the two large spectral features are seen to be broadly reproduced by the simulations.

Figure 5-5 shows the comparison between the ensemble-averaged simulations and the average-pressure representative cycle at the four crank angle locations. It is immediately clear that the H_2O/CO_2 overlap feature, λ_1, has strong agreement at all crank angles. However, the CO_2 feature, λ_2, has weak agreement. The λ_1 agreement suggests that the PMC-LBL simulations are accurately capturing the radiative development throughout the cycle. The agreement of the λ_1 wavelength

region is explored for the low and high-pressure cycles further below. The relative intensities of the λ_1 and the λ_2 features change visibly in the measurements. Early in combustion, measurements of the λ_2 emission band outweighs the λ_1 emission, but as the pressure and temperature increase the relative heights reverse. At + 150 ^{o}aTDC, the λ_2 emission band outweighs the λ_1 emission suggesting that the high pressure and temperature change the significance of radiative trapping. A similar trend is seen in the simulations, but not with a full reversal of the λ_1 and λ_2 magnitudes.

Given the strong agreement of the λ_1 region across all four crank angles, it is likely that the CO_2 absorption within the optically thick λ_2 wavelength band is not well captured in the simulations. One reason for this is the influence of the spark plug ground strap. The ground strap is prominently located in the simulated measurement volume around top dead center (TDC). In the simulations, the ground strap treated as a region of low-temperature gas rather than a solid boundary. The ground strap region could lower the H_2O and CO_2 concentrations and the overall temperature within the measured volume near TDC. Since CO_2 radiation is very sensitive to the local conditions, and the treatment of the ground strap could change its optical depth causing the noted spectral disagreement due to reduced reabsorption. Additionally, the temperature-dependent transmission of the sapphire piston window could reduce the measured radiation from 4-5 μm. At +150 ^{o}aTDC, the measured and simulated spectra in the λ_2 region have the closest agreement due to the lower temperatures, pressures, and the reduced influence of the ground strap. Additionally, late in the cycle the width of the CO_2 feature, which depends primarily on pressure through spectral collisional broadening [50], matches well.

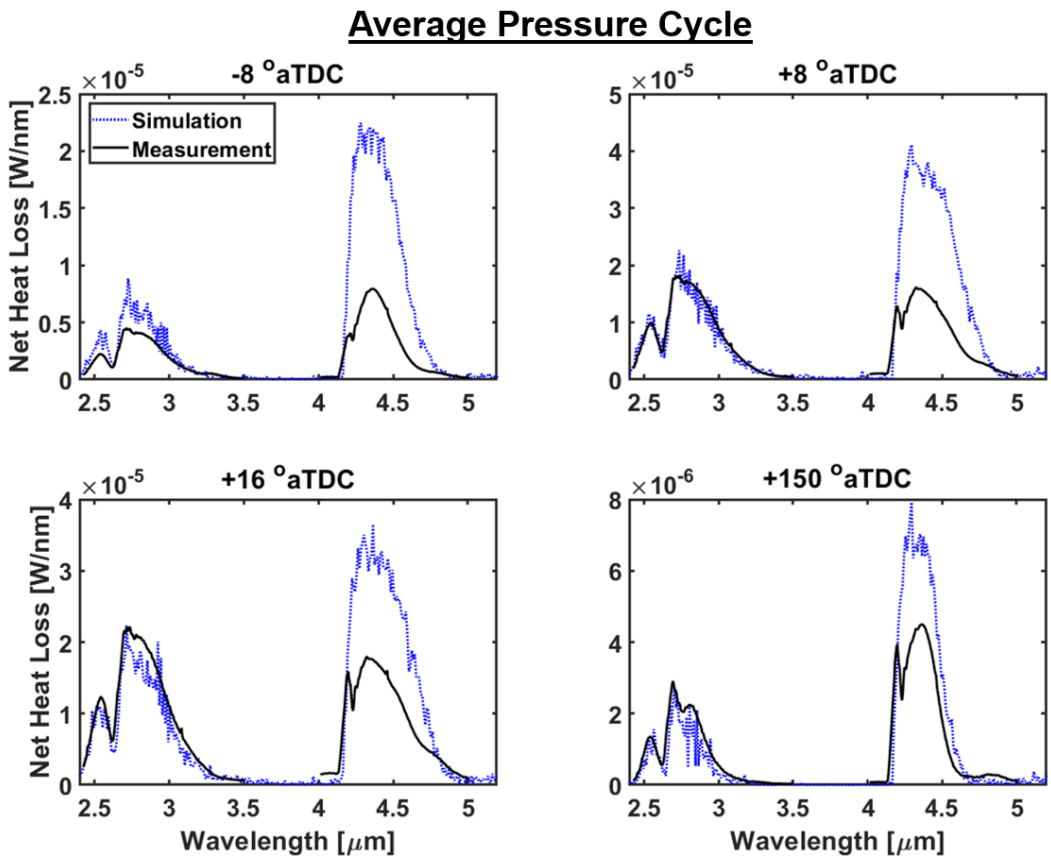

Figure 5-5: Comparison of measured volume simulations and spectral measurements

Figure 5-6 shows the measured and simulated net spectral emissions from λ_1 for the low and high-pressure representative cycles. The spectra agree well at all four crank angles for both representative cycles. The spectral resolution of the measurements is much lower than the simulations, but the overall magnitude, which changes an order of magnitude throughout the cycle, is in strong agreement. Slight disagreement can be attributed to the thermo-chemical differences between the chosen representative cycles. At +150 °aTDC, the spectral shape develops an additional peak at 2.8 µm. This peak corresponds to an H_2O feature and can be seen clearly in the measurements.

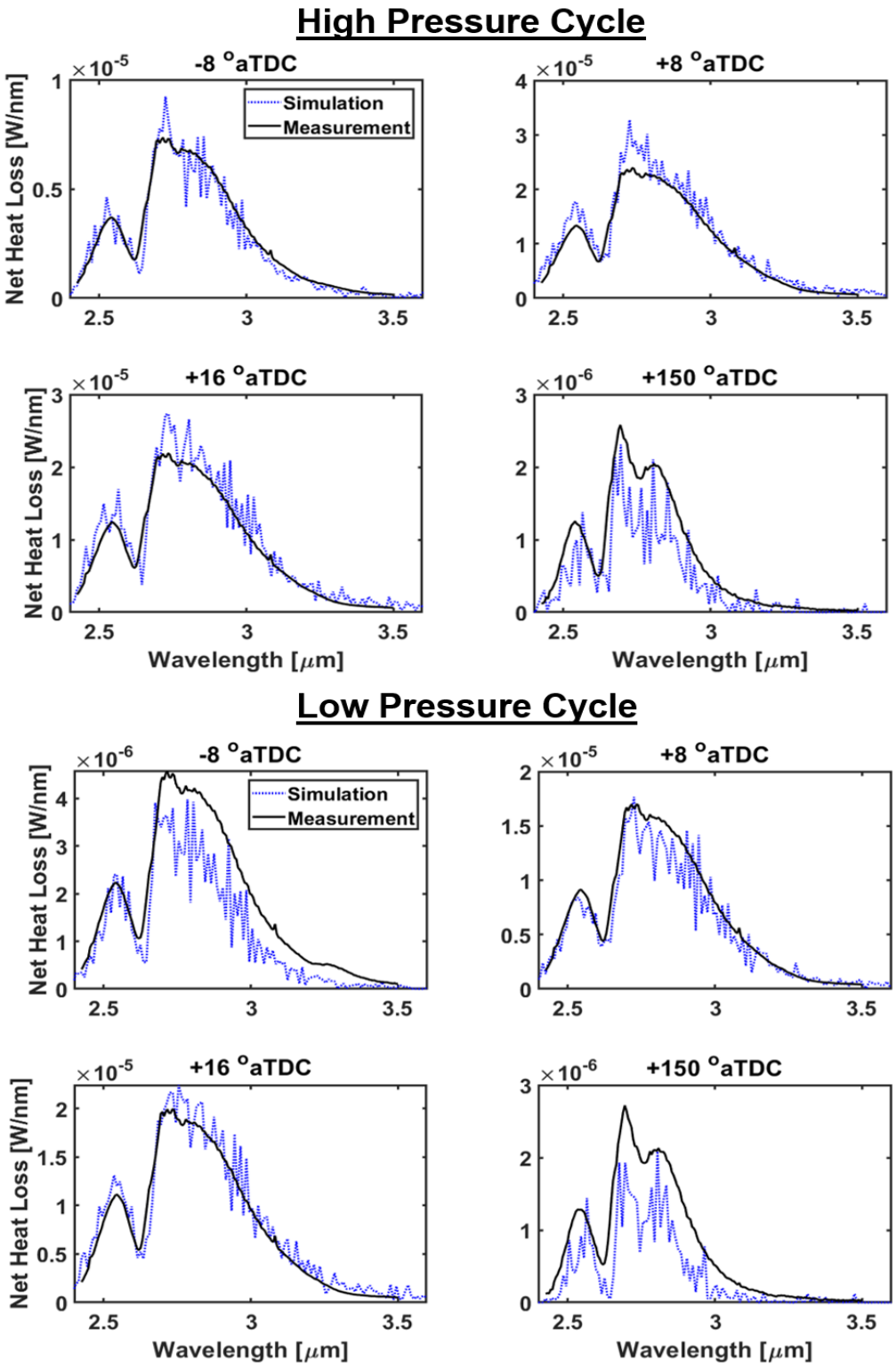

Figure 5-6: Comparison of measured volume simulations and spectral measurements from 2.4-3.4 um for the representative high pressure and low-pressure cycles. A strong agreement can be seen across the orders of magnitudes difference seen suggesting strong agreement.

Figure 5-7 demonstrates the numerical integration of the measured signal over the two measured wavelength bands, λ_1 and λ_2, for the ensemble-average cycle. The simulated spectra are integrated over the same wavelengths at the four simulated crank angles. This plot provides additional clarity about the "bulk" agreement of the spectra. The λ_1 region is mainly constituted of H_2O emission (~70%) and the λ_2 region is mainly constituted of CO_2 emission (>95%). The strong agreement of the λ_1 region is seen; the simulated points closely match the measured signal. The disagreement of the λ_2 region is also clear, and points to an under prediction of the CO_2 radiative trapping in the simulations.

Figure 5-7 also demonstrates the temporal development of the measured radiation. Both molecules radiate differently in high-pressure and temperature environments. This behavior is seen in the shape of the radiative temporal development. The λ_2 region can be seen to have a change in curvature around -8 ^{o}aTDC, this can be attributed to radiative trapping of CO_2. After +150 ^{o}aTDC, both plots show interesting features. In [29] the measured net heat loss against the crank angle curve was symmetric with no discernable signal beyond +90 ^{o}aTDC, but the updated measurement setup through the Bowditch piston has noticeable signal beyond +270 ^{o}aTDC. The radiation undulates late in the cycle; this variation is due to the changing pathlength as the piston moves. The changing pathlength explains the inflection point at +180 ^{o}aTDC in both plots of Figure 5-7 as the piston changes direction.

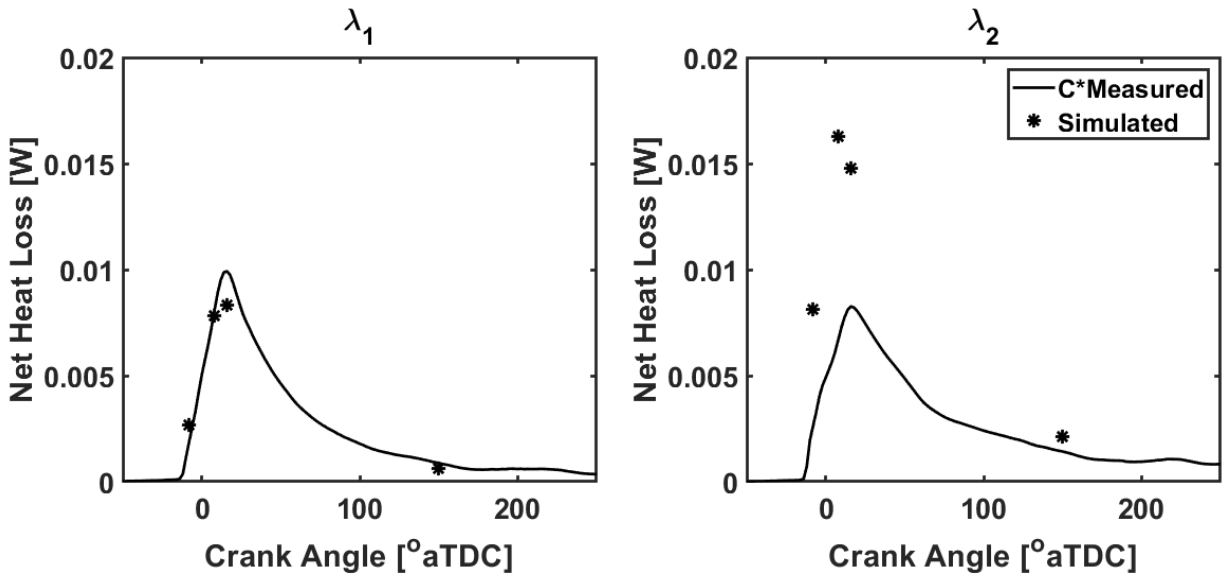

Figure 5-7: Radiative heat loss against crank angle for measurements and markers for simulated crank angle locations for the ensemble-average cycle.

Figure 5-8 shows the temporal development of the λ_1 radiation for the low and high-pressure representative cycles. The agreement of the simulated and measured net heat loss values is excellent at all four simulated crank angle locations. The high-pressure cycle demonstrates higher peak radiation occurring earlier in the cycle. This behavior is expected as the high-pressure cycle has a faster burning flame and earlier peak pressure. The low-pressure cycle has a slower burn and a peak net heat loss occurring close to +16 °aTDC.

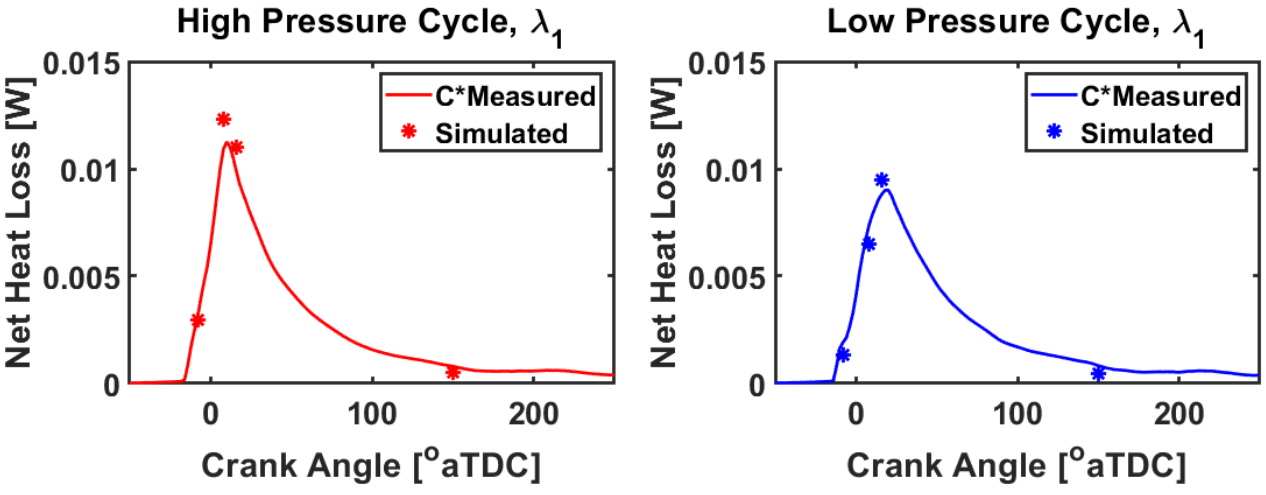

Figure 5-8: Net radiative heat loss against crank angle for measurements and markers for simulated crank angle locations for the low and high-pressure representative cycles.

Figure 5-9 shows the correlation between the peak pressure and peak signal for 100 continuous measured cycles. The peak signal from each individual cycle of the λ_1 and λ_2 measurements is compared to that cycle's peak pressure. λ_1 has a stronger correlation, R=0.87, between the measured signal and the in-cylinder pressure. This suggests that H_2O radiation is more sensitive purely to the pressure and temperature. However, the same trend is not seen for CO_2 radiation where the slope of the correlations is smaller and the correlation is lower, R=0.33. The magnitude of H_2O radiative heat loss is tightly connected to the CCV seen in the engine, but CO_2 radiative heat loss remains relatively constant with increasing pressures and temperatures. This behavior is due to the nature of CO_2 reabsorption, which is enhanced by increased pressure and temperature and counteracts the additional emission.

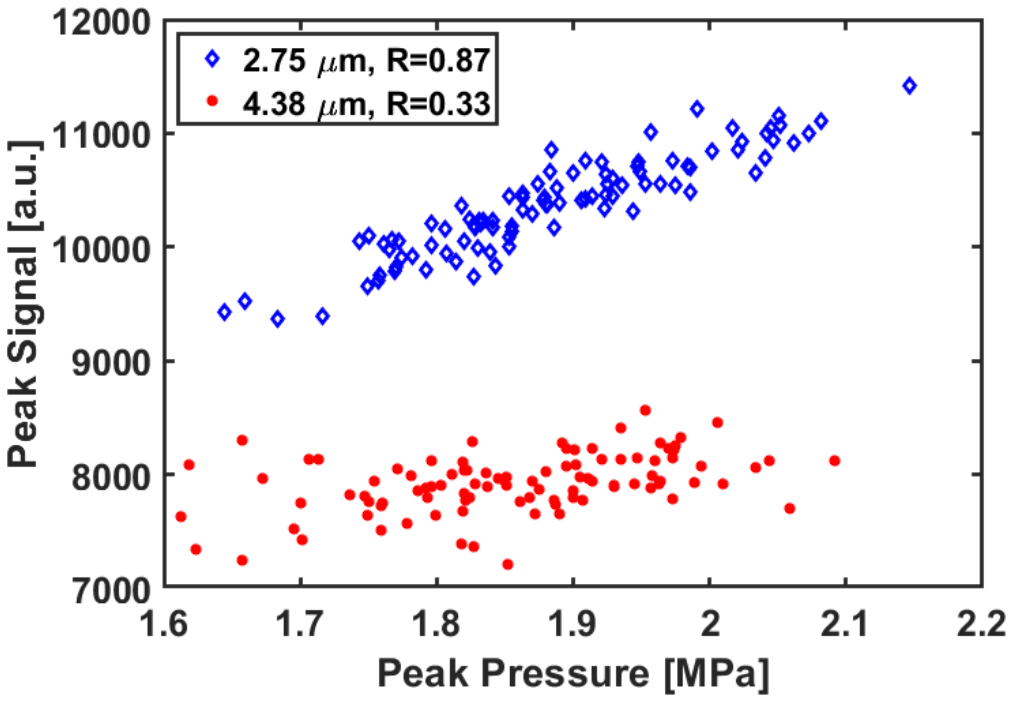

Figure 5-9: Peak signal vs. peak pressure at one wavelength of λ_1 and λ_2 for all 100 cycles. Lower correlation for λ_2 implies weaker connections between pressure and CO_2.

5.4 Summary

A detailed investigation of in-cylinder radiative heat transfer was performed on the spark-ignited TCC-III engine, using IR spectral measurements and LES with radiative post-processing models. Low, average, and high-pressure cycles of the stoichiometric propane-air fueled engine were analyzed. By comparing measurements and line-by-line photon Monte Carlo simulations, the influence of radiative trapping and radiative heat losses are better understood. The main conclusions are as follows.

This study provides partial validation of the photon Monte Carlo method. A strong agreement in the measured and simulated spectra of the wall radiation from 2.4-3.4 μm ($\lambda_1$region) was demonstrated when simulating the measured volume. This agreement was seen at different crank-angle locations across three representative cycles. This certifies that the PMC-LBL method accurately models the spectral and temporal radiative phenomena for an important wavelength region [35]. However, disagreement in the 4-5 μm region (λ_2) showed under prediction of CO_2 self-absorption. This mismatch was due partially to the treatment of the spark plug, which interferes with the measured volume. Comprehensive analysis of the treatment of the spark plug boundary and the measured volume location sensitivity will be evaluated in the future to complete the PMC-LBL validation. The complete validation of the photon Monte Carlo method will facilitate the development of simplified radiative transfer models that can be efficiently coupled to CFD simulations.

The amount of radiative reabsorption was quantified for three representative cycles. The validated simulations provide species-specific absorption information, and show that CO_2 re-absorbs significantly in this relatively low-pressure engine environment. Simulations in this chapter showed that up to 50% of CO_2 radiation was reabsorbed in the TCC-III engine, but the

measurements suggest that a significantly higher percentage of absorption occurs. Measurements of the cycle-to-cycle variations showed that high peak-pressure cycles are well correlated with high λ_1 radiative heat loss. The amount of radiative trapping and CCV is expected to be larger for cases with EGR, and Chapter 6 demonstrates experimental studies with CO_2 dilution to provide further insight into this.

Finally, this test case is well suited for the usage of a reverse Monte-Carlo (RMC) method where photons are traced in a time-reversal process from a small area of interest, in this case the measured wall patch. The RMC method would allow for similarly spectrally and temporally-resolved calculations, but would not require the solution of photon bundles that do not reach the chosen wall patch [95]. Therefore, the RMC method could be used effectively, in this case, to lower computational expense while matching the small wall patch seen in experiments [96].

Chapter 6 Analysis of Measured Molecular Radiation for Different Engine Conditions

This chapter presents measurements of the engine radiative spectra from twelve different TCC-III engine conditions. This parametric study aimed to characterize the IR radiative emissions leaving the combustion chamber and understand the role of self-absorption for a variety of engine conditions. The spectral measurements are correlated with the measured pressure dynamics data and burn characteristics. Data from synchronous infrared imaging and spectral acquisition of stoichiometric combustion is shown, and the spatial and spectral correlations are demonstrated. The crank-angle development of the spectral data is explored for all twelve conditions. Finally, a spectral analysis is performed for the different conditions, and the spectral influences of lean, rich, and/or dilute combustion are isolated. Following the analysis, a conceptual model of engine radiative behavior is summarized. Pressure analysis of radiative measurements from the TCC-III engine has been presented in the 13th International AVL Symposium on Propulsion Diagnostics and the Oil Gas Science and Technology Journal [29], [38].

6.1 Experimental Setup and Conditions

Table 6-1: Table describing conditions measured for 1300 rev/min run speed at 80 °C intake temperature. Superscripts describe the targets of different CO_2 dilution conditions.

Oxidizer	Equivalence Ratio [ϕ]	
Air	Leanest	0.59
	Lean	0.67
	Stoichiometric	1.00
	Rich	1.51
Air + 9% N_2 (by mass)	Lean	0.79
	Stoichiometric	1.00
Air + 19% N_2 (by mass)	Stoichiometric	1.00
Air + 5% CO_2 (by mass) *	Lean	0.79
	Stoichiometric	1.00
Air + 9% CO_2 (by mass) †	Stoichiometric	1.00
Air + 11% CO_2 (by mass)*	Stoichiometric	1.00
Air + 19% CO_2 (by mass) †	Stoichiometric	1.00
* diluted to match N_2 conditions with constant flame temperature † diluted to match N_2 conditions with constant mass fraction		

All the data presented within this chapter was measured through the sapphire piston window of the optical engine. The TCC-III engine was operated at 1300 rev/min on a variety of fuel/air/diluent mixtures with an intake plenum pressure of 40 kPa and an exhaust pressure of 98 kPa. All of the presented measurements were performed with an intake charge temperature of 80 °C to match the experimental conditions of Dr. Mark Greene and Dr. Mohammad Alzuabi [25],

[97]. All measurements had a two crank-angle resolution, i.e. one spectral measurement every two crank-angle degrees (CAD). The pressure data of the recorded cycles was analyzed and correlated with the spectral data in Section 6.2. The pressure data was captured every 0.5 CAD and provides information about the pressure dynamics, combustion landmarks, heat release, and the indicated mean effective pressure (IMEP) of each cycle.

The twelve measured conditions analyzed in this chapter are described in Table 6-1. Three different charge conditions were changed through these experiments: equivalence ratio (φ), N_2 dilution, and CO_2 dilution. The stoichiometric undiluted condition is used as the reference condition as it provides the most stable and industry-standard condition. The lean and rich values of φ match conditions used by Dr. Philipp Schiffmann to examine the root causes of CCV in the TCC-III engine and bring the engine to its variability limits [98]. The variability of the engine operation are described with the coefficient of variation of IMEP (COV_{IMEP}). The leanest condition (φ=0.59) and heavily dilute cases demonstrated variability exceeding COV_{IMEP}=50%. The variabilities of pressure and radiative conditions are explored further in Section 6.2. The addition of pre-mixed N_2 gas dilution reduced the flame temperature and reduced the laminar flame speed, but did not interfere with the radiative transfer because N_2 is IR-inactive [98]. Pre-mixed CO_2 gas dilution similarly reduced the flame temperature and laminar flame speed, but also enhanced radiative absorption.

Specific flame parameters were isolated to allow for an effective comparison of the N_2 and CO_2 dilution cases. The first dilution condition was aimed to maintain a constant mass fraction dilution and was performed for the 9 wt% and 19 wt% cases of N_2 and CO_2 to maintain the same mass fraction of fuel/air mixture. The second dilution condition aimed to maintain the same theoretical flame temperature for the two diluents. Previous work examining the impact of diluents

on flame temperature and NO_x formation provided data describing the theoretical flame temperature with different amounts of N_2 and CO_2 dilution [99]. This data allowed for TCC-III engine operation with different wt% of dilution but closely matching theoretical flame temperature, which would isolate the radiative magnitude due to the mixture temperature. The matching theoretical flame temperature conditions were 9 wt% and 19 wt% cases of N_2 and 5 wt% and 11 wt% cases of CO_2. Additional cases exploring lean and dilute operation with N_2 and CO_2 were measured as these approach realistic conditions for low-temperature combustion.

Figure 6-1 shows the ensemble-averaged pressure traces of the different measurement conditions described in Table 6-1. All plots contain the stoichiometric (φ=1) and undiluted condition for reference. The top plot shows the influence of the equivalence ratio on the pressure without the inclusion of dilution. The location of peak pressures occurs earlier with lean cases and later with the rich case. Additionally, a stoichiometric-charge motored (unfired) pressure trace is shown in the plot as a reference to demonstrate the increases in pressure for the leanest case; the peak-pressure of the motored pressure trace occurs at -0.5 °aTDC. The middle plot shows the pressure traces of the measurements with the different amounts of N_2 dilution and the lean/dilute N_2 condition. The bottom plot demonstrates the pressure traces with different amounts of CO_2 dilution and the lean/dilute CO_2 condition. It is clear that the heavy dilution cases drastically reduce pressure as shown in the middle and bottom plots.

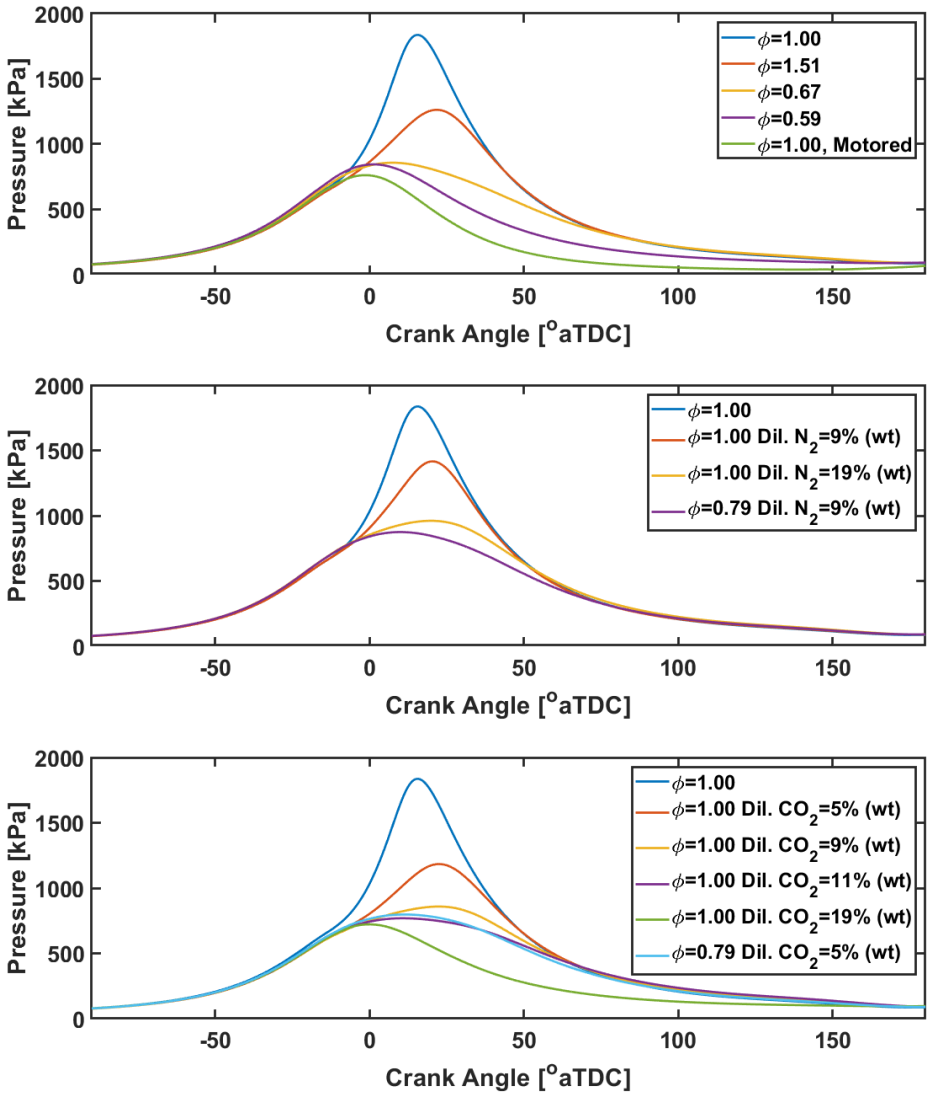

Figure 6-1: Top, pressure traces for equivalence ratio study without dilution. Middle, pressure traces for nitrogen gas dilution study. Bottom, pressure traces for carbon dioxide gas dilution study.

As described above, the spectral characteristics of certain N_2 and CO_2 dilution measurements are compared in Section 6.3. The pressure traces of these selected conditions are shown in Figure 6-2. There is clear disagreement in the average pressure traces between the N_2 and CO_2 dilution cases in most conditions. The N_2 dilution case has a higher peak pressure in all three cases. However, the CO_2 dilution cases set to match theoretical flame temperature have a

closer agreement to N_2 dilution. These disagreements root from the large impact CO_2 has in reducing the laminar flame speed [99].

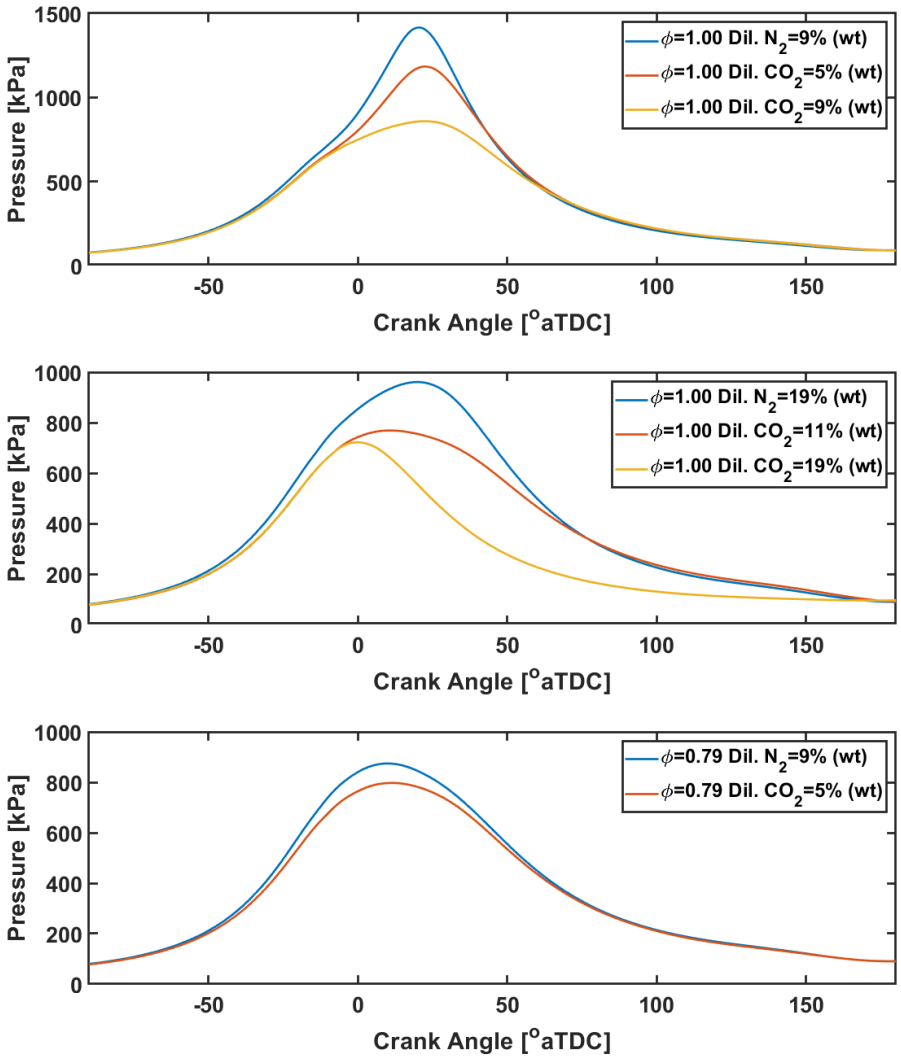

Figure 6-2: Pressure traces of dilute nitrogen and carbon dioxide measurement cases that are compared spectrally. Lower CO_2 dilution cases agree better with N_2 dilution cases.

6.2 Analysis of Radiation and Engine Operation

6.2.1 Spectra and Engine Operation

This section demonstrates the correlations between the engine pressure metrics and the radiative measurements at a variety of equivalence ratios for the TCC-III engine. Similarly to Chapter 5, two wavelength ranges were measured for each of the different engine operating

conditions. Table 6-2 describes the measured wavelength ranges, λ_1 and λ_2, a label used for the experiments. Also in Table 6-2 are the measured wavelengths and relevant molecules. Early development of the correlations between the engine pressure data and radiative measurements was presented in the 13th International AVL Symposium on Propulsion Diagnostics and published in the proceedings [29].

Table 6-2: Wavelength ranges and corresponding molecules of the measurements

Experiment Label	Measured Wavelengths	Relevant Molecules
$\boldsymbol{\lambda_1}$	$2.45 - 3.45\ \mu m$	H_2O, CO_2
$\boldsymbol{\lambda_2}$	$4.0 - 5.0\ \mu m$	CO_2

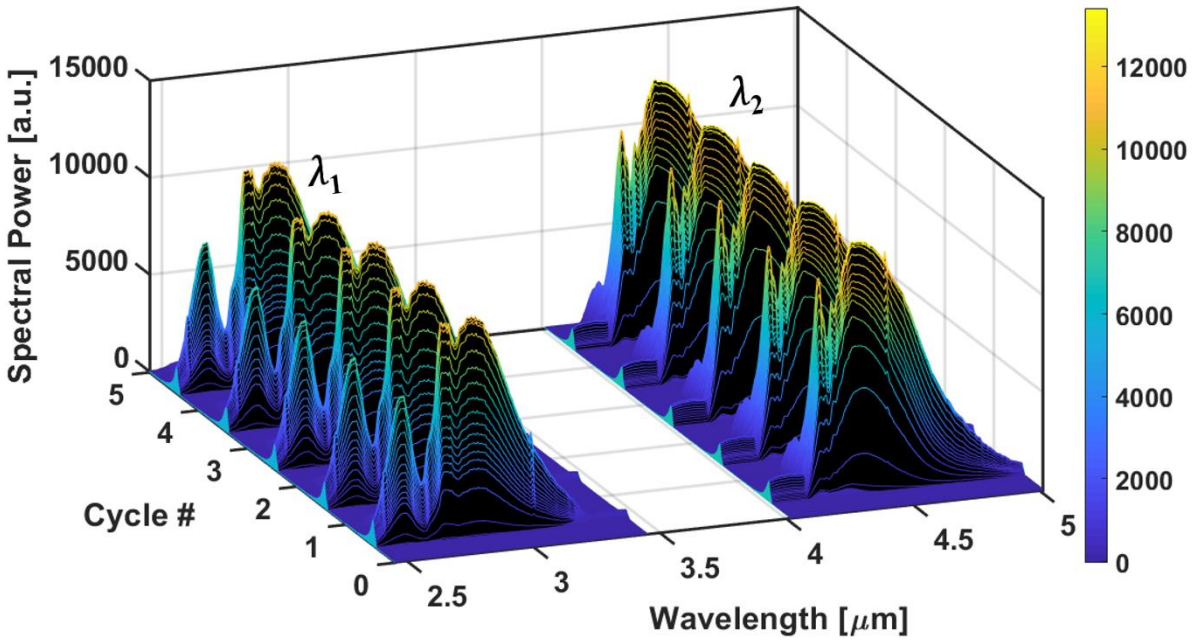

Figure 6-3: A three-dimensional IR emission dataset produced by the optical engine IR spectroscopy setup. Both measured wavelength regions, λ_1 and λ_2, are labeled.

Figure 6-3 shows an example of the three-dimensional dataset produced by the spectrometer/camera setup with the engine operating at φ=1. The spectral radiation shown in

Figure 6-3 spans 2.45-5.0 µm with each colored line corresponding to a measurement. The color scale to the right represents the spectral power measured in camera counts with arbitrary units. This plot shows the first five measured cycles of the 100-measured cycles. While not immediately clear from Figure 6-3, there are changes in the spectral power from cycle to cycle. The relevant molecular species are identified in Table 6-2. This dataset can be presented in several informative ways by displaying two-dimensional subsets or "slices." For example, a subset of constant crank angle within a cycle gives the emission spectrum at the crank angle. A subset of constant wavelength gives the time-dependent emission at that wavelength, which is explored next.

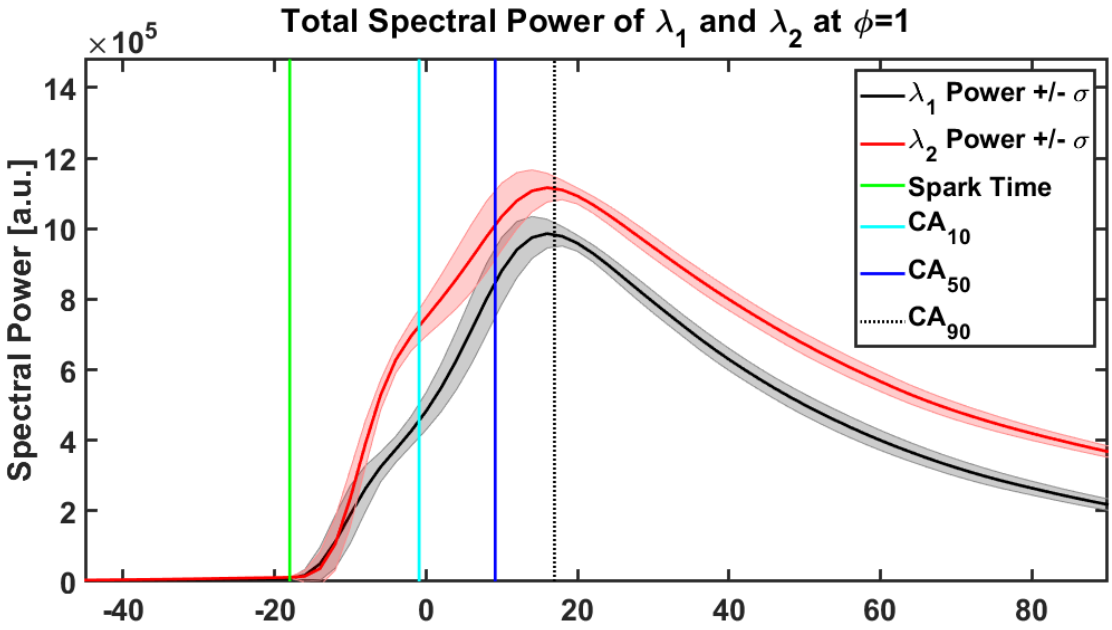

Figure 6-4: Total spectral power of the average, stoichiometric cycle from λ_1 and λ_2 shows temporal differences in H_2O and CO_2 radiative development. Spectral development of λ_2 can be seen to slow around TDC. Four combustion landmarks are also shown.

Figure 6-4 was produced by computing the average and standard deviation (over all 100 cycles) of the spectrally integrated (over the entire measured wavelength range) emission, hereafter "total spectral power", at each crank angle. This procedure was performed for both λ_1 and λ_2. The average total spectral power of λ_1 is shown with a solid black line and the standard deviation is represented with a gray shaded area; similarly, λ_2 is shown with a solid red line and the standard

deviation is represented with a red shaded area. Vertical lines indicate four combustion landmarks: spark timing, CA_{10} CA_{50}, CA_{90} (CA_x refers to the average crank angle where x % mass fraction of the fuel has been burned for the 100 measured cycles). This plot illustrates how the flame emission evolves during a combustion cycle. The peak emission of both λ_1 and λ_2 occurs near CA_{90} and the standard deviation of the integrated emission, which is one measure of cycle-to-cycle variability, is greater before peak emission than after for both plots. This connection between the burn fraction and the molecular emission demonstrates the importance of the radiative heat released during combustion; the rising edge of the emission curve maps to the CA values, and the overall curve shows the timescale over which significant radiative heat transfer occurs. Distinct differences between the λ_1 and λ_2 total spectral power are due to the primary molecule of each region. The λ_2 emission, due to CO_2, has a change in slope around TDC due to radiative trapping; CO_2 radiative trapping was seen in the previous chapter to increase strongly near TDC. In Figure 6-4, λ_1 emission is seen to increase more steadily due to reduced radiative trapping from H_2O. These total spectral power trends and their derivatives are further explored in Section 6.3.

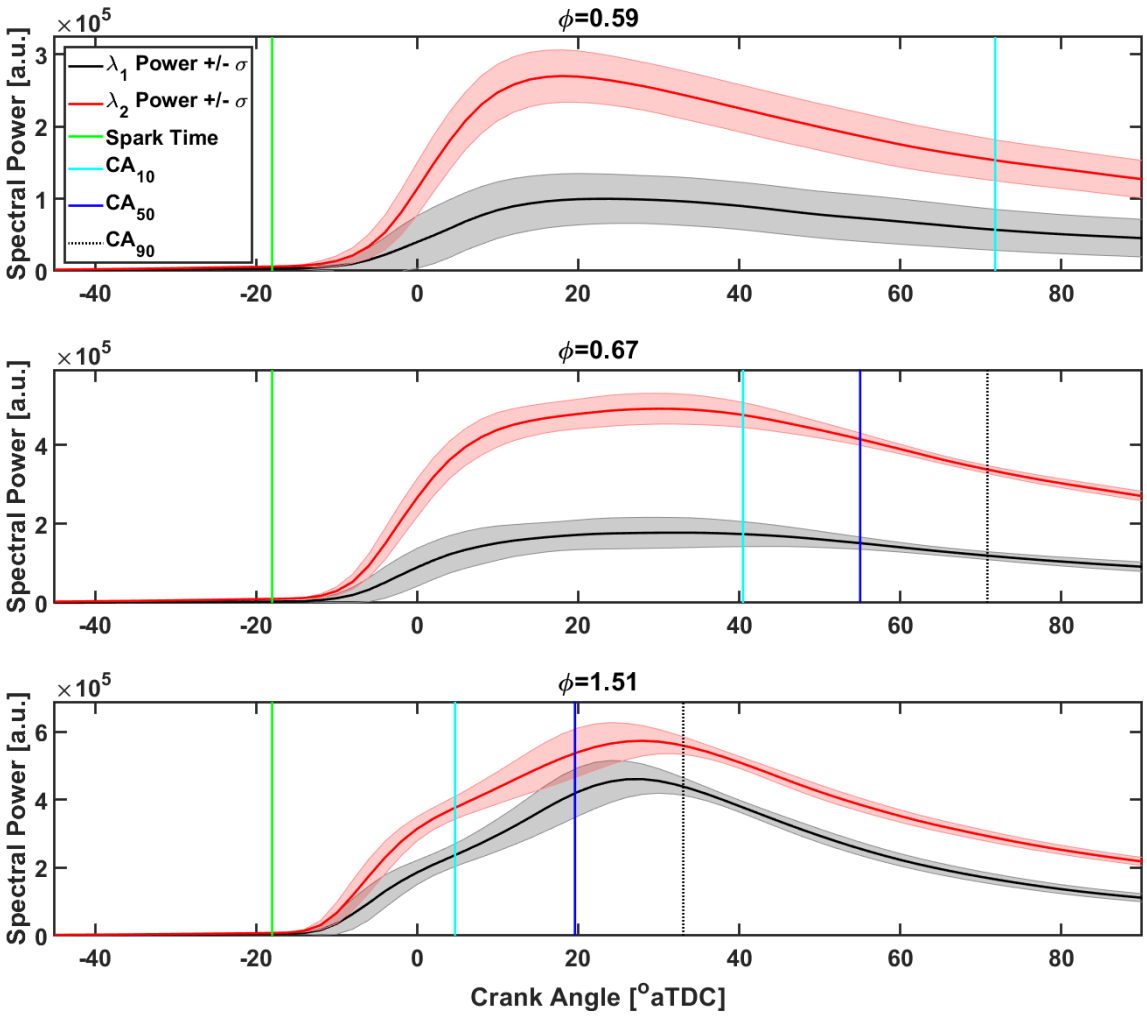

Figure 6-5: Top, total spectral power of the φ=0.59 from λ_1 and λ_2. Middle, total spectral power of the φ=0.67 from λ_1 and λ_2. Bottom, total spectral power of the φ=1.51 from λ_1 and λ_2. Lean conditions demonstrate high variability and have significantly stronger λ_2 radiation due to higher CO_2 concentrations. Four combustion landmarks are also shown.

Figure 6-5 shows the total spectral power of λ_1 and λ_2 for the other measured equivalence ratios. The standard deviation of total spectral power, due to the flame variability, is notably high in these extremely rich and lean cases. However, the φ=0.67 and φ=1.51 show lower variability in the flame extinction period. The radiative behavior of φ=0.59 for both λ_1 and λ_2 does not follow the trends seen in Figure 6-4. CA_{10} occurs around +60 °aTDC due to the extremely lean condition causing misfires. The φ=0.59 pressure data demonstrated that only 9 cycles burned 90% of the provided fuel mass before the exhaust valve opened, highlighting a strong trend of partial burns and misfires. The average behavior of spectral power is similar between λ_1 and λ_2, and the standard

deviation of the flame spectral power remains high throughout the cycle. Later in this chapter, the φ=0.59 case provides interesting information about radiative variability and its connection with pressure. The second row of Figure 6-5 shows the φ=0.67 case has a slow flame burn due to the lack of available fuel. The radiative curve shape is seen to flatten from ~20 to ~40 °aTDC suggesting that the flame slowly burns and that flame extinction occurs late in the cycle, around +60 °aTDC, at which point the flame standard deviation begins to decrease. Finally, the bottom row shows the rich case, φ=1.51. This condition demonstrates similar radiative behavior to the φ=1.00 case including the change in the slope of the λ_2 due to radiative trapping, but the flame development is slower as seen by the CA_x locations. Both lean cases have relatively higher λ_2 radiation demonstrating that lean conditions have CO_2 dominant radiation.

Figure 6-6 shows the COV_{IMEP} and coefficient of variation of total spectral power of the λ_1 region at TDC (COV_{RH}) to explore the engine variability of the presented cases. The lean cases are seen to have very high COV_{IMEp} and COV_{RH}, and a minimum variability is seen at the stoichiometric condition. The relative trend of COV agrees between the spectral measurements and the pressure measurements.

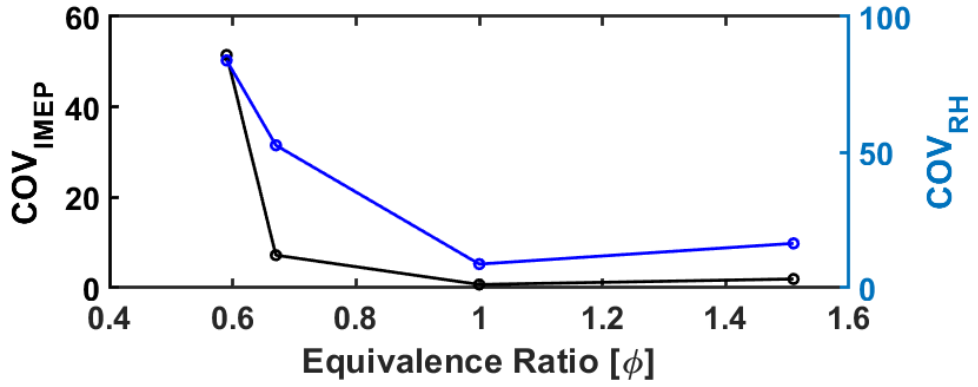

Figure 6-6: Left axis, CoV_{IMEP} for various equivalence ratios. Right axis, COV_{RH} for various equivalence ratios. Lean conditions are shown to generate high COV.

Figure 6-7 shows the relationships between IMEP and peak spectral emission demonstrated through the Pearson correlation coefficient, R, which is a measure of linear correlation between two variables. R is a value between -1 and 1; an R=1 demonstrates a perfect positive linear correlation, an R=0 demonstrates no linear correlation, and an R=-1 demonstrates a perfect negative correlation (e.g. an increase in one variable results in a decrease in another variable). This plot shows both the λ_1 and λ_2 correlation to explore the species-specific correlations. Each point represents the peak pressure and peak IR signal of a single cycle at the corresponding condition. The φ=1.00 case shows a negative correlation, R= -0.41 and R= -0.42, between spectral power and IMEP at both λ_1 and λ_2. This trend shows that there is valuable information about engine operation and its variability in the emission spectrum. For example, if the peak signal is high, IMEP will be lower for that cycle; this result is due to the fast combustion producing higher peak signal — compare to Figure 6-4 for the relationship between IR emission and CA_x — and earlier peak pressure. The TCC-III engine at this condition is optimized to have slower combustion, so the correlation demonstrates that higher peak signal cycles reached peak pressure too soon and the overall IMEP was negatively affected.

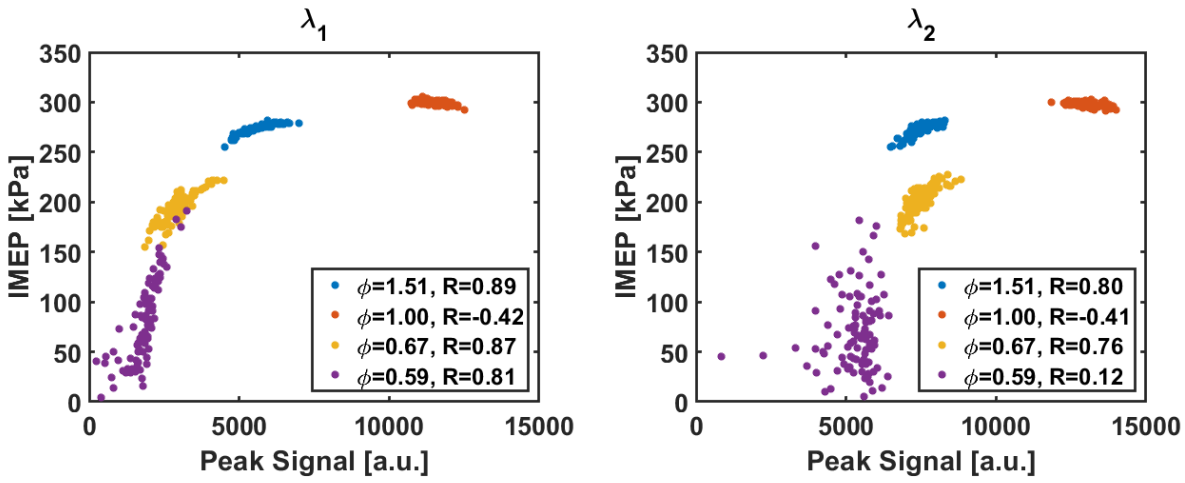

Figure 6-7: IMEP of each cycle correlates well with peak spectral power measured at both λ_1 and λ_2.

A strong correlation exists for the lean and rich cases of λ_1, suggesting that in these conditions the high radiative power cycles will have the highest IMEP. Following the reasoning above, it is expected that the faster burning cycles of these lean and rich conditions will reach higher IMEP. However, the φ=0.59 case has a poor correlation with IMEP for the λ_2 wavelengths. This is surprising given that the total spectral power of λ_2 was ~3 times stronger than the λ_1 for the φ=0.59 case in Figure 6-5. This behavior is due to the extreme flame variability and the high propensity for misfires combined with the CO_2 trapping.

Table 6-3 explores the Pearson correlation coefficients for other spectral and pressure variables for the previously examined conditions. Table 6-3 only examines the correlations with λ_1 wavelengths as these demonstrate a stronger correlation. As previously noted, the magnitude of λ_1 radiative heat loss is tightly connected to the CCV seen in the engine, but λ_2 radiative heat loss has weaker connections to increasing pressures and temperatures due to the influence of radiative trapping. This behavior is due to the nature of CO_2 reabsorption in the λ_2 band, which is enhanced by increased pressure and temperature and partially counteracts the additional emission. The table shows correlation values for the peak signal, signal at -10 °aTDC, and signal at +10 °aTDC. These CAD locations were chosen because the peak signal location changes between cycles and conditions so signal at a specific location would allow repetitive sampling for diagnostic usage. The correlation of the -10 °aTDC signal examines early flame information in regards to the pressure data and provides a predictive measure. The signal at +10 °aTDC occurs around CA_{50} for the stoichiometric case and compares the developed flame signal with the pressure metrics.

As seen in the table, the peak signal correlations produce the strongest correlations. The correlations for signal seen at -10 and +10 °aTDC change strongly due to the varying conditions, but the peak signal correlations remain relatively strong for all conditions. Correlations between

the peak signal and total heat release suggest that the φ=1.00, 1.51, and 0.67 cases with the highest signal would produce the lowest total heat release. Particularly in the φ=1.51 case it seems that lower peak signal cycles had higher total heat release; however, the IMEP would suffer. This is seemingly counter-intuitive as one would expect higher heat release for high IMEP cycles, but the φ=1.51 case has an abundance of fuel. Therefore, high IMEP cycles may have a faster burn but leave unburned fuel where insufficient oxidizer is available. The negative correlation at φ=0.67 is equally counter-intuitive given the strong correlation with IMEP. Here the author similarly suggests that the faster burning cycles reached higher peak signals, but slower flame cycles more completely burn the fuel leading to higher overall heat release.

From Table 6-3 it is clear that the stoichiometric flame has the stronger correlations between early flame signal (-10 °aTDC) and the peak and average pressures. However, these correlations are weak and are unlikely to be useful in predicting operating conditions. Similarly, the φ=1.51 case shows some correlation with early flame signal but it is weaker than the stoichiometric case. The two lean conditions have weak correlations at -10 °aTDC due to the slow flame development and suggest that the early flame development of these conditions tells very little about the resulting flame. Therefore, the usage of early flame information is unlikely to be particularly useful in a real-time predictive sense. While not explored in this section, similarly strong correlations were found for conditions that included dilution. Tables describing the pressure and spectral correlations for additional conditions can be found in Appendix A.

Table 6-3: Comparison of R correlation values for spectral and pressure metrics

φ	R{row,column}	Peak signal	Signal @ -10 aTDC	Signal @ +10 aTDC
1.00	**IMEP**	-0.42	-0.14	-0.71
	Peak Pressure	0.82	0.44	0.96
	Avg. Pressure	0.61	0.44	0.93
	Total Heat Release	-0.53	-0.18	-0.82
1.51	**IMEP**	0.89	0.32	0.79
	Peak Pressure	0.95	0.32	0.94
	Avg. Pressure	0.93	0.32	0.94
	Total Heat Release	-0.76	-0.29	-0.66
0.67	**IMEP**	0.87	0.18	0.53
	Peak Pressure	0.88	0.11	0.54
	Avg. Pressure	0.90	0.16	0.52
	Total Heat Release	-0.66	-0.01	-0.36
0.59	**IMEP**	0.81	0.17	0.47
	Peak Pressure	0.46	0.19	0.15
	Avg. Pressure	0.81	0.18	0.46
	Total Heat Release	0.71	0.16	0.43

6.2.3 Infrared Images and Spectra

In this section, the flame development is explored further through a combination of spectroscopy and imaging. These experiments were performed through the quartz cylinder liner using the Onca camera for spectroscopy and Cheetah camera for imaging as described in Chapter 3. This comparison of spatial and spectral flame characteristics was presented in the 13th International AVL Symposium on Propulsion Diagnostics and published in the proceedings [29]. In these experiments, the 1.3-1.7 µm region falls within the sensitivity range of both cameras and contains appreciable H_2O radiation. Combining spectroscopy and imaging allows spectral and spatial features of the flame to be linked. The images and spectra were captured synchronously at a 4 CAD resolution with the TCC-III engine operating with a stoichiometric propane/air charge, an intake pressure of 40 kPa, an exhaust pressure of 101.5 kPa, and a spark timing of -18 ^{o}aTDC.

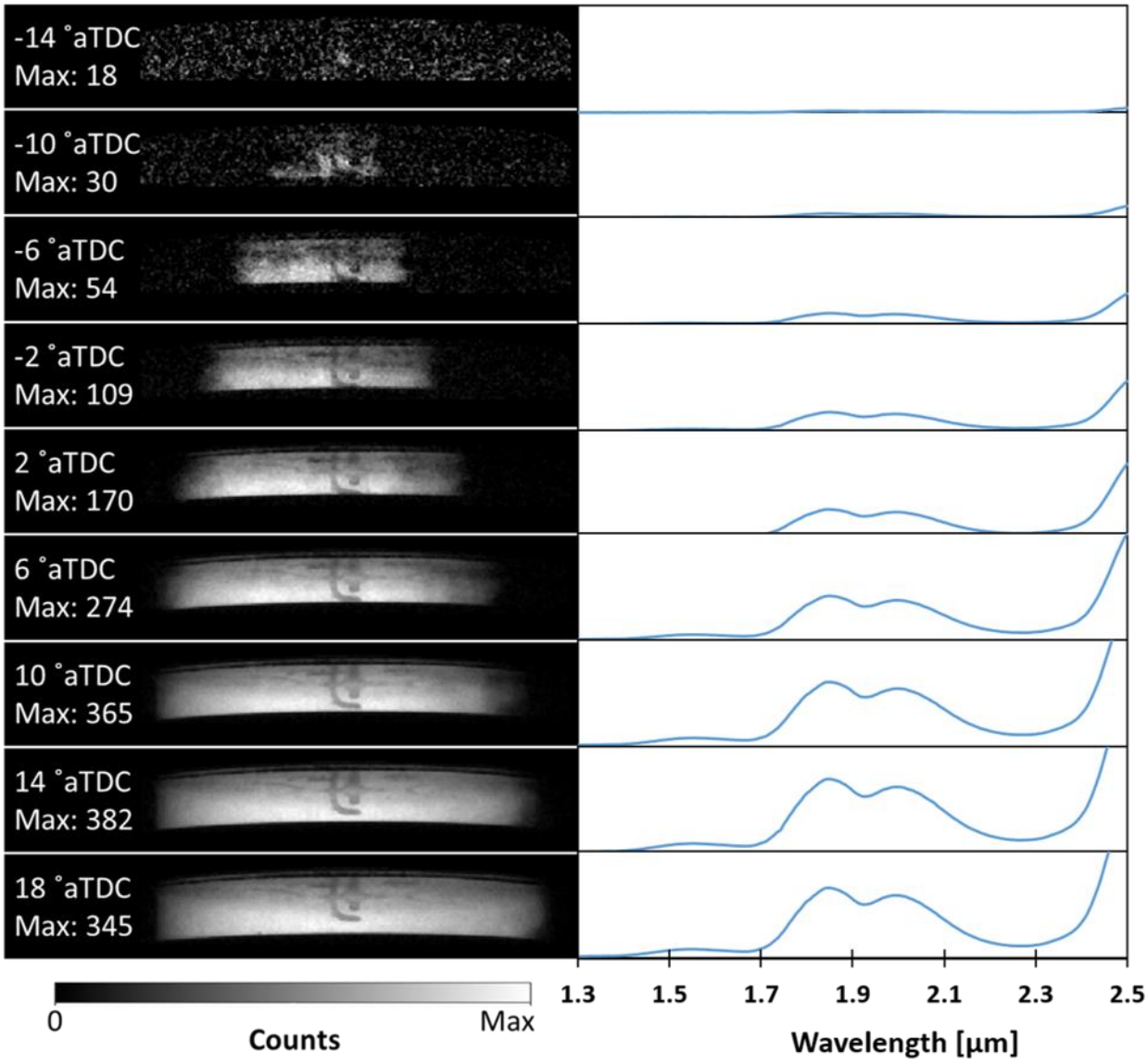

Figure 6-8: Images and spectra recorded simultaneously at nine crank angles within a single engine cycle show synchronous growth in the image and spectral signal. Images captured and provided by Dr. Ahmet Mazacioglu [29].

Figure 6-8 shows sample images and spectra recorded simultaneously by the Cheetah and Onca cameras, respectively, at nine crank angles during a single combustion cycle. The spectral power values are not shown, but the ordinate axis has a constant scaling to emphasize the growth in the spectral signal. As the figure illustrates, the early flame development is captured both spatially and spectrally. The maximum image brightness and peak spectral power in Figure 6-8 occur at +14 ^{o}aTDC; at this time, the flame has reached the cylinder wall. This peak signal aligns

well with previously demonstrated spectra, which demonstrate peak spectral power at +16 ^{o}aTDC. It is particularly interesting to observe the flame at -10 and -6 ^{o}aTDC as these early flames are used throughout this dissertation in spectral comparisons and for early flame correlations in Table 6-3. The spatial signal from the Cheetah camera was summed over the clearance volume for each measured crank angle degree and compared with the total spectral power from the Onca spectra integrated over the 1.3-1.7 μm region at the corresponding crank angle. The results shown in Figure 6-9 demonstrate a very high correlation of R=0.996, verifying that the two measurements are correctly synchronized. Dr. Ahmet Mazacioglu captured and analyzed the IR images and image data used to create Figure 6-8 and Figure 6-9.

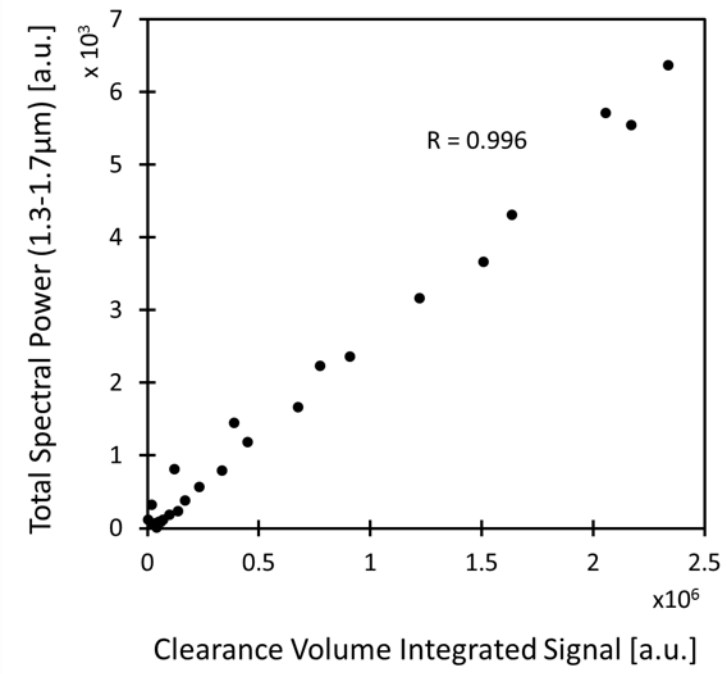

Figure 6-9: The spatially integrated (over the clearance volume only) signal recorded by the imaging camera correlates very strongly with the spectrally integrated signal recorded by the spectroscopy camera. Data and plot provided by Dr. Ahmet Mazacioglu [29].

Further collection and comparison of synchronous spectral and spatial data could permit exploration of the spatial variation of molecular emission. Images would show locations of emitting molecules while spectra would provide a measure of the radiative magnitude and species-

specific emissions. Understanding the spatial development of molecular radiative heat transfer, especially in lean and dilute operation, would provide spatial experimental data about the influence of molecular radiative heat transfer and radiative trapping.

6.3 Spectral Characteristics of Varied Conditions

6.3.1 Full spectrum

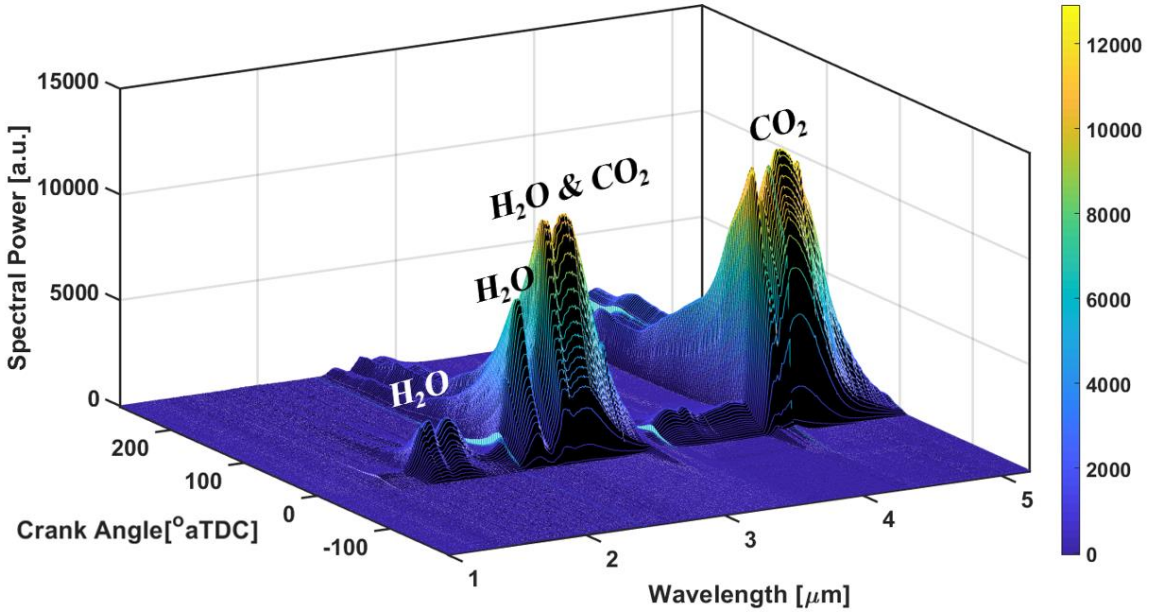

Figure 6-10: A three-dimensional IR emission dataset produced by the optical engine operating at φ=1 without dilution measured with the IR spectroscopy setup.

Figure 6-10 is comprised of five separate measurements of the coarse spectra that were stitched together along the wavelength axis to cover the entire range of experimental sensitivity. Each colored line corresponds to a spectral measurement. The color scale to the right represents the spectral power of the colored spectra. Spectral discontinuities can be seen at ~1.5 µm, ~2.5 µm, ~3.5 µm, ~4.5 µm at the locations of stitching due to spectral CCV between measurements. Figure 6-10 shows an example of the three-dimensional dataset produced by the

spectrometer/camera setup with the engine operating stoichiometrically at a 40 kPa intake pressure / 98 kPa exhaust pressure. This plot shows the first recorded cycle of each measurement. The molecular species and vibrations can be identified from the emission spectrum and are labeled in the figure. The spectroscopic range discussed in this section, 1.0-5.2 μm, contains several strong H_2O vibrations and CO_2 vibrations, which are described in Table 6-4 [51]. This table is replicated from Chapter 2 to provide a reminder of the relevant vibrational transitions that are measured. It is important to note that the fundamental vibrations (boldface in Table 6-4) often have the highest population and thus have the strongest intensity bands. This explains the strong emission from 2.4-3.4 μm, due to the υ_1 and υ_3 vibrations of H_2O, and from 4-5 μm, due to the υ_3 vibration of CO_2.

Table 6-4: Relevant H_2O and CO_2 vibrations across the entire measured spectrum, 1-5.2 μm. Fundamental vibrations in boldface.

λ_{H_2O} [μm]	H_2O Vibration	λ_{H_2O} [μm]	CO_2 Vibration
1.14	$\nu_1 + \nu_2 + \nu_3$	1.96	$2\nu_1 + \nu_3$
1.38	$\nu_1 + \nu_3$	2.01	$\nu_1 + 2\nu_2 + \nu_3$
1.45	$2\nu_2 + \nu_3$	2.06	$4\nu_2 + \nu_3$
1.88	$\nu_2 + \nu_3$	2.69	$\nu_1 + \nu_3$
2.66	$\boldsymbol{\nu_3}$	2.77	$2\nu_2 + \nu_3$
2.73	$\boldsymbol{\nu_1}$	4.26	$\boldsymbol{\nu_3}$
3.17	$2\nu_2$	4.82	$\nu_1 + \nu_3$
		5.17	$3\nu_2$

6.3.2 Theoretical Expectations of Spectra Characteristics

The comparison of spectral measurements is facilitated by reviewing the ways that spectra change due to different parameters. This section seeks to expand on the theory in Chapter 2 to

provide initial insight into what is theoretically expected from the varied charge conditions explored in the following sections. Specifically, this section describes the expected spectral characteristics for changes in pressure, temperature, number density, and absorption.

The molecular population of a specific energy level determines the strength of the spectral signal. The Boltzmann distribution describes the distribution of molecules over its allowed quantum states. The fraction of molecules at a specific energy level is described by the following equation [50].

$$F_i = \frac{n_i}{n} \propto \exp\left(-\frac{\epsilon_i}{T}\right)$$

Where ϵ_i is the energy level, n_i is the number of molecules at ϵ_i. The distribution of molecules at different energy levels is directly related to the temperature. The higher the population of a molecule at a specific energy level, the higher the measured signal of that transition. Functionally, this means that increases in the number density of a molecule will increase the signal, and an increase of the temperature will increase the measured signal of high energy transitions. Engine charges that reach higher temperatures and higher molecular number densities will have a stronger emitted signal. Increasing temperatures cause a higher population at higher rotational energy levels. This causes higher temperature emissions to emit predominantly in the R-branch [48]. Additionally, the spacing of the P and R band rotational transitions can cause shorter-wavelength R branch emissions to wrap around on themselves and occur very closely together, which creates a "band head" [50]. The CO_2 υ_3 vibration has a strong band head at ~4.17 μm [100], and H_2O has shown band heads in the shorter wavelength R-branch [101].

The number density, n, represents the number of molecules per m^3. This value is correlated to the molar concentration, c, and the mass density, ρ, through Avogadro's number, N_A, through the following relationships.

$$n = N_A c = \frac{N_A}{M}\rho$$

Meaning that an increase in molar concentration and density will increase the overall number density. Compared to a stoichiometric mixture, lean charges are expected to have higher concentrations of CO_2, lower concentrations H_2O, and minimal CO; rich charge conditions are expected to have lower concentrations of CO_2, high concentrations H_2O, and significant CO concentrations. Conditions seen with higher-peak pressures, as seen in pressure traces Figure 6-1 and Figure 6-2, tend to have higher densities leading to increases in number densities.

The bandwidth in these measurements is primarily attributed to collisional broadening and thermal broadening. Collisional broadening occurs when an emitting particle collides with another particle. This collision interrupts the emission process and broadens the spectral band. Collisional broadening is directly correlated to the pressure. Thermal broadening occurs due to relative velocities of emitting molecules which slightly modulates the measured wavelength. Molecules moving towards the measurement device are blue-shifted (shorter wavelength); molecules moving away from the measurement device are red-shifted (longer wavelength). Higher velocity molecules will cause greater thermal broadening, and the mean speed of all molecules is directly correlated to $\sqrt{T}$. However, broadening mechanics are controlled by specific constants for different molecules and the specific ro-vibrational transition.

Absorption of radiation is described by the absorption coefficient, α. Radiative absorption strength and broadening are controlled by the same mechanics as emission [50]. Within these experiments, absorption is relevant as emitted photons can be absorbed before exiting the combustion chamber, and self-absorption is the most likely source of absorption because molecules absorb at the same wavelengths that they emit. Therefore, H_2O and CO_2 are the strongest absorbers in these experiments, and as seen in previous chapters CO_2 is the primary absorber.

Absorption occurs when a molecule at a compatible low-energy state absorbs a photon at a specific energy. e.g. a high-temperature CO_2 molecule is formed due to a combustion reaction and emits a photon that is absorbed by a lower-energy CO_2 molecule. Radiative absorption is expected to be minimal early in combustion due to the low number densities of ground state absorptive molecules. Chapter 5 showed that absorbed energy (as a percentage of the total emitted energy) increases throughout the cycle because both the H_2O and CO_2 number densities increase during the combustion process. Finally, the cases with CO_2 dilution increase overall CO_2 number density, which contributes to strong CO_2 absorption. The absorption spectrum is determined by the thermo-chemical properties of the absorbing gas, which is important in cases with hot gases being absorbed by cool diluents.

Collisional quenching occurs when an excited state molecule collides with a quenching molecule and returns to a lower energy state through a non-radiative transition [102]. This quenching lowers the spectral strength because no photon is emitted from these quenched high-energy molecules. Like collisional broadening this adds a certain uncertainty to the spectrum. Collisional quenching occurrences grow with an increasing number of collisions, but the propensity of a molecule to quench is a molecular-energy specific property [102]. O_2 is known as a common quencher, therefore lean charge conditions could demonstrate a weaker measured signal [103]. However, even IR active molecules can quench an excited state molecule.

Independently, all of these effects can be predicted for a spectrum. However, all of these separate effects, and other higher-order effects, are convolved together to determine the measured spectra. The measured spectra contain the information to describe all of these separate influences, but without accurate data describing several of these properties, the information cannot be isolated. The following sections describe the different influences of the noted properties

6.3.3 Overview of Spectral Characteristics of all Measured Conditions

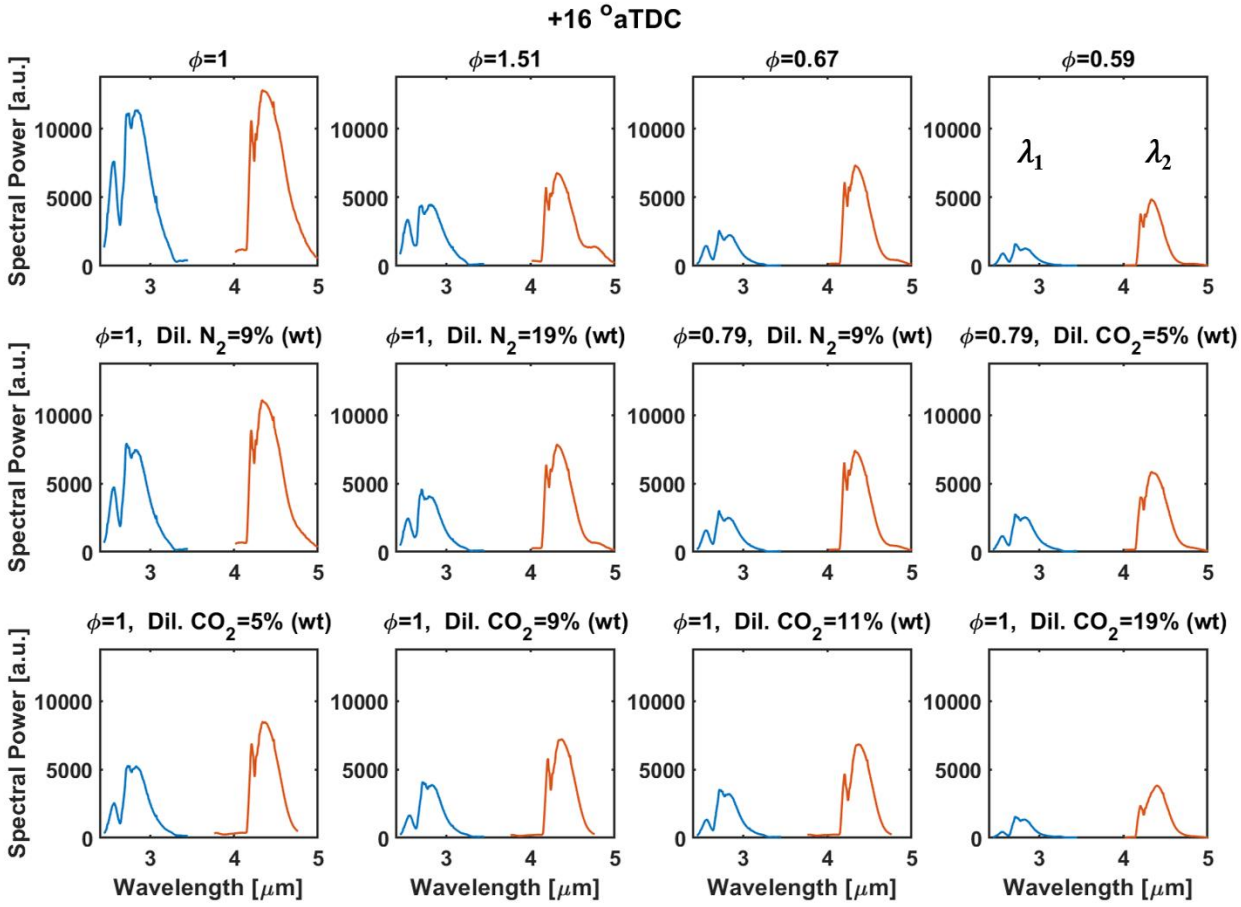

Figure 6-11: λ_1 and λ_2 emissions at +16 °aTDC for all measured conditions to provide a sense of spectral power magnitude. Top row, spectra for different equivalence ratios Middle row, spectra for N_2 dilution and lean/dilute measured conditions. Bottom row, spectra from CO_2 dilution measured conditions.

Figure 6-11 demonstrates the λ_1 and λ_2 emission spectrum of the twelve different measured conditions at +16 °aTDC. +16 °aTDC was chosen because it is close to the peak signal location for the φ=1 case, as seen in Figure 6-4. The ordinate is uniformly scaled across all plots so that the magnitude of radiative emissions of the different conditions is clear. The φ=1 case has the highest emissions at +16 °aTDC. The ratio of the peak λ_1 and peak λ_2 emission changes for the different

conditions due to molecular concentrations and the width of the λ_1 and λ_2 emission bands changes due to the pressure and temperature broadening.

Table 6-5 further explores the spectral magnitudes of the different measurement conditions. As expected, the undiluted φ=1 case had the highest total spectral power, and thus it was used as the reference case for comparison with all other conditions. Column three and four are calculated by summing the total spectral power over all the measured crank angles for the ensemble-averaged cycle producing a single value. Parenthetically next to the total signal is the percentage of the undiluted φ=1 case total signal. These columns give a quantitative value of total radiation in the measured volume at all measured conditions. Column five shows the ratio of the total λ_1 signal and the total λ_2 signal.

φ=0.59 has the lowest total signal, which makes sense given the high propensity of misfires with this condition. The lowest dilution cases – φ=1, N_2 dilution=9 % wt and φ=1, CO_2 dilution=5 % wt – have the highest total signal after the undiluted stoichiometric case. However, the CO_2 diluted case has a much lower λ_2 total signal due to the radiative absorption of the diluent. For all conditions, the λ_2 total signal outweighs the λ_1 total signal, but the φ=1 cases with CO_2 dilution demonstrate a higher ratio of λ_1 and λ_2, as seen in the fifth column. In fact, the ratios for the φ=1 cases with 5, 9, and 11% wt CO_2 dilution have higher ratios than the undiluted φ=1 case. This trend is due to the high CO_2 number density leading to reabsorption in the λ_2 feature.

Table 6-5: Total signal magnitudes and peak signal ratios for all measured conditions. Relative height compared to the stoichiometric, φ =1, case for reference.

Oxidizer	φ	Total λ_1 Signal / 10^7 (% of φ=1 case) [a.u.]	Total λ_2 Signal / 10^7 (% of φ=1 case) [a.u.]	Total λ_1 Signal/ Total λ_2 Signal [%]
Air	**0.59**	0.58 (16.3%)	01.63 (31.0%)	35.33
	0.67	1.04 (29.4%)	3.20 (60.6%)	32.44
	1.00	3.53 (100%)	5.27 (100%)	66.85
	1.51	1.71 (48.5%)	2.88 (54.6%)	59.37
Air + 9% N_2 (by mass)	**0.79**	1.28 (36.4%)	3.18 (60.3%)	40.29
	1.00	2.60 (73.9%)	4.76 (90.3%)	54.70
Air + 19% N_2 (by mass)	**1.00**	2.09 (59.4%)	3.88 (75.7%)	52.44
Air + 5% CO_2 (by mass)	**0.79**	1.55 (43.9%)	3.04 (57.7%)	50.93
	1.00	2.68 (76.1%)	3.82 (72.4%)	70.19
Air + 9% CO_2 (by mass)	**1.00**	2.45 (69.4%)	3.58 (67.8%)	68.37
Air + 11% CO_2 (by mass)	**1.00**	2.39 (67.8%)	3.38 (64.1%)	70.66
Air + 19% CO_2 (by mass)	**1.00**	1.12 (31.7%)	2.53 (47.9%)	44.30

Figure 6-12 expands on the information provided in the final column of Table 6-5 by presenting the ratios of total spectral power ratio from the λ_1 and λ_2 measurements from spark timing (-18 ^{o}aTDC) to +90 ^{o}aTDC. The undiluted φ=1 case is seen to peak right after the spark (-14 ^{o}aTDC), but all other conditions initially decrease before increasing towards a peak. This suggests that the early stoichiometric flame development produces H_2O faster than CO_2 in the

flame kernel, which agrees with the global 2-step reaction mechanism of propane and air [104]. This mechanism initially creates H_2O and CO, and the CO then reacts with O_2 to form CO_2 [105]. Also, fired simulations of the TCC-III engine operating stoichiometrically at 1300 rev/min demonstrated $\frac{dX_{H_2O}}{dt} > \frac{dX_{CO2}}{dt}$ from -20 to 0 ^{o}aTDC [personal communication with Dr. Angela Wu]. This trend is not seen in other conditions partially due to the reduced flame speeds which slows the flame kernel growth. The location of the peak ratio is seemingly connected to the flame burn speed. Increasing N_2 and CO_2 dilution can be seen to delay the peak location. The ratios changing throughout the cycle are connected to the species-specific spectral development, which is examined next. Lean equivalence ratio cases are seen to be CO_2 emission dominant across all presented crank angles, which aligns with predictions that lean flames have a high number density of CO_2 and low number density of H_2O.

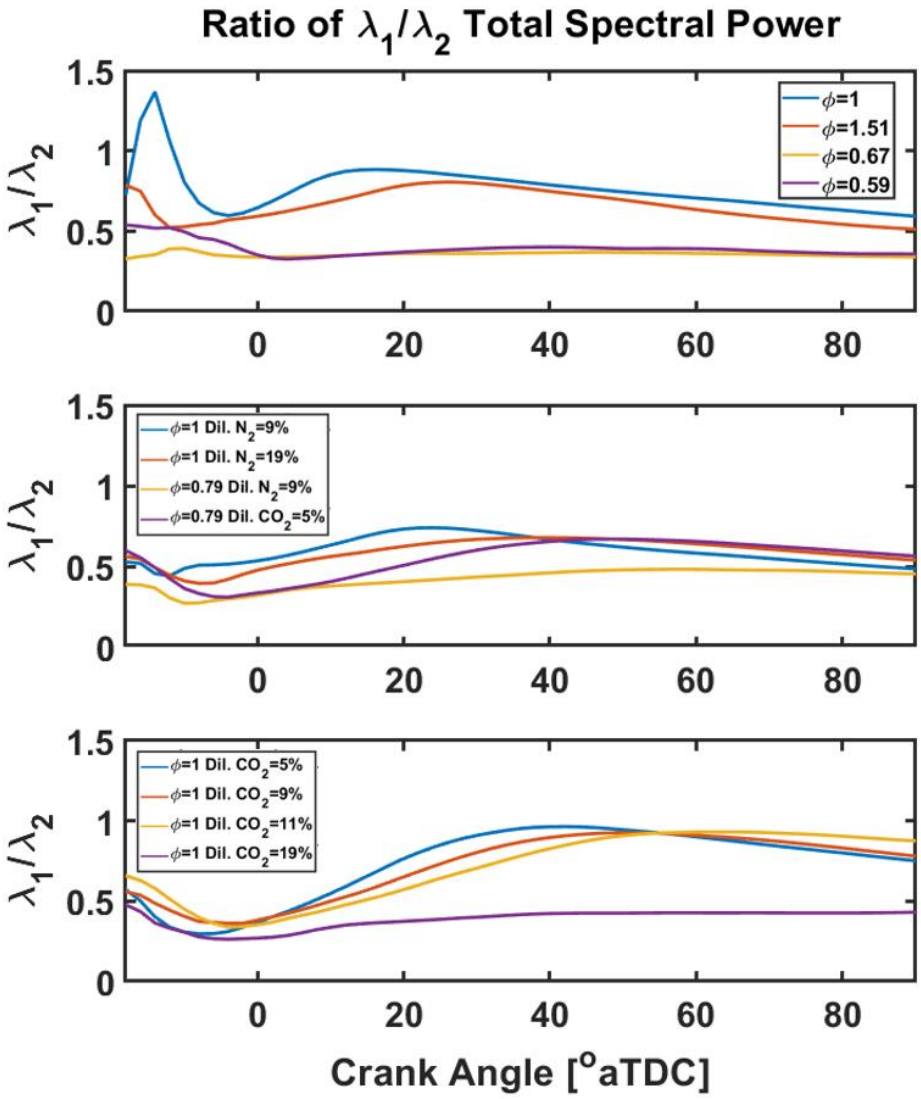

Figure 6-12: Ratio of the total spectral power of the λ_1 andλ_2 features at from spark time (-18 °aTDC) to +90 °aTDC. The changing ratio demonstrates overall changes in feature magnitude.

Figure 6-13 shows the crank-angle development of all the measured conditions against the total spectral power density, ρ_L. ρ_L corrects the total spectral power for the measured pathlength using the following relationship.

$$\rho_{\lambda,L} = \frac{I_{\lambda,CA}}{L_{CA}} \left[\frac{a.u.}{m}\right]$$

where I_{CA} is the spectral power at a specific crank angle and L_{CA} is the length from the piston top to the engine head surface in meters. The subscript λ_1 or λ_2 determines which wavelength region

is being presented. ρ_L represents the radiative heat rate per meter. This pathlength correction reduces the late-cycle emission seen in Figure 6-4 and Figure 6-5 because the pathlength has significantly increased. ρ_L produces a value of total spectral power per meter. The development of all the measured conditions is seen in this plot. As noted above in Figure 6-12, lean conditions have strong CO_2 emission. Inversely, the φ=1.51 is expected to have more H_2O and CO due to the abundance of fuel. The resulting spectral densities of φ=1.51 and φ=0.67 have different λ_1 emissions but similar magnitude λ_2 emissions.

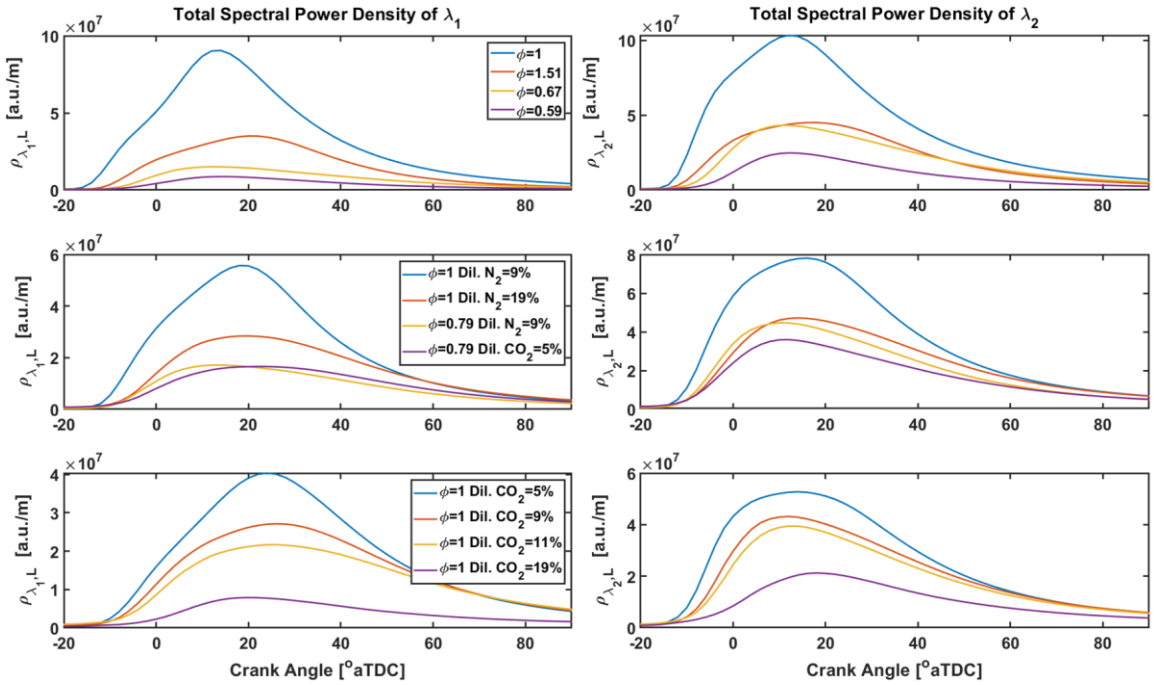

Figure 6-13: Left column, Total λ_1 spectral power density development for different measured conditions. Right column, Total λ_2 spectral power density development for different measured conditions. Conditions described in left column legends.

A comparison of the lean and dilute cases – φ=0.79, N_2 dilution=9 % wt and φ=0.79, CO_2 dilution=5 % wt – in the second row shows the influence of CO_2 absorption, which noticeably reduces the λ_2 spectral density for the CO_2 diluted case. The combination of a lean equivalence ratio, which results in CO_2 dominant emission, and CO_2 dilution, which reduces the CO_2 emissions, is explored further in Section 6.3.4.

The φ=1 case demonstrates the interesting features described previously. $\rho_{\lambda_1,L}$ can be seen to increase monotonically from spark timing to ~16 ^{o}aTDC (near CA_{90}), but the slope changes throughout the flame burn period. $\rho_{\lambda_2,L}$ also increases monotonically from spark timing to ~16 ^{o}aTDC (near CA_{90}), but the slope significantly decreases around TDC. This decrease in slope was attributed to the radiative absorption of the CO_2 feature. The derivative of spectral power density with respect to the crank angle was calculated to explore the second derivate of radiative heat loss and to examine the changing slopes.

Figure 6-14 shows $\frac{d\rho_L}{dCA}$ for both λ_1 and λ_2 for all measured conditions. It is clear that $\frac{d\rho_{\lambda_1,L}}{dCA}$ demonstrates a two-peak behavior for most conditions. $\frac{d\rho_{\lambda_2,L}}{dCA}$ also shows a two-peak behavior, but for all cases the first peak is stronger. These two-peak curves suggest a bimodal radiative development for both H_2O and CO_2 during the flame growth period. However, the influence of the measurement volume could explain this trend. Early flame kernel growth within the measurement volume is well captured, but the horizontal expansion of the flame towards the liner is poorly captured. Previous measurements of IR emissions from 1.3-2.5 μm through the fused silica cylinder liner do not present this type of spectral development. This trend demonstrates a shortcoming of measurements through the Bowditch piston, and suggest that measurements collecting the total in-cylinder emission could explain the global development of radiation.

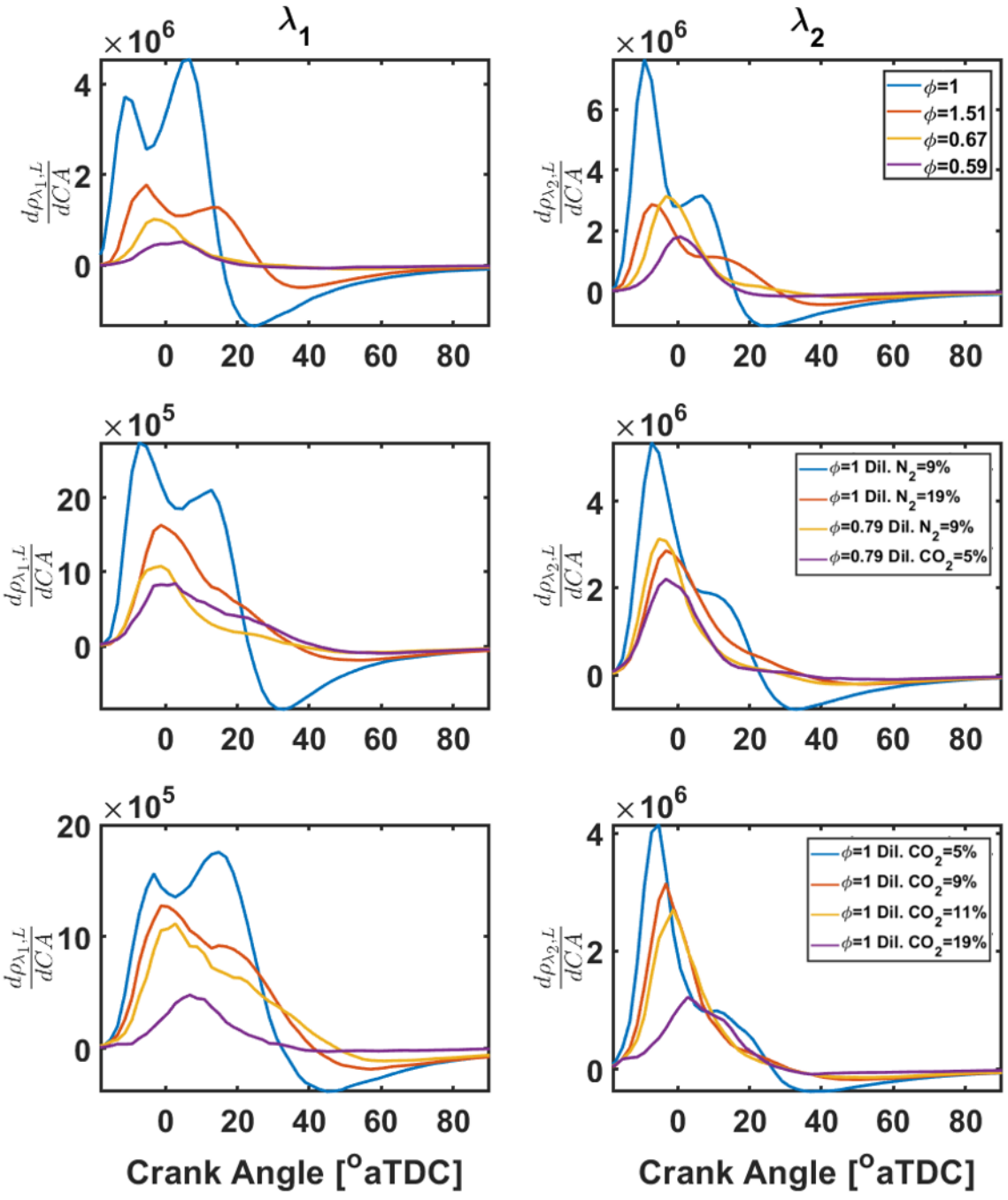

Figure 6-14: Derivative of the total spectral power density of the λ_1 and λ_2 measurement with respect to the crank angle for all measured conditions.

6.3.4 Influence of Equivalence Ratio

As in Chapter 5, the following plots examine the emission spectrum at four crank angles: -8, +8, +16, and +150 °aTDC. These are chosen to examine the early flame, peak flame, and flame

extinction periods. Figure 6-15 shows the normalized spectral power (Norm. Spec. P.) of the ensemble-averaged cycle for four different equivalence ratios. λ_1 is normalized by the peak spectral power from 2.7-3.0 µm; λ_2 is normalized by the peak spectral power from 4.3-4.5 µm. These spectra are normalized to accentuate relative spectral differences; however, the presented spectra can have signal that is orders of magnitude different.

The λ_1 spectra at -8 ^{o}aTDC show relevant emission at 3.2-3.4 µm due to the C-H bond of unburned propane, highlighted in Figure 6-15. The relative intensity of the C-H feature is a maximum for the φ=0.59 spectrum, which has the lowest expected laminar flame speed therefore it is likely that the flame kernel has not reached the boundaries of the measurement volume [98]. This slow flame means significant unburned propane remains at -8 ^{o}aTDC. The φ=0.67 spectrum also has significant C-H emission in the early flame for the same reasons. It is important to note that the φ=1 spectrum could have C-H emission that is eclipsed by the H_2O and CO_2 radiation which is broadened to 3.3 µm. Finally, the rich case has strong overall λ_1 emissions, which partially obscures the C-H emission in the relative spectrum. However, the φ=1.51 spectrum produces the strongest absolute C-H emissions due to the abundance of fuel and slow flame speed. The absolute spectral power of the C-H bond in the rich case is about two times larger than the absolute spectral power of the leanest case.

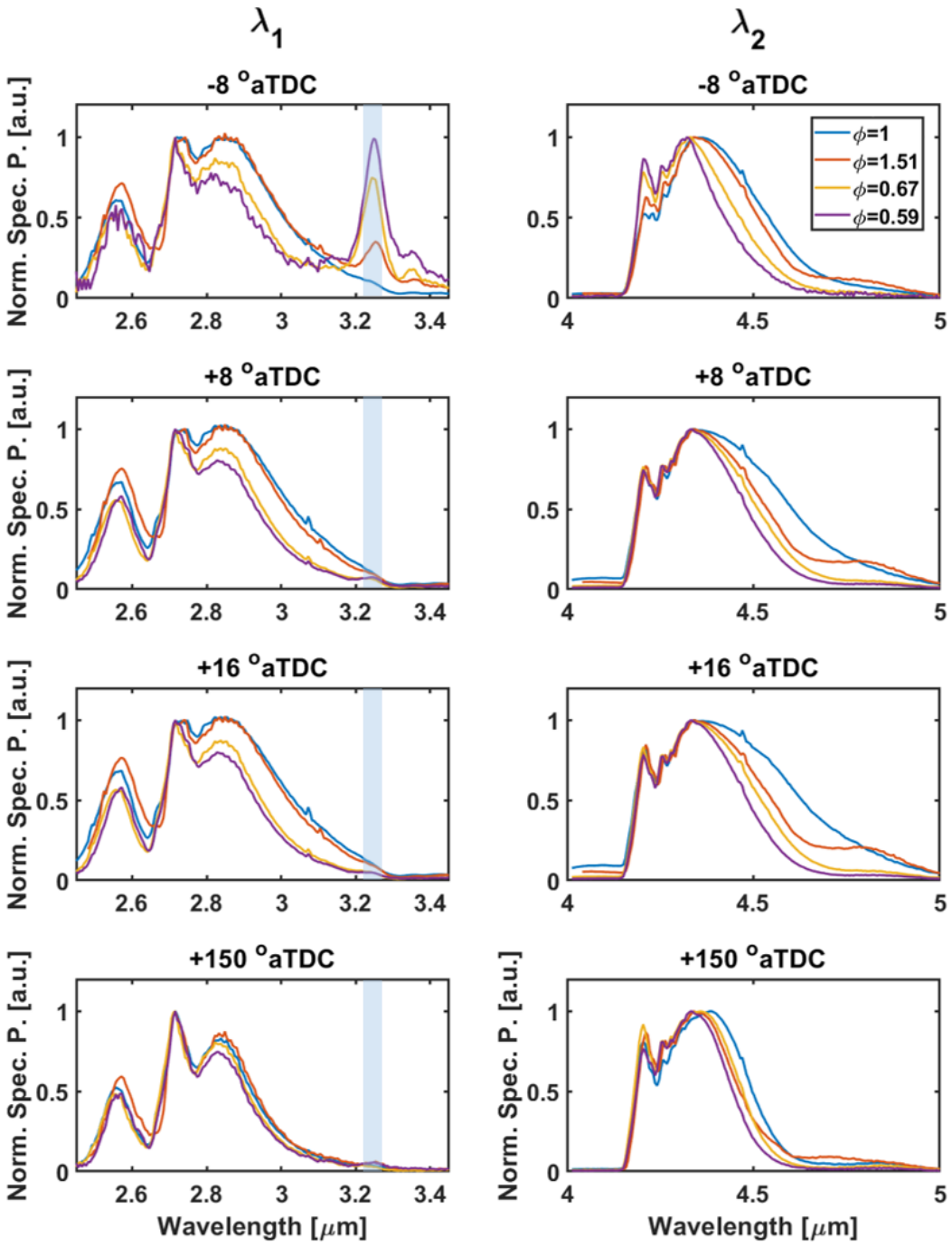

Figure 6-15: λ_1 and λ_2 emission spectrum for φ=1, 1.51, 0.67, and 0.59 at four different crank angles. C-H bond, highlighted in λ_1, at ~3.3 µm seen early in the cycle, CO vibration at ~4.9 µm seen late in the cycle.

The λ_2 spectrum contains both CO_2 and CO emission. CO is a diatomic molecule and has its fundamental ro-vibrational band centered at 4.66 µm and its P-band from 4.66-5.1 µm. The rich condition has the most CO due to excessive fuel and limited oxidizer, and the rich λ_2 spectrum

shows the strongest relative emission from 4.6-5.0 μm at all measured crank angles. The lean cases show low relative emission from 4.6-5.0 μm at all presented crank angles due to low amounts of CO. The stoichiometric case has strong emission from 4.6-5.0 μm at +8 and +16 ^{o}aTDC, but the majority of this signal is likely due to the broadened CO_2 feature. At +150 ^{o}aTDC, the stoichiometric case has relatively low emission as the stoichiometric condition is expected to produce low amounts of CO.

In the λ_1 and λ_2 spectra, the width of the spectral feature is connected to the pressure and temperature through the broadening mechanics. Since both properties change simultaneously, it is challenging to separate the influence of temperature and pressure. The λ_2 spectra show a clear increase in width for increasing pressure. The stoichiometric case increases in width until reaching a maximum at +16 ^{o}aTDC where the maximum pressure occurs. The bandwidth increases primarily on the long-wavelength (right side) of the spectrum, and the peak spectral location shifts in the same direction with increasing absolute spectral power. As noted previously, the short wavelength region of the CO_2 region has a strong band head, which counteracts broadening on the short wavelength side. However, the higher temperature regions would have higher populations of the rotational transitions occurring at short wavelengths, but strong radiation at shorter wavelengths is not pronounced in this plot. The width of the λ_1 feature follows a similar trend for high pressures and temperatures, but in λ_1, the rich case has similar width as the stoichiometric case while having lower pressure and temperature at -8, +8, and +16 ^{o}aTDC. The bandwidth trend is explored further in Figure 6-16.

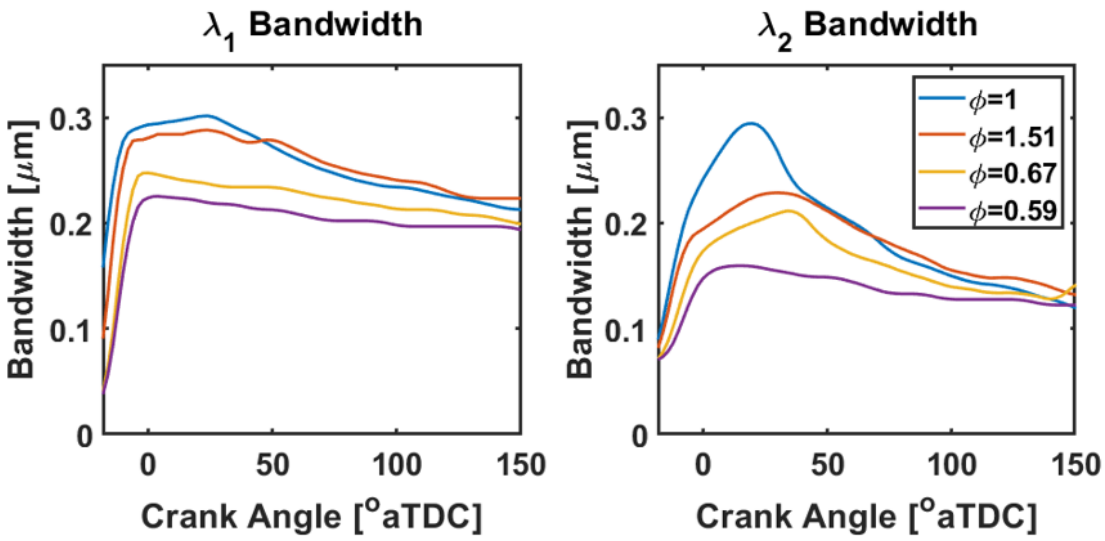

Figure 6-16: Bandwidths for φ=1, 1.51, 0.67, and 0.59 from spark timing (-18 °aTDC) to +150 °aTDC.

Figure 6-16 demonstrates the λ_1 and λ_2 bandwidths from the spark timing to +150 °aTDC. The bandwidths are calculated as the width from the location of the maximum signal to the location of 50% signal in the longer wavelength direction. This value was chosen because the shorter wavelength width remains mostly constant in the λ_2 plots. The increase in bandwidth can be attributed to collisional broadening ($\propto$ P) and Doppler broadening ($\propto \sqrt{T}$). Both plots show the stoichiometric case having the highest bandwidth from the spark until ~50 °aTDC. The λ_2 bandwidth plot shows much higher variations in bandwidth size for increasing temperature and pressure, demonstrating that the CO_2 υ_3 band is more sensitive to total broadening mechanics. The λ_1 bandwidth plot shows that the rich and stoichiometric bandwidths are similar. This similar bandwidth is consistent with theoretical expectations: the rich case has a higher concentration of H_2O increasing long-wavelength signal, the stoichiometric case reaches higher peak T and P enhancing broadening mechanisms.

6.3.5 Influence of Dilution

This section explores the influence of charge dilution on the molecular radiative heat loss. Firstly, the following section explores the impact of the N_2 dilution (9% and 19% wt), the impact of CO_2 dilution (5%, 9%, 11%, and 19%), and the combination of a lean equivalence ratio and dilution (5% N_2 and 9% CO_2) is presented.

Nitrogen Dilution

The addition of N_2 is meant to reduce the flame temperature and reduce the flame speed, but since N_2 is IR-inactive, it does not interfere with the radiative emissions within the combustion chamber. The following plot examines the emission spectrum at four crank angles: -8, +8, +16, and +150 ^{o}aTDC. Figure 6-17 shows the normalized spectral power (Norm. Spec. P.) of the ensemble-averaged cycle for the different φ=1 with and without added N_2 dilution. As previously, λ_1 is normalized by the peak spectral power from 2.7-3.0 μm; λ_2 is normalized by the peak spectral power from 4.3-4.5 μm.

Figure 6-17 demonstrates similar characteristics as Figure 6-15. Particularly, the bandwidth of the λ_2 spectrum increases for the higher pressure and temperature condition; the widest feature is the undiluted φ =1 case and the narrowest is the 19% dilution case. The C-H bond is clearly seen in the -8 ^{o}aTDC λ_1 spectrum. A trend not yet explored is the relative height of the 4.25 μm peak, highlighted in orange in the plot. This feature increases throughout the cycle for all presented crank angles. At -8 aTDC, the 9% dilution case closely matches the value of the stoichiometric case. In Figure 6-15, the 4.25 μm peak is highest for lean cases. The similarities of the 4.25 μm peak at -8 ^{o}aTDC in the undiluted and φ=1 with 9% N_2 dilution cases suggest that there is a connection in the early flame development and the total radiative heat loss. These two conditions have the strongest λ_2 total spectral magnitudes, and this relatively low 4.25 μm peak could be due to the

early development of CO_2 and subsequent reabsorption at -8 ^{o}aTDC. Early flame absorption is further identified in CO_2 dilution cases.

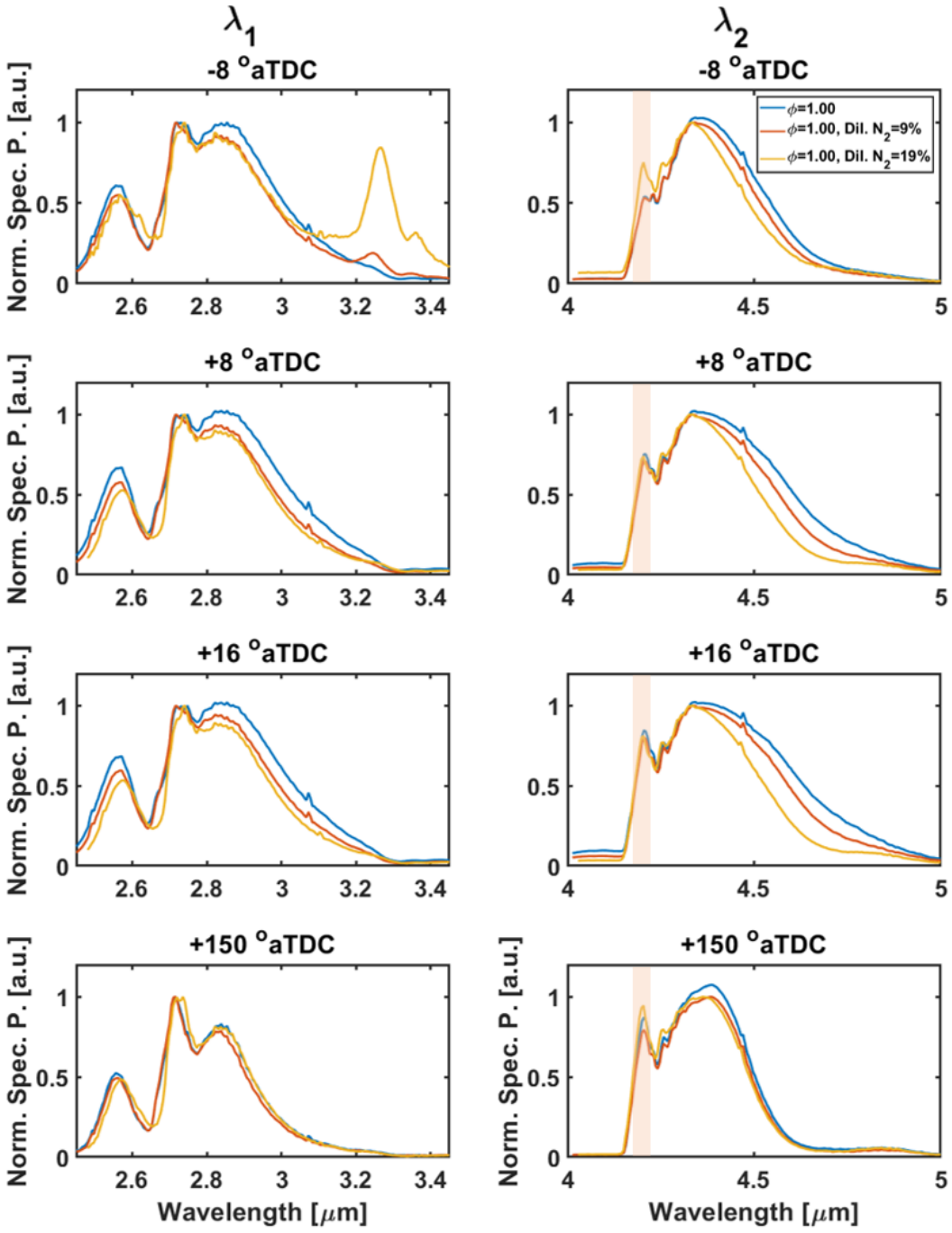

Figure 6-17: λ_1 and λ_2 emission spectrum for φ=1 undiluted, φ=1 N_2 dilution= 9 [%wt.], φ=1 N_2 dilution= 19 [%wt.] at four different crank angles. 4.25 μm peak highlighted to demonstrate the increasing value at different crank angles.

Carbon Dioxide Dilution

The addition of CO_2 reduces the flame temperature and the flame speed while increasing the number density of CO_2 in the measurement volume. CO_2 is a strong IR absorber, and the influence of this absorption has been previously noted in this dissertation and previous simulations [14]. The following plot examines the emission spectrum at four crank angles: -8, +8, +16, and +150 ^{o}aTDC. Figure 6-18 shows the normalized spectral power (Norm. Spec. P.) of the ensemble-averaged cycle for the different φ=1 with added CO_2 dilution.

Figure 6-18 demonstrates unique characteristics not seen in the previous spectra. The -8 ^{o}aTDC λ_2 spectral peak locations have shifted towards longer wavelengths and the overall spectral shape has changed. This is due to radiative trapping in the unburned gas region. Diluents in the unburned region away from the flame kernel will remain at a relatively low temperature during the early combustion period (see Figure 6-8 for the image of the flame kernel at -10 and -6 ^{o}aTDC). Therefore, CO_2 emissions from the flame and burnt gas region are strongly absorbed by the lower temperature CO_2 diluent. The absorbing CO_2 absorbs radiation predominantly in the shorter wavelengths due to its low temperature. This explains the spectral shape seen at -8 ^{o}aTDC for all four CO_2 dilutions. The highest dilution case (19% CO_2) can be seen to have a different spectral shape at -8, +8, and +16 ^{o}aTDC due to the low temperature, low pressure, and extremely high CO_2 concentration of this condition. These spectral changes highlight the connection between the number density of CO_2 concentration, CO_2 absorption, and the spectral shape.

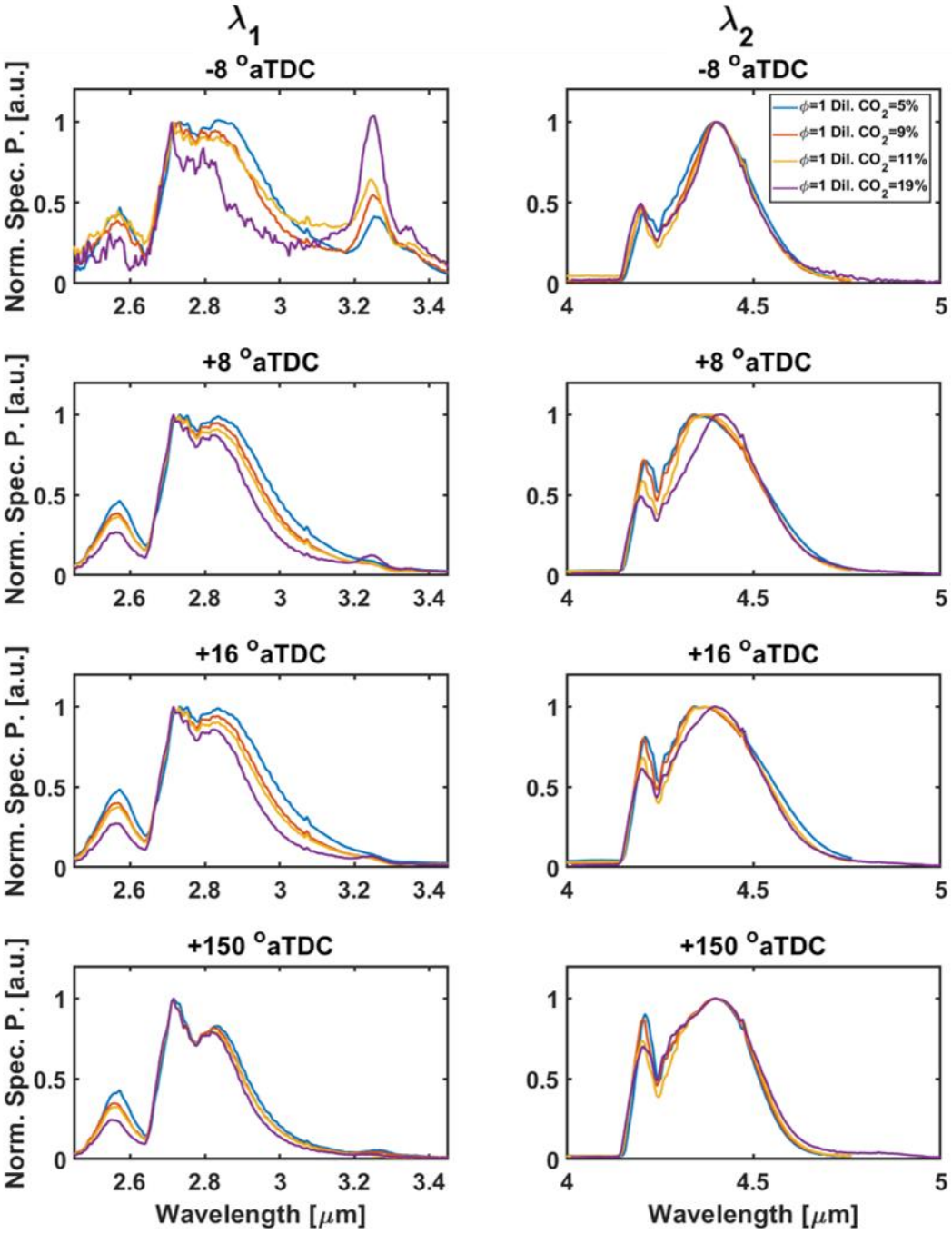

Figure 6-18: λ_1 and λ_2 emission spectrum for φ=1 CO_2 dilution= 5 [%wt.], φ=1 CO_2 dilution= 9 [%wt.], φ=1 CO_2 dilution= 11 [%wt.], φ=1 CO_2 dilution= 19 [%wt.] at four different crank angles. Relative height of ~4.25 μm peak decreases with increasing CO_2 dilution.

Another noticeable difference is the reduced sensitivity of λ_2 bandwidth to increased pressure and temperature. At +16 °aTDC, the least diluted case (5% dilution) demonstrates a slightly increased λ_2 bandwidth on the longer wavelengths, but this case has a higher pressure than

in the other cases. At +8 and +16 ^{o}aTDC the peak location of λ_2 emission shifts to longer wavelengths for additional dilution, which effectively increases the bandwidth for decreasing CO_2 dilution. The λ_1 spectrum remains sensitive to increases in pressure and temperature.

Lean and Dilute Cases

The final set of conditions are lean and dilute cases. Two lean and dilute cases are presented: φ=0.79 with 9% wt. N_2 dilution and φ=0.79 with 5% wt. CO_2 dilution. Lean and dilute operation is used in advanced engine configurations to increase efficiency and reduce pollutant formation, but this pushes engine operation towards the limits of stable combustion. These conditions have low-temperature flames, slow flame speeds, and excessive oxidizer. The measurements from the lean and CO_2 dilute conditions are close to replicating the radiative impact of EGR. The following plot examines the emission spectrum at four crank angles: -8, +8, +16, and +150 ^{o}aTDC. These two conditions were designed to have similar flame temperatures and were seen to have comparable pressures in the bottom plot of Figure 6-2. The N_2 diluted case had higher pressure at all presented crank angles, which leads to higher temperatures. The pressure differences at the different crank angles, ΔP_{CA}, are as follows: $\Delta P_{-8\ ^{\circ}aTDC}$=66 kPa, $\Delta P_{+8\ ^{\circ}aTDC}$ =78 kPa, $\Delta P_{+16\ ^{\circ}aTDC}$ =71 kPa, and $\Delta P_{+150\ ^{\circ}aTDC}$ =1 kPa. These pressure differences amount to ~8.5% change in pressure at -8, +8, and +16 ^{o}aTDC (<1% at +150 ^{o}aTDC), and emphasize that the temperatures and pressure are close between both conditions. Therefore, the spectral differences can be attributed principally to species number density and radiative trapping. Figure 6-19 is not normalized by peak emission to highlight these differences.

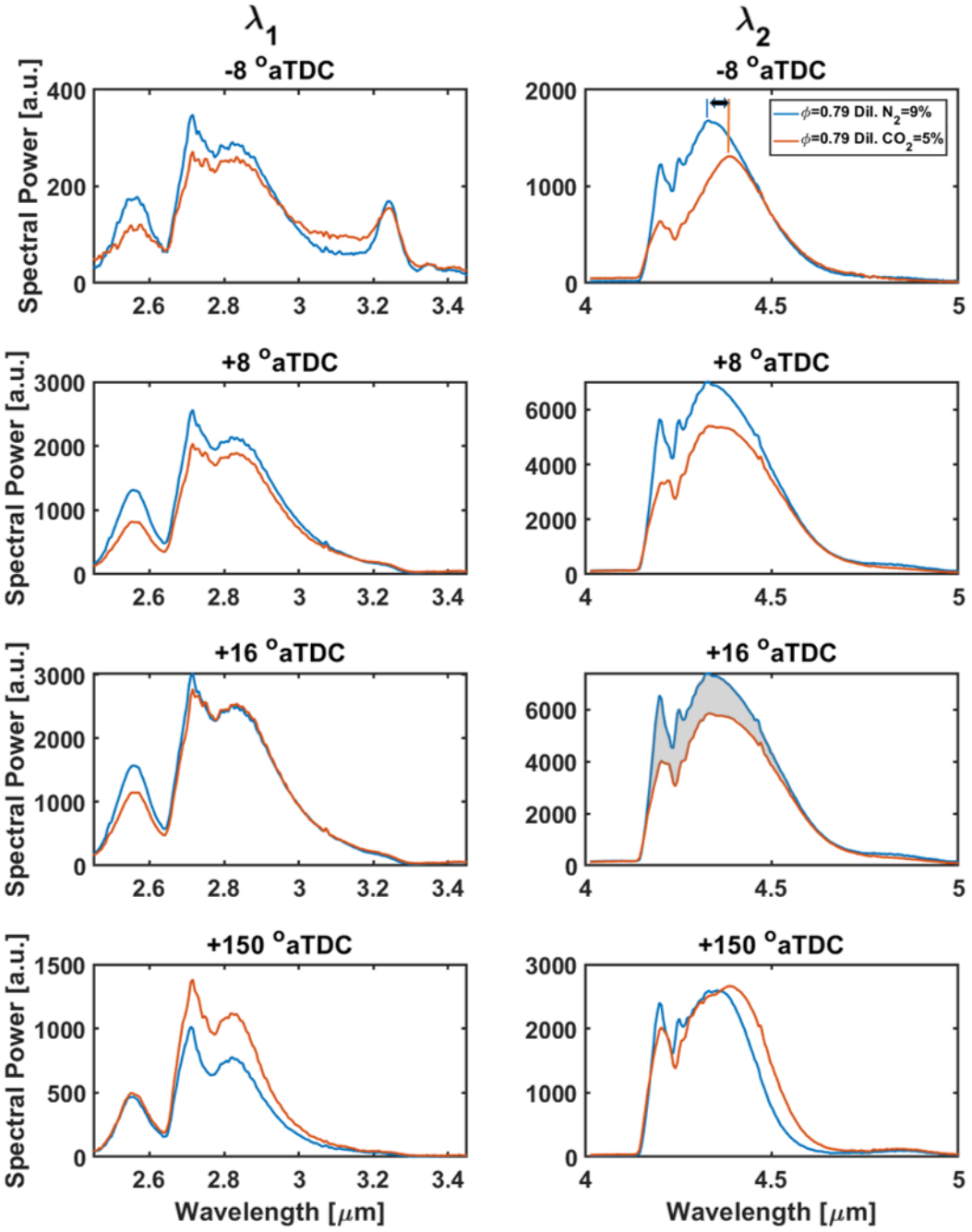

Figure 6-19: λ_1 and λ_2 emission spectrum for φ=0.79 N_2 dilution= 9 [%wt.], φ=0.79 CO_2 dilution= 5 [%wt.] at four different crank angles. λ_2 peak location changes with the addition of CO_2 dilution.

The lean and N_2 dilute case has CO_2 dominant emissions, with total λ_2 emission being 2.5 times total λ_1 emission; the lean and CO_2 diluted condition is also CO_2 dominant, with total λ_2 emission being 2 times total λ_1 emission. The lean and CO_2 diluted condition has a high CO_2 concentration from the diluent gas, leading to high CO_2 absorption early in the cycle and higher

overall CO_2 emission later in the cycle. Figure 6-19 further confirms the strong influence of CO_2 dilution on radiative heat loss and provides key insights into the combination of lean equivalence ratios and CO_2 dilution.

As highlighted in the -8 ^{o}aTDC λ_2 plot, the φ=0.79, 5% CO_2 case has a spectral peak ~50 nm away from the 9% N_2 diluted case. The -8 ^{o}aTDC λ_2 spectra clearly show the previously described spectral peak shift due to CO_2 self-absorption and reinforce the claim that early flame absorption occurs at shorter wavelengths. The differences between the two λ_2 spectra, $\Delta\lambda_2$, (shown shaded at +16 ^{o}aTDC in Figure 6-19) can be used as a proxy for the absorption due to CO_2 diluent. $\Delta\lambda_2$ shifts to longer wavelengths at later crank angles. At +150 ^{o}aTDC, the CO_2 diluted case emits strongly at longer wavelengths, suggesting that the latent heat absorbed by CO_2 throughout the cycle is re-emitted later in the cycle. $\Delta\lambda_1$ shows agreement during the flame growth period at +8 and +16 ^{o}aTDC. At +150 ^{o}aTDC, the CO_2 diluted case has stronger λ_1 emission.

6.4 Summary

This chapter contained an extensive analysis of the 12 different measured conditions in the TCC-III engine. Through this analysis, strong correlations between the radiative emissions and the engine pressure dynamics were demonstrated. Pressure correlations for the measurements of different equivalence ratios were highlighted, but data describing correlations at all measured conditions is included in Appendix A. The Pearson correlation coefficients, R, were weaker for λ_2 due to the influence of CO_2 reabsorption in that wavelength band. Strong relationships were seen between the spectral power and the IMEP, peak pressure, average pressure, and total heat release.

A combination of broadband spectral measurements demonstrated the largest spectral range of emission measurements yet recorded in an engine. The stoichiometric spectrum from 1.5-5 μm highlighted all the relevant molecular ro-vibrational features that contribute to radiative heat

loss within that band. The two largest spectral features are due primarily to the fundamental vibrations of H_2O and CO_2; H_2O's υ_1 and υ_3 vibrations contained in λ_1 and CO_2's υ_3 vibration contained in λ_2. These two wavelength regions have been the subject of previous modeling studies, and contain a majority of the total molecular radiative heat loss [35].

The magnitude of radiative emissions varied significantly for different conditions. From all the measured conditions the stoichiometric and undiluted condition showed the strongest emissions, and the 5% CO_2 and 9% N_2 diluted cases showed the second strongest emissions. All cases with CO_2 dilution demonstrated lower λ_2 emissions due to CO_2 self-absorption. The crank-angle development of all spectra was examined to further determine the influence of the conditions. Early development of the flame kernel for the stoichiometric condition demonstrated strong H_2O radiation in alignment with the expected chemical kinetics and TCC-III engine simulations. The spectral power density demonstrated undulating spectral emissions in both λ_1 and λ_2 regions during an engine cycle, but these results could be significantly influenced by the measurement volume location.

The relative spectra from the different measurement conditions were examined. These spectra are in strong qualitative agreement with theoretical spectral expectations. The temperature, pressure, species number density, and radiative trapping influenced the measured spectra. Spectra at -8 °aTDC often showed the emission of the C-H bond due to unburned propane, and conditions where not all fuel was burnt included C-H signal at late in the cycle. Therefore, the 3.3 μm C-H region could be utilized to monitor partial-burns and misfires. The φ=1.51 condition demonstrated noticeable emissions from CO fundamental vibration in the λ_2 region. The collisional and thermal bandwidth broadening was seen prominently in the λ_2 region; however, the sensitivity of this broadening changed in CO_2 diluted cases. Additionally, CO_2 diluted cases had altered spectral

shapes and spectral peak locations due to high CO_2 number density absorbing short-wavelength radiation. CO_2 diluted cases saw significant radiative trapping. This trapping lowers the radiative heat loss to the walls but raises the local temperatures within the combustion chamber. From the lean and dilute cases, it was hypothesized that the λ_2 region re-emits radiation late in the cycle. All of the presented trends within this chapter suggest that the broadband measurements of radiative emission have the potential to provide quantitative insight into the in-cylinder thermochemical properties. However, these measured spectral trends result as a convolution of many spectral characteristics. Further quantitative data is needed to isolate a single property.

Finally, this chapter provided insight into the expected behavior of radiative heat transfer for different engine conditions, and allowed for the formulation of a conceptual understanding of molecular radiation for varied conditions. The conclusions are as follows.

- **φ = 1 without dilution:** This reference condition showed the strongest measured radiative heat loss. In Chapter 5, measurements suggested that over 50% of CO_2 emissions are reabsorbed. The amount of radiative trapping will increase significantly for higher-pressure engines where number densities and temperatures are higher.
- **φ < 1 without dilution:** For these conditions, CO_2 dominant and low H_2O radiative heat loss and high radiative variability were observed relative to stoichiometric conditions. Strong CO_2 radiation is likely to enhance local condition changes, but early flame emissions are less likely to be trapped due to low CO_2 number density early in the cycle.
- **φ > 1 without dilution:** For these conditions, significant CO radiation and C-H radiation were recorded, but radiation is predominantly H_2O controlled. In Chapter 5, up to 15% of H_2O emission was reabsorbed, so radiative trapping is not as significant as CO_2 dominant conditions. Rich conditions are rarely used as a global equivalence ratio; however, the φ=1.51

rich measurements could provide a sense of expected radiative behavior for locally high-φ flames from direct injection and stratified charge combustion.

- **φ = 1 with N_2 dilution:** N_2 dilution showed low-temperature stoichiometric behavior, and followed similar trends. The lightly diluted condition showed strong measured radiative heat loss.
- **φ = 1 with CO_2 dilution:** Early flame radiation was strongly absorbed by the diluent. The temperature changes at the location of diluent could be significant for high-pressure, highly-diluted combustion schemes, such as HCCI. Trapped radiation may be released later in the cycle, but this will have little impact on the local conditions.
- **φ < 1 with CO_2 dilution:** Similar to φ=1 with CO_2 dilution, lean and dilute conditions would similarly enhance early radiative trapping. The lean condition has strong CO_2 number density so it would further accentuate CO_2 absorption and local conditions. This condition serves as a proxy for EGR-diluted engine charges, but the impacts of H_2O trapping were not explored. This condition is likely to have the strongest local conditions change and deserves further study.

Chapter 7 Conclusions and Future Work

7.1 Conclusions

Climate change due to manmade greenhouse gas (GHG) emissions has drawn worldwide attention as the defining issue of the century. Improving the efficiency of the transportation sector is important in the fight against climate change, and advanced engine research provides needed pathways to improving engine efficiency. This includes a continued focus on in-cylinder engine heat transfer and re-evaluating the influence of radiative heat transfer. This dissertation sought to characterize molecular radiation in a spark-ignited engine for a variety of conditions to provide needed experimental insight into this complex phenomenon.

A detailed investigation of radiative heat transfer was performed on a flat-flame Hencken burner and the spark-ignited TCC-III engine. These measurements were performed using an IR spectral measurement technique developed to achieve high-repetition rates and large spectral ranges. Spectral emission measurements were recorded for twelve different conditions of the propane-air fueled engine and sixteen different conditions of the methane-air fueled flat-flame burner. Concurrent simulations using the photon Monte Carlo line-by-line method, performed at Pennsylvania State University by Dr. Daniel Haworth and his laboratory, allowed the influence of radiative trapping and radiative heat losses to be better understood. Measured and simulated spectral comparisons permitted the preliminary validation studies of the numerical technique. The main conclusions of this body of work are as follows.

An accurate, high-speed, and broadband spectral measurement technique for infrared molecular radiative emissions was developed. Previously, limited work had been performed to capture broadband, spectrally resolved, infrared emissions measurements in a reciprocating engine. Adequate measurement capabilities were achieved using a high-speed IR camera coupled with a dispersive grating spectrometer. The TCC-III engine with a modified sapphire piston window provided optical access to the relevant wavelength region. This measurement technique provided the first comprehensive dataset of crank-angle resolved broadband measurements of the IR molecular gas emissions from 1.5-5.0 μm.

The presented measurements allowed for assessments and improvements of the photon Monte Carlo line-by-line method. The initial validation of the PMC-LBL method was achieved. Simulations performed at Pennsylvania State University with the participation of Dr. Daniel Haworth, Dr. Sebastian Ferreyro Fernandez, and Samuel Kazmouz provided spectrally resolved simulations of IR emissions from the flat-flame burner and TCC-III engine. The simulated and measured spectra of the flat-flame burner operating at φ=1 were compared in Chapter 4, and a strong agreement was seen across the entire measured wavelength range, 1.5-5.5 μm. Small disagreement in the spectra was seen due to the different spectral resolutions and unresolved contributions of atmospheric absorption in the measurements. In Chapter 5, comparisons were made for simulations and measurements from the TCC-III engine operating at φ=1. A strong agreement in the measured and simulated spectra of the wall radiation from 2.4-3.4 μm ($\lambda_1$region) was demonstrated when simulating the measured volume. The agreement was seen at various crank angles and several different individual cycles. These validation studies demonstrate that the PMC-LBL method is an accurate model of the radiative heat loss for atmospheric and high-

pressure combustion environments, but further validation of the 4-5 μm ($\lambda_2$region) region is still needed.

The radiative emissions of molecular gases (CO_2, H_2O, CO, and hydrocarbons) were characterized at a variety of flat-flame and optical engine conditions. Within the flat-flame burner, calculations of the participating species number densities were closely tied to the measured signals. Measurements from the flat-flame burner showed that increasing the equivalence ratio showed decreasing spectral power; N_2 dilution decreased the flame temperature and lowered the overall spectral power; and the species-specific contributions of H_2O, and CO_2, CO were isolated through spectral ratios. Spectral measurements from the TCC-III engine changed significantly in both the spectral and temporal dimensions based on conditions. The measured spectral dataset demonstrated strong correlations to the engine pressure dynamics, especially in stable combustion conditions. Changes in equivalence ratio, N_2 dilution, CO_2 dilution were directly connected to the emitted spectral characteristics. Lean operation lowers the in-cylinder temperatures and pressures which results in a weaker spectral signal, but lean operation demonstrated higher relative CO_2 radiation due to an abundance of oxidizer. Rich operation also lowers spectral magnitude, and the lack of oxidizer causes appreciable CO and unburned fuel (C-H bond) radiation. N_2 diluted cases have reduced spectral intensity due to reduced temperature. CO_2 diluted cases exhibit altered spectral shapes and spectral peak locations due to significant CO_2 radiative trapping. This trapping lowers the radiative heat loss to the walls but lead to the local temperature changes within the combustion chamber. Finally, the noted experimental trends were discussed in the context of their implications on engine behavior.

7.2 Future Work

Through the course of this work, several opportunities for further investigation of radiative heat transfer in combustion systems were identified. Infrared imaging measurements of radiative emissions could provide unique information about the spatial component of molecular radiation. During engine combustion, the majority of the gas is compressed into the boundary layer, and simulations have shown that a majority of radiative reabsorption occurs in these areas. Additionally, the boundary layer controls the magnitude of convective heat flux. The ability to study the spatial development of H_2O and CO_2 radiative emissions could further determine the impacts on total heat loss, and allow for measurement of local condition changes. Performing synchronous spectral and spatial measurements would provide a wealth of information in the overlap of spatial and spectral dimensions.

Further studies comparing measurements and PMC-LBL simulations for combustion systems would allow complete validation of the method. The dataset of flat-flame burner measurements operating at varied conditions provides a range of conditions for continued validation of atmospheric flame radiation. Hencken burner flame simulations would need to be corrected for the measurement volume, which has not been experimentally quantified. The flat-flame burner remains useful to validate as it removes the complications of dynamic pressures and temperatures.

A strong agreement in the measured and simulated spectra of the wall radiation from 2.45-3.45 μm (λ_1 region) was demonstrated when simulating the measured volume for the engine experiments. However, disagreement in the 4-5 μm region (λ_2) showed under prediction of CO_2 self-absorption. Further analysis of the treatment of the spark plug boundary and the measured volume location sensitivity is currently underway. Once completed, validation of the PMC-LBL

method across all measured wavelengths for the stoichiometric condition can occur. Additionally, the measured dataset of TCC-III measurements provide a range of conditions for further validation of high-pressure molecular radiation. The successful validation of the photon Monte Carlo method will facilitate the development of simplified radiative transfer models that can be efficiently coupled CFD simulations. Simplified radiative transfer models would permit efficient consideration of molecular radiation in many different combustion environments. Also, the measurement volume is well suited for the usage of a reverse Monte-Carlo (RMC) method where photons are traced in a time-reversal process from a small area of interest, in this case the measured wall patch.

Finally, there is promise that the broadband measurements of radiative emission will provide quantitative insight into the in-cylinder thermochemical properties. This work has identified strong correlations and trends between the radiative emissions and the in-cylinder pressure, temperature, burn characteristics, species number densities, and radiative trapping. However, these spectral trends result as a convolution of several of these conditions and have yet to be isolated. It is possible to extract single conditions accurately with additional analysis of the spectral measurements, calibration of the experimental apparatus to an absolute unit, and a parametric study using an accurate spectral emissions model (such as the PMC-LBL). With access to expected temperatures, pressures, and concentrations it would be possible to determine expected flame emission, and to determine the amount of radiative absorption occurring.

Appendix A: Pressure Correlation Data

Table A-1: λ_1 pressure and spectral correlations for different equivalence ratio conditions

φ	R{row,column}	Peak signal	Signal @ -10 aTDC	Signal @ +10 aTDC
1.00	IMEP	-0.42	-0.14	-0.71
	Peak Pressure	0.82	0.44	0.96
	Avg. Pressure	0.61	0.44	0.93
	Total Heat Release	-0.53	-0.18	-0.82
1.51	IMEP	0.89	0.32	0.79
	Peak Pressure	0.95	0.32	0.94
	Avg. Pressure	0.93	0.32	0.94
	Total Heat Release	-0.76	-0.29	-0.66
0.67	IMEP	0.87	0.18	0.53
	Peak Pressure	0.88	0.11	0.54
	Avg. Pressure	0.90	0.16	0.52
	Total Heat Release	-0.66	-0.01	-0.36
0.59	IMEP	0.81	0.17	0.47
	Peak Pressure	0.46	0.19	0.15
	Avg. Pressure	0.81	0.18	0.46
	Total Heat Release	0.71	0.16	0.43

Table A-2: λ_2 pressure and spectral correlations for different equivalence ratio conditions

φ	R{row,column}	Peak signal	Signal @ -10 aTDC	Signal @ +10 aTDC
1.00	IMEP	-0.41	-0.15	-0.67
	Peak Pressure	0.61	0.39	0.83
	Avg. Pressure	0.53	0.37	0.82
	Total Heat Release	-0.53	-0.18	-0.78
1.51	IMEP	0.80	0.24	0.80
	Peak Pressure	0.86	0.15	0.91
	Avg. Pressure	0.85	0.17	0.90
	Total Heat Release	-0.70	-0.27	-0.65
0.67	IMEP	0.76	0.37	0.48
	Peak Pressure	0.84	0.42	0.51
	Avg. Pressure	0.83	0.41	0.52
	Total Heat Release	-0.68	-0.36	-0.44
0.59	IMEP	0.12	-0.10	0.08
	Peak Pressure	0.06	-0.05	0.05
	Avg. Pressure	0.12	-0.10	0.08
	Total Heat Release	0.11	-0.06	0.05

Table A-3: λ_1 pressure and spectral correlations for N_2 dilution and lean/dilute conditions

φ	Dilution	R{row,column}	Peak signal	Signal @ -10 aTDC	Signal @ +10 aTDC
1.00	9% wt N_2	IMEP	0.65	0.25	0.61
		Peak Pressure	0.89	0.31	0.89
		Avg. Pressure	0.79	0.29	0.86
		Total Heat Release	-0.79	-0.24	-0.69
1.00	19% wt N_2	IMEP	0.84	0.15	0.76
		Peak Pressure	0.81	0.07	0.73
		Avg. Pressure	0.84	0.13	0.78
		Total Heat Release	-0.59	-0.16	-0.61
0.79	9% wt N_2	IMEP	0.91	0.20	0.79
		Peak Pressure	0.85	0.05	0.64
		Avg. Pressure	0.94	0.18	0.79
		Total Heat Release	-0.76	-0.03	-0.49
0.79	5% wt CO_2	IMEP	0.95	0.27	0.73
		Peak Pressure	0.76	0.18	0.75
		Avg. Pressure	0.94	0.25	0.76
		Total Heat Release	-0.70	-0.19	-0.63

Table A-4: λ_2 pressure and spectral correlations for N_2 dilution and lean/dilute conditions

φ	Dilution	R{row,column}	Peak signal	Signal @ -10 aTDC	Signal @ +10 aTDC
1.00	9% wt N_2	IMEP	0.45	0.18	0.46
		Peak Pressure	0.71	0.44	0.82
		Avg. Pressure	0.65	0.45	0.80
		Total Heat Release	-0.56	-0.28	-0.59
1.00	19% wt N_2	IMEP	0.16	0.07	0.13
		Peak Pressure	0.08	0.04	0.06
		Avg. Pressure	0.14	0.07	0.11
		Total Heat Release	-0.20	-0.12	-0.12
0.79	9% wt N_2	IMEP	0.90	0.26	0.76
		Peak Pressure	0.85	0.14	0.74
		Avg. Pressure	0.92	0.21	0.78
		Total Heat Release	-0.77	-0.16	-0.52
0.79	5% wt CO_2	IMEP	0.85	0.22	0.58
		Peak Pressure	0.79	0.13	0.55
		Avg. Pressure	0.87	0.19	0.58
		Total Heat Release	-0.60	-0.08	-0.41

Table A-5: λ_1 pressure and spectral correlations for CO_2 dilution conditions

φ	Dilution	R{row,column}	Peak signal	Signal @ -10 aTDC	Signal @ +10 aTDC
1.00	5% wt CO_2	IMEP	0.75	0.25	0.80
		Peak Pressure	0.59	0.20	0.96
		Avg. Pressure	0.61	0.21	0.95
		Total Heat Release	-0.72	-0.22	-0.77
1.00	9% wt CO_2	IMEP	0.95	0.17	0.87
		Peak Pressure	0.83	0.13	0.87
		Avg. Pressure	0.92	0.16	0.90
		Total Heat Release	-0.83	-0.17	-0.71
1.00	11% wt CO_2	IMEP	0.94	0.21	0.73
		Peak Pressure	0.74	0.14	0.68
		Avg. Pressure	0.94	0.20	0.75
		Total Heat Release	-0.32	-0.03	-0.24
1.00	19% wt CO_2	IMEP	0.91	-0.03	0.34
		Peak Pressure	0.31	-0.05	0.23
		Avg. Pressure	0.92	-0.03	0.35
		Total Heat Release	0.60	-0.06	0.29

Table A-6: λ_2 pressure and spectral correlations for CO_2 dilution conditions

φ	Dilution	R{row,column}	Peak signal	Signal @ -10 aTDC	Signal @ +10 aTDC
1.00	5% wt CO_2	IMEP	0.60	0.20	0.72
		Peak Pressure	0.61	0.11	0.83
		Avg. Pressure	0.59	0.10	0.82
		Total Heat Release	-0.49	-0.26	-0.65
1.00	9% wt CO_2	IMEP	0.83	0.22	0.66
		Peak Pressure	0.77	0.10	0.66
		Avg. Pressure	0.83	0.17	0.69
		Total Heat Release	-0.66	-0.15	-0.62
1.00	11% wt CO_2	IMEP	0.78	0.08	0.52
		Peak Pressure	0.74	-0.07	0.45
		Avg. Pressure	0.80	0.04	0.52
		Total Heat Release	-0.51	0.01	-0.28
1.00	19% wt CO_2	IMEP	0.59	-0.04	0.29
		Peak Pressure	0.05	0.02	0.91
		Avg. Pressure	0.58	-0.03	0.29
		Total Heat Release	0.37	0.04	0.32

Bibliography

[1] P. R. S. Masson-Delmotte, V., P. Zhai, H.-O. Pörtner, D. Roberts, J. Skea, T. M. A. Pirani, W. Moufouma-Okia, C. Péan, R. Pidcock, S. Connors, J.B.R. Matthews, Y. Chen, X. Zhou, M.I. Gomis, E. Lonnoy, and and T. W. M. Tignor, "2018: Global Warming of 1.5°C.An IPCC Special Report on the impacts of global warming of 1.5°C above pre-industrial levels and related global greenhouse gas emission pathways, in the context of strengthening the global response to the threat of climate ch," 2018.

[2] U. N. E. Programme, "Emissions Gap Report 2019," Nairobi, 2019.

[3] U. S. Energy Information Administration, "Monthly Energy Review - September 2019," vol. September, 2019.

[4] U. Federal Highway Administration, "Highway Statistics 2017," 2017.

[5] International Energy Agency, "Putting CO2 to Use: Creating value from emissions," no. September, p. 86, 2019.

[6] E. P. Agency, "2017 and Later Model Year Light-Duty Vehicle Greenhouse Gas Emissions and Corporate Average Fuel Economy Standards," *Fed. Regist.*, vol. 77, no. 199, pp. 62624–63200, 2012.

[7] J. B. Heywood, *Internal Combustion Engine Fundamentals*. McGraw-Hill New York, 1988.

[8] R. D. Reitz, "Directions in internal combustion engine research," *Combust. Flame*, vol. 160, no. 1, pp. 1–8, 2013.

[9] M. Yao, Z. Zheng, and H. Liu, "Progress and recent trends in homogeneous charge compression ignition (HCCI) engines," *Prog. Energy Combust. Sci.*, vol. 35, no. 5, pp. 398–437, 2009.

[10] M. Krishnamoorthi, R. Malayalamurthi, Z. He, and S. Kandasamy, "A review on low temperature combustion engines: Performance, combustion and emission characteristics," *Renew. Sustain. Energy Rev.*, vol. 116, no. September, p. 109404, 2019.

[11] K. Epping, S. Aceves, R. Bechtold, and J. Dec, "The potential of HCCI combustion for high efficiency and low emissions," *SAE Tech. Pap.*, no. 724, 2002.

[12] J. Torregrosa, P. C. Olmeda, C. A. Romero, M. Térmicos, U. P. D. E. Valencia, and C. De Vera, "Revising engine heat transfer 1.," *Ann. Fac. Eng. Hunedoara*, vol. 6, no. 3, pp. 245–265, 2008.

[13] G. Borman and K. Nishiwaki, "Internal-combustion engine heat transfer," *Prog. Energy Combust. Sci.*, vol. 13, no. 1, pp. 1–46, 1987.

[14] M. F. Modest and D. C. Haworth, *Radiative Heat Transfer in Turbulent Combustion Systems: Theory and Applications*. Springer, 2016.

[15] C. Paul *et al.*, "Modeling radiative heat transfer and turbulence-radiation interactions in engines," in *U.S. National Combustion Meeting*, 2017, vol. 10, pp. 1–6.

[16] S. F. Fernandez *et al.*, "Soot and spectral radiation modeling for high-pressure turbulent spray flames," *Combust. Flame*, vol. 190, pp. 402–415, 2018.

[17] D. L. Reuss, V. Sick, and P. Schiffmann, "TCC Engine Collection," *Deep Blue Data*. [Online]. Available: https://deepblue.lib.umich.edu/data/collections/8k71nh59c?locale=en.

[18] P. C. Ma, M. Greene, V. Sick, and M. Ihme, "Non-equilibrium wall-modeling for internal combustion engine simulations with wall heat transfer," vol. 18, pp. 15–25, 2017.

[19] V. Raj Mohan and D. C. Haworth, "Turbulence-chemistry interactions in a heavy-duty compression-ignition engine," *Proc. Combust. Inst.*, vol. 35, no. 3, pp. 3053–3060, 2015.

[20] G. Woschni, “A Universally Applicable Equation for the Instantaneous Heat Transfer Coefficient in the Internal Combustion Engine,” 1967.
[21] G. D. Ebersole, P. S. Myers, O. A. Uyehara, G. D. Ebersole, P. S. Myers, and O. A. Uyehara, “The Radiant and Convective Components of Diesel Engine Heat Transfer The Radiant and Convective Components of Diesel Engine Heat Transfer,” 1963.
[22] P. Flynn, M. Mizusawa, O. A. Uyehara, and P. S. Myers, “An Experimental Determination of the Instantaneous Potential Radiant Heat Transfer Within an Operating Diesel Engine,” *SAE Tech. Pap.*, pp. 95–126, 1972.
[23] G. Sitkei and G. V Ramanaiah, “A rational approach for calculation of heat transfer in diesel engines,” pp. 165–174, 1972.
[24] P. Furmanski, J. Banaszek, and T. S. Wisniewski, “Radiation heat transfer in a combustion chamber of diesel engine with partially transparent burnt gas zone,” *SAE Tech. Pap.*, no. 724, 1998.
[25] M. Greene, “Momentum Near-wall Region Characterization in a Reciprocating Internal-combustion Engine,” Univesity of Michigan, 2017.
[26] A. Wu, S. Keum, and V. Sick, “Large Eddy Simulations with Conjugate Heat Transfer (CHT) modeling of Internal Combustion Engines (ICEs),” *Oil Gas Sci. Technol. – Rev. d’IFP Energies Nouv.*, vol. 74, p. 51, 2019.
[27] L. A. Kranendonk, A. W. Caswell, A. M. Myers, and S. T. Sanders, “Wavelength-Agile Laser Sensors for Measuring Gas Properties in Engines,” 2003.
[28] W. J. Parrish, J. D. Blackwell, G. T. Kincaid, and R. C. Paulson, “Low-cost high-performance InSb 256 x 256 infrared camera,” *Infrared Technol. XVII*, vol. 1540, no. December 1991, p. 274, 1991.
[29] V. Sick, L. Henrion, A. Mazacioglu, and M. C. Gross, “Time-resolved infrared imaging and spectroscopy for engine diagnostics,” in *13th AVL Intl. Symp. on Propulsion Diagnostics Proceedings*, 2018.
[30] F. J. Struwe and D. E. Foster, “In-cylinder measurement of particulate radiant heat transfer in a direct injection diesel engine,” *SAE Tech. Pap.*, no. 724, 2003.
[31] J. F. Wiedenhoefer and R. D. Reitz, “Multidimensional modeling of the effects of radiation and soot deposition in heavy-duty diesel engines,” *SAE Trans.*, vol. 112, no. 3, pp. 784–804, 2003.
[32] J. F. Wiedenhoefer and R. D. Reitz, “A multidimensional radiation model for diesel engine simulation with comparison to experiment,” *Numer. Heat Transf. Part A Appl.*, vol. 44, no. 7, pp. 665–682, 2003.
[33] M. F. Modest, *Radiative Heat Transfer*, 3rd ed. Academic Press, 2013.
[34] G. Pal, A. Gupta, M. F. Modest, and D. C. Haworth, “Comparison of accuracy and computational expense of radiation models in simulation of non-premixed turbulent jet flames,” *Combust. Flame*, vol. 162, no. 6, pp. 2487–2495, 2015.
[35] C. Paul, D. C. Haworth, and M. F. Modest, “A simplified CFD model for spectral radiative heat transfer in high-pressure hydrocarbon-air combustion systems,” *Proc. Combust. Inst.*, vol. 37, pp. 4617–4624, 2019.
[36] D. C. Haworth, S. P. Roy, J. Cai, A. Sircar, A. Imren, and M. F. Modest, “Modeling Radiative Heat Transfer in Engines,” vol. 2010, no. 10, pp. 1–6, 2015.
[37] C. Paul, S. Ferreyro-Fernandez, D. C. Haworth, S. Roy, and M. F. Modest, “A detailed modeling study of radiative heat transfer in a heavy-duty diesel engine,” *Combust. Flame*, vol. 200, pp. 325–341, 2019.

[38] L. Henrion *et al.*, “Characterization of radiative heat transfer in a spark-ignition engine through high-speed experiments and simulations,” *Oil Gas Sci. Technol. – Rev. d’IFP Energies Nouv.*, vol. 74, p. 61, 2019.
[39] T. L. Bergman, F. P. Incropera, D. P. DeWitt, and A. S. Lavine, *Fundamentals of heat and mass transfer*. John Wiley & Sons, 2011.
[40] C. S. Goldenstein, R. M. Spearrin, J. B. Jeffries, and R. K. Hanson, “Infrared laser-absorption sensing for combustion gases,” *Prog. Energy Combust. Sci.*, vol. 60, pp. 132–176, 2017.
[41] R. Gade and T. B. Moeslund, “Thermal cameras and applications: A survey,” *Mach. Vis. Appl.*, vol. 25, no. 1, pp. 245–262, 2014.
[42] L. S. Rothman *et al.*, “The HITRAN2012 molecular spectroscopic database,” *J. Quant. Spectrosc. Radiat. Transf.*, vol. 130, pp. 4–50, 2013.
[43] C. N. Banwell and E. M. McCash, “Fundamentals of molecular spectroscopy. 1994.” Tata McGraw Hill, New Delhi.
[44] A. G. Gaydon, *Spectroscopy and Combustion Theory*, 2nd ed. London: Chapman & Hall, 1948.
[45] A. G. Gaydon, *The Spectroscopy of Flames*, vol. 54, no. 4. Springer Science & Business Media, 1957.
[46] D. C. Harris and M. D. Bertolucci, *Symmetry and Spectroscopy: an Introduction to Vibrational and Electronic Spectroscopy*. New York: Dover Publications, 1989.
[47] R. Pecsok, L. Shields, T. Cairns, and J. McWilliam, *Modern Methods of Chemical Analysis*. New York: John-Wiley, 1976.
[48] M. J. Hollas, *Modern Spectroscopy*, 3rd ed. Chichester: John Wiley & Sons, 1996.
[49] S. S. Penner, *Quantitative molecular spectroscopy and gas emissivities*. Reading: Addison-Wesley, 1959.
[50] R. K. Hanson, R. M. Spearrin, and C. S. Goldenstein, *Spectroscopy and Optical Diagnostics for Gases*. 2016.
[51] G. Herzberg, “Infrared and raman spectra of polyatomic molecules,” pp. 1–633, 1945.
[52] C. Paul, “An Open-Source Framework for Advanced Turbulent Combustion and Radiaiton Modeling in IC Engines,” Pennsylvania State University, 2018.
[53] D. F. Swinehart, “The Beer-Lambert law,” *J. Chem. Educ.*, vol. 39, no. 7, pp. 333–335, 1962.
[54] L. S. Rothman *et al.*, “HITEMP, the high-temperature molecular spectroscopic database,” *J. Quant. Spectrosc. Radiat. Transf.*, vol. 111, no. 15, pp. 2139–2150, 2010.
[55] L. A. Kranendonk, A. W. Caswell, and S. T. Sanders, “Robust method for calculating temperature, pressure, and absorber mole fraction from broadband spectra,” *Appl. Opt.*, vol. 46, no. 19, pp. 4117–4124, 2007.
[56] O. Witzel, A. Klein, C. Meffert, C. Schulz, S. A. Kaiser, and V. Ebert, “Calibration-free, high-speed, in-cylinder laser absorption sensor for cycle-resolved, absolute H2O measurements in a production IC engine,” *Proc. Combust. Inst.*, vol. 35, no. 3, pp. 3653–3661, 2015.
[57] L. A. Kranendonk, J. W. Walewski, T. Kim, and S. T. Sanders, “Wavelength-agile sensor applied for HCCI engine measurements,” *Proc. Combust. Inst.*, vol. 30, no. 1, pp. 1619–1626, 2005.
[58] M. J. H. and J. S. W. Peter O. Witze, “Fiber-Optic Instrumented Spark Plug for Measuring Early Flame Development in Spark Ignition Engines,” *SAE Trans.*, vol. 97, no. Section 3,

pp. 813–825, 1988.
[59] C. R. Bailey and K. H. Lih, “The Infrared Emission Spectra of the Bunsen and Allied Flames,” *Trans. Faraday Soc.*, pp. 29–32, 1929.
[60] P. R. Griffiths and J. A. de Haseth, *Fourier Transform Infrared Spectrometry*, 2nd ed. John Wiley & Sons, 2007.
[61] R. A. Palmer, C. J. Manning, J. A. Rzepiela, J. M. Widder, and J. L. Chao, “Time-resolved spectroscopy using step-scan Fourier transform interferometry,” *Appl. Spectrosc.*, vol. 43, no. 2, pp. 193–195, 1989.
[62] K. D. Rein, S. T. Sanders, S. R. Lowry, E. Y. Jiang, and J. J. Workman, “In-cylinder Fourier-transform infrared spectroscopy,” *Meas. Sci. Technol.*, vol. 19, no. 4, p. 043001, 2008.
[63] K. Rein, S. Sanders, and R. Bartula, “Interferometric techniques for crank-angle resolved measurements of gas spectra in engines,” *Framework*, pp. 1–7, 2009.
[64] K. D. Rein and S. T. Sanders, “Fourier-transform absorption spectroscopy in reciprocating engines.,” *Appl. Opt.*, vol. 49, no. 25, pp. 4728–34, 2010.
[65] M. P. B. Musculus, “Measurements of the Influence of Soot Radiation on In-Cylinder Temperatures and Exhaust NOx in a Heavy-Duty DI Diesel Engine,” vol. 2005, no. 724, 2005.
[66] B. D. Stojkovic, T. D. Fansler, M. C. Drake, and V. Sick, “High-speed imaging of OH* and soot temperature and concentration in a stratified-charge direct-injection gasoline engine,” *Proc. Combust. Inst.*, vol. 30 II, no. 2, pp. 2657–2665, 2005.
[67] H. Zhao and N. Ladommatos, “Optical diagnostics for soot and temperature measurement in diesel engines,” *Prog. Energy Combust. Sci.*, vol. 24, no. 3, pp. 221–255, 1998.
[68] S. M. Yukio Matsui, Takeyuki Kanimoto, “A Study on the Application the Two-Color Method to the measurement of flame temperature and Soot Concentration in Diesel Engines,” *SAE Tech. Pap.*, 1980.
[69] C. S. Goldenstein, V. A. Miller, R. Mitchell Spearrin, and C. L. Strand, “SpectraPlot.com: Integrated spectroscopic modeling of atomic and molecular gases,” *J. Quant. Spectrosc. Radiat. Transf.*, vol. 200, pp. 249–257, 2017.
[70] P. Schiffmann, D. L. Reuss, and V. Sick, “Empirical investigation of spark-ignited flame-initiation cycle-to-cycle variability in a homogeneous charge reciprocating engine,” *Int. J. Engine Res.*, vol. 19, no. 5, pp. 491–508, 2018.
[71] F. W. Bowditch, “A new tool for combustion research a quartz piston engine,” *SAE Tech. Pap.*, 1961.
[72] W. D. Callister, *Materials Science and Engineering: An Introduction*, 10th ed. Wiley, 2018.
[73] Engineering ToolBox, “Thermal Conductivity of selected Materials and Gases,” *engineeringtoolbox.com*, 2003. .
[74] D. J. Oude Nijeweme, J. B. W. Kok, C. R. Stone, and L. Wyszynski, “Unsteady in-cylinder heat transfer in a spark ignition engine: Experiments and modelling,” *Proc. Inst. Mech. Eng. Part D J. Automob. Eng.*, vol. 215, no. 6, pp. 747–760, 2001.
[75] R. M. Sova, M. J. Linevsky, M. E. Thomas, and F. F. Mark, “High-temperature infrared properties of sapphire, AlON, fused silica, yttria, and spinel,” *Infrared Phys. Technol.*, vol. 39, no. 4, pp. 251–261, 1998.
[76] U. P. Oppenheim and U. Even, “Infrared Properties of Sapphire at Elevated Temperatures,” *J. Opt. Soc. Am.*, vol. 52, no. 9, pp. 1078–1079, 1962.

[77] M. E. Thomas, R. I. Joseph, and W. J. Tropf, “Infrared transmission properties of sapphire, spinel, yttria, and ALON as a function of temperature and frequency,” *Appl. Opt.*, vol. 27, no. 2, pp. 239–245, 1998.
[78] R. R. Steeper and E. J. Stevens, “Characterization of combustion, piston temperatures, fuel sprays, and fuel-air mixing in a DISI optical engine,” *SAE Tech. Pap.*, no. 724, 2000.
[79] T. Husberg, S. Gjirja, I. Denbratt, A. Omrane, M. Aldén, and J. Engström, “Piston temperature measurement by use of thermographic phosphors and thermocouples in a heavy-duty diesel engine run under partly premixed conditions,” *SAE Tech. Pap.*, no. 724, 2005.
[80] Z. M. Ayers, J. M. Fisher, A. Brown, S. F. Son, and T. R. Meyer, “KHz-rate temperature imaging using time-domain thermographic phosphorescence,” *AIAA Scitech 2019 Forum*, no. January, pp. 1–6, 2019.
[81] T. Ombrello, C. Carter, and V. Katta, “Burner platform for sub-atmospheric pressure flame studies,” *Combust. Flame*, vol. 159, no. 7, pp. 2363–2373, 2012.
[82] S. Prucker, W. Meier, and W. Stricker, “A flat flame burner as calibration source for combustion research: Temperatures and species concentrations of premixed H2/air flames,” *Rev. Sci. Instrum.*, vol. 65, no. 9, pp. 2908–2911, 1994.
[83] F. N. Egolfopoulos, P. Cho, and C. K. Law, “Laminar flame speeds of methane-air mixtures under reduced and elevated pressures,” *Combust. Flame*, vol. 76, no. 3–4, pp. 375–391, 1989.
[84] I. Glassman, *Combustion*, 1st ed. Academic Press, 1977.
[85] C. J. Humphreys and E. Paul, “Interferometric Wavelength Determinations in the First Spectrum of ’ 36 Xe,” *J. Opt. Soc. Am.*, vol. 60, no. 10, pp. 1302–1310, 1970.
[86] J. Das *et al.*, “Smart onboard image enhancement algorithms for SWIR day and night vision camera,” *Infrared Technol. Appl. XLI*, vol. 9451, no. May 2015, p. 945103, 2015.
[87] J. Neys *et al.*, “Cheetah: A high frame rate, high resolution SWIR image camera,” *Sensors, Syst. Next-Generation Satell. XII*, vol. 7106, no. October 2008, p. 71061M, 2008.
[88] NASA, “Chemical Equilibrium with applications.” NASA, 2017.
[89] S. F. Fernandez, “Advance Soot and Radiation Models for Laminar and Turbulent Flames,” Pennsylvania State University, 2018.
[90] L. Henrion, V. Sick, and D. C. Haworth, “Quantifying the significance of radiative trapping in a spark-ignited internal combustion engine,” in *14th internationales AVL Powertrain Diagnostik Symposium*.
[91] P. Schiffmann, “Root causes of cycle-to-cycle combustion variations in spark ignited engines,” 2016.
[92] V. Sick, “High speed imaging in fundamental and applied combustion research,” *Proc. Combust. Inst.*, vol. 34, no. 2, pp. 3509–3530, 2013.
[93] Y. Shekhawat *et al.*, “An experimental and simulation study of early flame development in a homogeneous-charge spark-ignition engine,” *Oil Gas Sci. Technol.*, vol. 72, no. 5, 2017.
[94] H. Weller, C. Greenshields, and C. de Rouvray, “OpenFoam,” *The OpenFOAM Foundation*. [Online]. Available: https://openfoam.org/.
[95] M. F. Modest, “Backward Monte Carlo simulations in radiative heat transfer,” *J. Heat Transfer*, vol. 125, no. 1, pp. 57–62, 2003.
[96] X. Lu and P. F. Hsu, “Reverse Monte Carlo method for transient radiative transfer in participating media,” *J. Heat Transfer*, vol. 126, no. 4, pp. 621–627, 2004.

[97] Mohammad K. Alzuabi, “Imaging of Temperature Variations in the Near-Wall Region of an Optical Reciprocating Engine using Laser-Induced Fluorescence,” University of Michigan, 2020.
[98] P. Schiffmann, “Root Causes of Cycle-to-Cycle Combustion Variations in Spark Ignited Engines,” University of Michigan, 2016.
[99] A. A. Quader, “Why intake charge dilution decreases nitric oxide emission from spark ignition engines,” *SAE Pap. 710009*, pp. 20–30, 1971.
[100] E. K. Plyler, L. R. Blaine, and E. D. Tidwell, “Infrared absorption and emission spectra of carbon monoxide in the region from 4 to 6 microns,” *J. Res. Natl. Bur. Stand. (1934).*, vol. 55, no. 4, p. 183, 1955.
[101] L. A. Kranendonk, R. Huber, J. G. Fujimoto, and S. T. Sanders, “Wavelength-agile H2O absorption spectrometer for thermometry of general combustion gases,” *Proc. Combust. Inst.*, vol. 31 I, no. 1, pp. 783–790, 2007.
[102] J. R. Lakowicz, *Principles of fluorescence spectroscopy, 3rd Edition, Joseph R. Lakowicz, editor*. 2006.
[103] H. Kautsky, “Quenching of Luminescence by Oxygen,” *Trans. Faraday Soc.*, 1939.
[104] R. B. Bramlette and C. D. Depcik, “Review of propane-air chemical kinetic mechanisms for a unique jet propulsion application,” *J. Energy Inst.*, no. xxxx, 2019.
[105] F. L. Dryer and C. K. Westbrook, “Simplified Reaction Mechanisms for the Oxidation of Hydrocarbon Fuels in Flames,” *Combust. Sci. Technol.*, vol. 27, no. 1–2, pp. 31–43, 1981.